STUDY OF STRESS CHANGES IN UNCONVENTIONAL RESERVOIRS WITH COUPLED FLOW AND GEOMECHANICS SIMULATIONS

A Dissertation

by

NING LI

Submitted to the Office of Graduate and Professional Studies of
Texas A&M University
in partial fulfillment of the requirements for the degree of

DOCTOR OF PHILOSOPHY

Chair of Committee,	John E. Killough
Co-Chair of Committee,	Kan Wu
Committee Members,	Maria A. Barrufet
	Eduardo Gildin
Head of Department,	Jeff Spath

May 2021

Major Subject: Petroleum Engineering

ABSTRACT

The development of unconventional reservoirs in us follows this practice: parent wells are first drilled, then infill wells are drilled to produce the region between parent wells. One of the key factors for the success of this strategy is to find out the stress change induced by parent well production and how to generate efficient fracture geometry for infill wells.

The first work in this paper is the analysis of the stress distribution after parent well production. This analysis is based on a real field model. The lower-than-expected infill well production rate is first analyzed, then possible causes for this poor production performance are checked. Based on the real field model, stress is calculated after the parent well's production. To precisely simulate hydraulic fractures, the swarm effect is considered. Results show that due to non-uniform fracture geometry in the parent well, an irregular depletion area and large stress change region are induced in the reservoir; frac hits still can be induced from the irregular depletion area between the staggered parent and infill wells; Parent well depletion not only changes reservoir stress in the layer of the parent well but also alters stress in the lower layer of the infill wells.

Secondly, the efficiency of subsequent parent well water injection is analyzed. Different injection designs are simulated to investigate the influence of factors like reservoir fluid type, injection pressure, and injection volume. Results show that subsequent parent well water injection mainly restores the stress and pressure near the wellbore; it is more efficient in the oil-water two-phase case than in cases with gas.

The third work is the simulation of hydraulic fracture closure during production. A 3D geomechanics simulator is developed. Then it is coupled to GURU, a fully compositional simulator, using a modified fixed stress coupling method. A relationship derived by Bandis and the Cubic Law are used to calculate the fracture closure and the fracture permeability change. Simulations show that fracture closure mainly affects the early production stage; at different locations along a fracture, fracture width and permeability change show different trends.

ACKNOWLEDGEMENTS

I would like to thank my committee chair, Dr. Killough and Dr. Wu, and my committee members, Dr. Gildin and Dr. Barrufet for their guidance and support throughout the course of this research.

Thanks also go to my friends and colleagues and the department faculty and staff for making my time at Texas A&M University a great experience.

Finally, thanks to my mother and father for their support.

CONTRIBUTORS AND FUNDING SOURCES

Contributors

This work was supervised by a thesis (or) dissertation committee consisting of Professor John Killough, Kan Wu, and Eduardo Gildin of the Department of Petroleum Engineering and Professor(s) Maria A. Barrufet of the Department of Chemical Engineering.

The data analyzed for Chapters 1 and 2 was provided by Marathon Oil Corporation.

All other work conducted for the thesis (or) dissertation was completed by the student independently.

Funding Sources

This study is supported by a fellowship from Marathon Oil Corporation.

TABLE OF CONTENTS

Page

LIST OF FIGURES

Page

LIST OF TABLES

Page

CHAPTER I

INTRODUCTION

1.1 Background

1.1.1 Well interference in unconventional reservoirs

The practice of unconventional reservoirs development follows this strategy: first, parent wells are drilled in a section to hold the lease. Then infill wells are drilled to produce regions between parent wells. **Fig. 1** shows the newly drilled wells from 2008 to 2017 in Eagle Ford. As we can see from the plot, from 2014, more infill wells were drilled than parent wells. With these infill wells drilled, well spacings are significantly reduced and as a result, occurrences of well interference or frac-hits are found in many Eagle Ford field observations (Miller et al. 2016; Lindsay et al. 2018; Awada et al. 2016; Bhardwaj et al. 2016; Cao et al. 2016; Gupta et al. 2012; Kamkom et al. 2007; Olson et al. 2012; Pankaj et al. 2018; Rainbolt et al. 2018; Safari et al. 2017; Sangnimnuan et al. 2018; Settari et al. 2017; Van Dam et al. 2000; Warpinski et al. 2002).

These infill wells are expected to as efficient as parent wells in terms of production performance. **Fig. 2** compared the production of parent and infill wells in 10 basins (Lindsay et al. 2018). From this comparison, it is found that the production of infill wells is usually lower than the parent wells. **Fig. 3** shows the production history of a parent well before and after the infill well completion (from King et al. 2017). After the infill well completion, the parent well resumed production, but the oil and gas production of the parent well went down by 65%; while there was a sharp increase in

water production. Cipolla et al. 2018 placed a pressure gauge at the parent well(H1) lateral and monitored the pressure change there during the fracturing operations of infill wells H2 and H4 (**Fig. 4**). A significant pressure increase in the parent well was observed and this is explained to be an evidence of frac hits from infill well H2. Similar field observations of well interference or frac hits can be found in other authors' papers (Rainbolt et al. 2018).

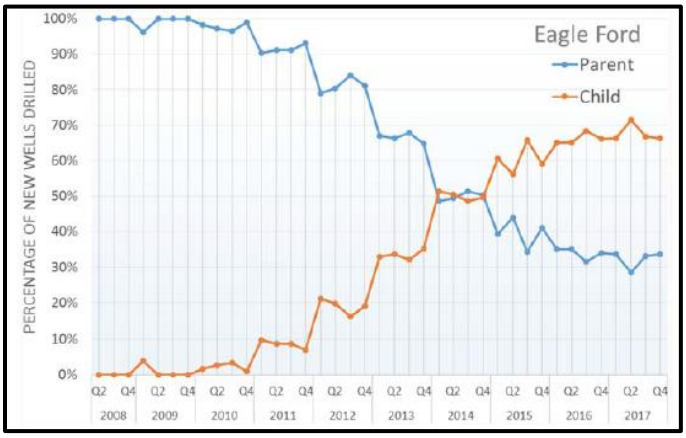

Figure 1 Newly drilled wells from 2008 to 2017 in Eagle Ford (Lindsay et al. 2018)

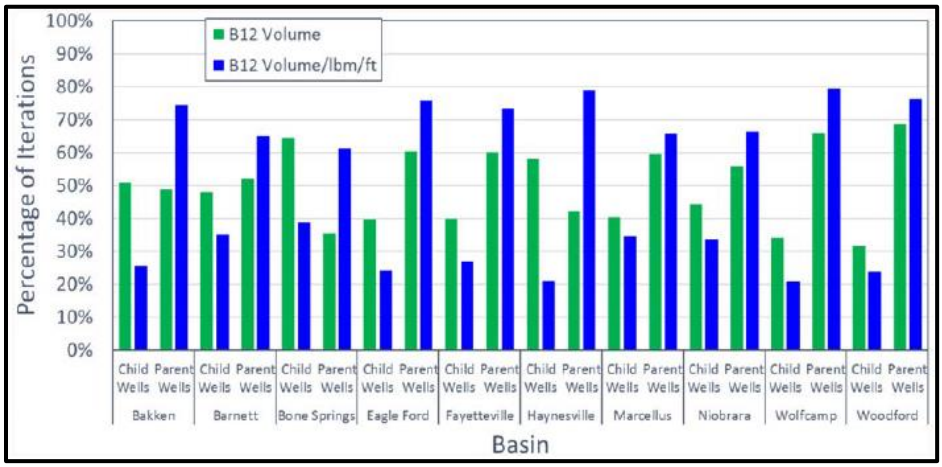

Figure 2 Production Comparison of parent and infill wells from 10 basins (Lindsay et al. 2018)

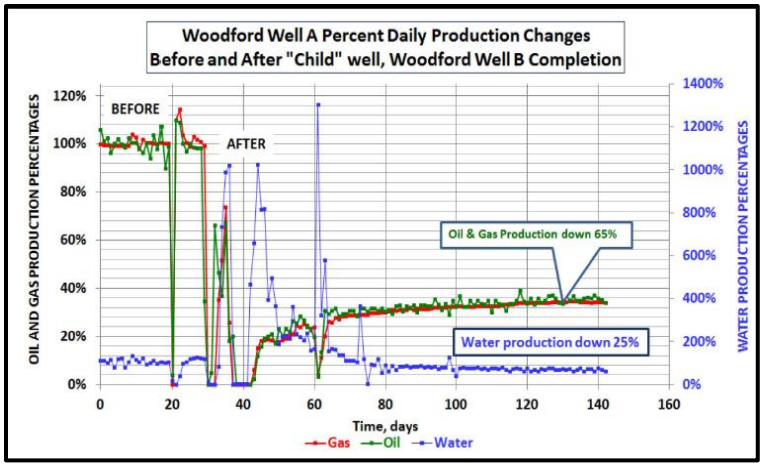

Figure 3 Production comparison of the parent well before and after infill well completion (King et al. 2017)

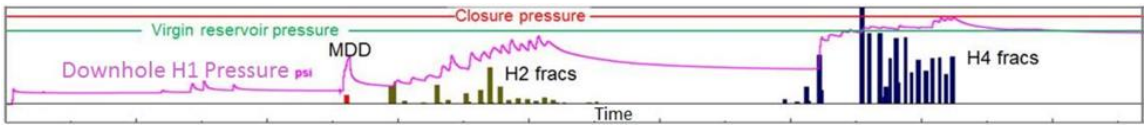

Figure 4 Pressure gauge data in the parent well (H1) lateral during completing infill wells H2 and H4 (Cipolla et al. 2018)

1.1.2 Mitigation strategies

Well interference or frac-hit between parent and infill wells causes the lower-than-expected production from infill wells and causes oil/gas production loss as well as increase in water production in parent wells. To mitigate the damage caused by well interference is a big challenge for unconventional reservoir operators. From papers (Gala et al. 2018, Whitfield et al. 2018), currently available mitigation strategies include, but not limited to: (1) shutting down the parent well before infill well fracturing operations. This strategy is the simplest, but costs production lost. (2) Keeping the parent well on production during the infill well completion to avoid the damage frac hits may cause on

parent well integrity. (3) Refracturing the parent well after infill frac completion to rebuild the productivity of parent wells. This strategy is time-consuming and expensive to execute. (4) Injecting water into the parent well before the infill completion to restore the altered stress field. This strategy is called subsequent parent well water injection.

My study focuses on understanding the mechanism and the effectiveness of subsequent parent well water injection. Currently, field trials of this approach are reported from several unconventional reservoirs, but their results are not consistent, both negative and positive results are observed. Gakhar et al. (2017) reported that injecting the parent well by injecting approximately 43000 bbls of water can reduce cumulative oil production from a multi-well pad by 7%. While Whitfield et al. (2018) reported successful filed application in Karnes filed and Hawkville.

Numerical analysis of this topic based on coupled flow and geomechanics can also be found in papers. Gala et al. (2018) studied the stress change around the parent well fractures induced by fluid injection and from his results, re-pressurization will be a more useful strategy in minimizing damage from frac-hits in a black oil reservoir. Kumar et al. (2018) used a simplified reservoir model and observed that the reduced reservoir pore pressure and stress state can be approximately restored to the original in-situ values with an injection of only 12 hours. Guo et al. (2018) also reported positive numerical results for subsequent parent well water injection, but in his case, longer injection times are required (0.5 to 3 years' injection is required to be effective). This is not acceptable in practice.

1.1.3 Coupled flow and geomechanics simulation

The coupled flow and mechanics are of interest in many fields outside our reservoir engineering area. This topic has been studied in soil science and civil engineering (Biot et al. 1941, Park et al. 1983). In reservoir engineering, geomechanics shows its important role in compaction drive oil/gas recovery with the development of unconventional reservoirs. Matrix and fracture permeability is also found to be highly related to reservoir deformation (Gai et al. 2006; Garipov et al. 2014).

Traditionally, in reservoir simulation, the geomechanics part is simplified by using the pressure-dependent porosity. To more properly describe the reservoir deformation and simulate its effects on the production performance of unconventional reservoirs, several coupling methods have been proposed. Coupling methods are typically classified into four types: fully coupled, iteratively coupled, explicitly coupled, and loosely coupled (Kim, 2010; Settari and Walters, 2001; Dean et al., 2006).

1.1.4 Fracture closure during production

Once production begins, fluid pressure in the hydraulic fractures drops. With compressive stress acting on the fracture surface, hydraulic fractures are forced to close. This closure results in the reduction in fracture width and space for reservoir fluid to flow through, and as a result, the production rate will decline sharply. In reservoir simulation, fracture closure is simulated as fracture permeability decline. This fracture closure has been proved by the scaled laboratory; experiments (Van Dam et al., 2002), and through field measurements (Warpinski et al., 2002).

Hydraulic fractures play a critical role in unconventional reservoirs as the matrix permeability there is ultra-low. This reduction in fracture permeability will significantly affect the production rate and accumulative production. In traditional reservoir simulators, fracture closure is ignored or considered with simplified methods (Yu et al., 2017). If the fracture closure effect is ignored, hydraulic fracture geometry does not change with time, and this will overestimate the production rate and generate enormous cumulative production forecasts. Some simplified methods assume that the compressive stress does not change with time and modify the fracture permeability as a function of only fluid pressure in fractures. Geomechanics simulation has shown that both magnitude and orientation of stress in the reservoir are altered by production, especially around hydraulic fractures.

1.2 Study scopes

The objective of my work is to understand how stress change in unconventional reservoirs during production and injection. The study scope covers 3 aspects: (1) to analyze the production induced stress change with a real field case; (2) to investigate how the altered stress will be restored by subsequent parent well water injection; (3) to simulate the fracture closure during production and study how this fracture closure affects production performance.

To analysis the production-induced stress change with a real field case, a workflow is established. History matching is done to calibrate the reservoir parameters and geomechanics parameters. Then, geomechanics simulations are run to get the stress distribution in the horizontal and vertical directions. The key factor to get reliable results

is the simulation of hydraulic fractures. To describe the geometry of hydraulic fracture as accurately as possible, the fracture swarm effect is considered.

To investigate how the altered stress will be restored by subsequent parent well water injection, different injection designs are simulated. Factors controlling the injection process include injection pressure, injection volume, and reservoir fluid type. In this part, which part of the altered stress can be restored and to which extent the stress could be restored are obtained.

To simulate the fracture closure, first, a 3D geomechanics simulator is developed. Then it is coupled to GURU a compositional simulator with a modified fixed stress iterative coupling method. In this simulation, hydraulic fractures are modeled with the EDFM method. To calculate the fracture permeability change as fracture close, a relationship between normal contact stress and fracture width derived by Bandis and the Cubic Law are used. Cases using this method, ignoring fracture closure, and using rock compaction tables are compared to find out how the fracture closure affects the production rate and cumulative production.

CHAPTER II

STRESS CHANGES CAUSED BY PARENT WELL PRODUCTION IN UNCONVENTIONAL RESERVOIRS

2.1 Field observations

This analysis is based on the field data of a section in the Meramec stack play. The Meramec stack play is in Anadarko Basin, Oklahoma, and is a multi-layered tight oil reservoir

In the target section, 7 production wells were drilled in a staggered layout. The parent well P1 was drilled in June 2015 and produced for 2 years before the six infill wells were drilled in May 2017. In the vertical direction, the Meramec Stack Play has 6 layers. The parent well was drilled in layer 3, infill wells W3D and W5D were drilled in layer 3, and the rest 4 infill wells were drilled in layer 4. The layout of these 7 wells is plotted in **Figs. 5** and **6**.

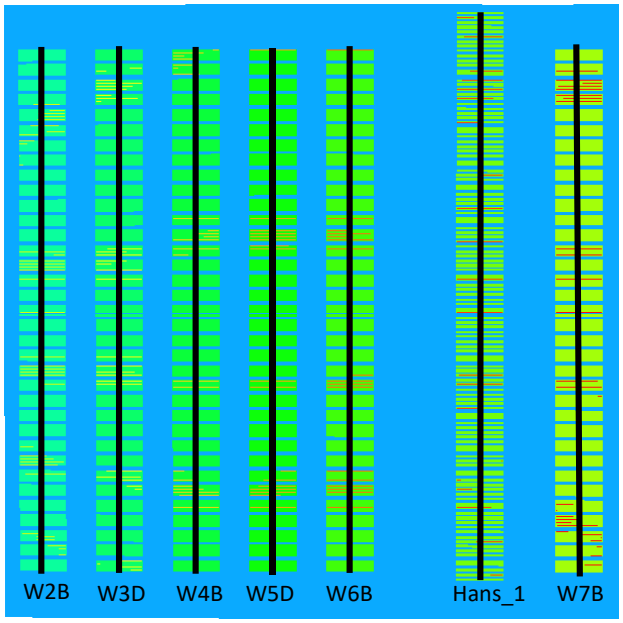

Figure 5 Map view of the layout of production wells

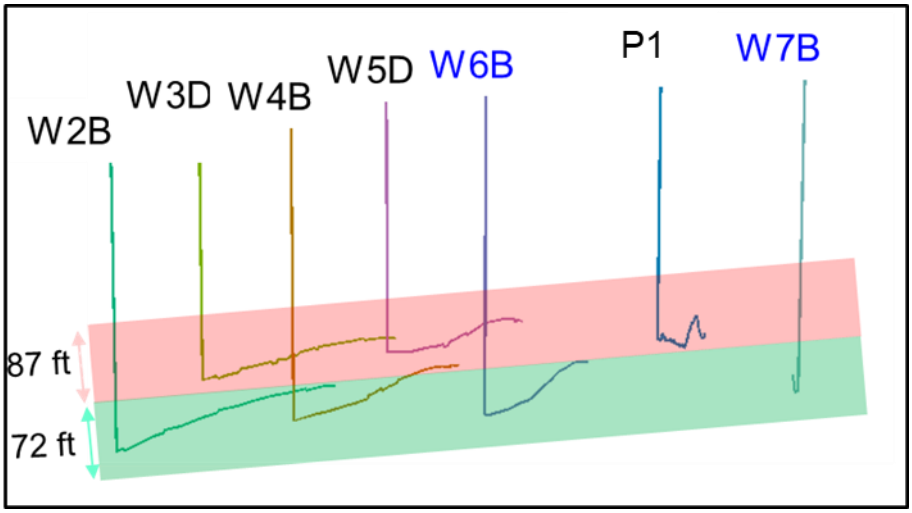

Figure 6 Section view of the layout of production wells

Fig. 7 shows the oil, gas, and water production from the parent well. Around May 2017, the parent well was shut-in for the infill well completion and resumed production after the completion. After the infill well completion, the oil rate of the parent well

dropped compared to that before shut-in; and a significant increase in water production from the parent well was observed. To make it clear, **Fig. 8** zooms into this time interval just before and after the infill well completion.

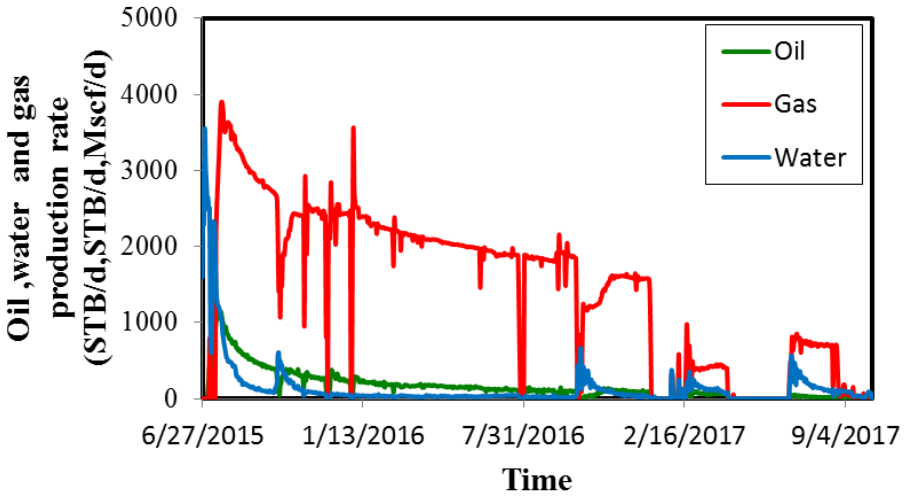

Figure 7 Production history of the parent well

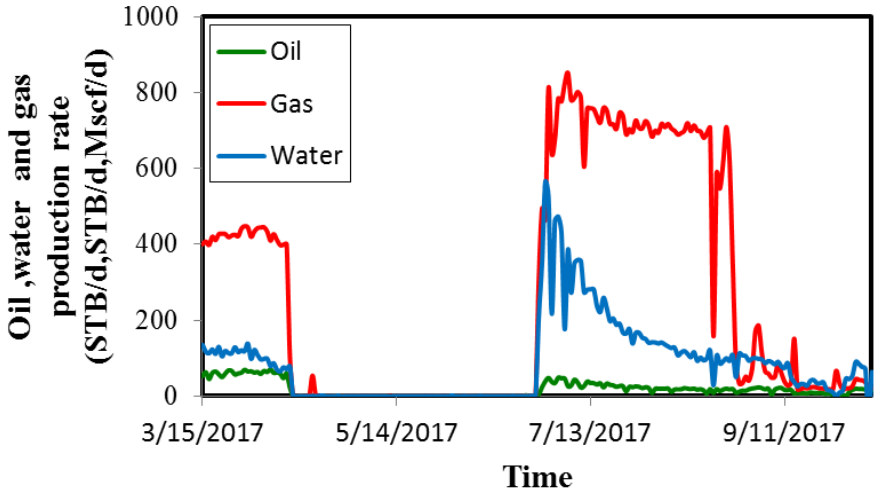

Figure 8 Production rate changes before and after infill well completion

Fig. 9 and **10** compare the oil and gas production from these 6 infill wells. Wells W6B and W7B are close to the parent well. At the early production stage, the gas and oil rates from these 2 wells are much lower than the rest 4 infill wells.

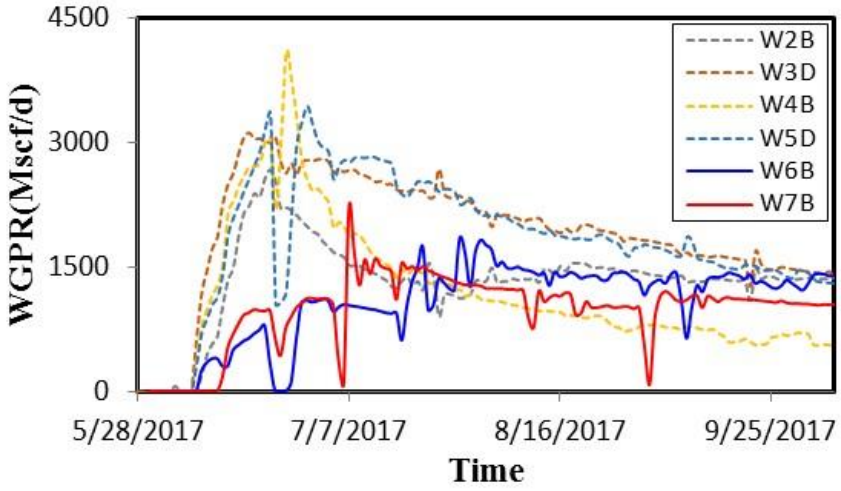

Figure 9 Gas production rate of infill wells

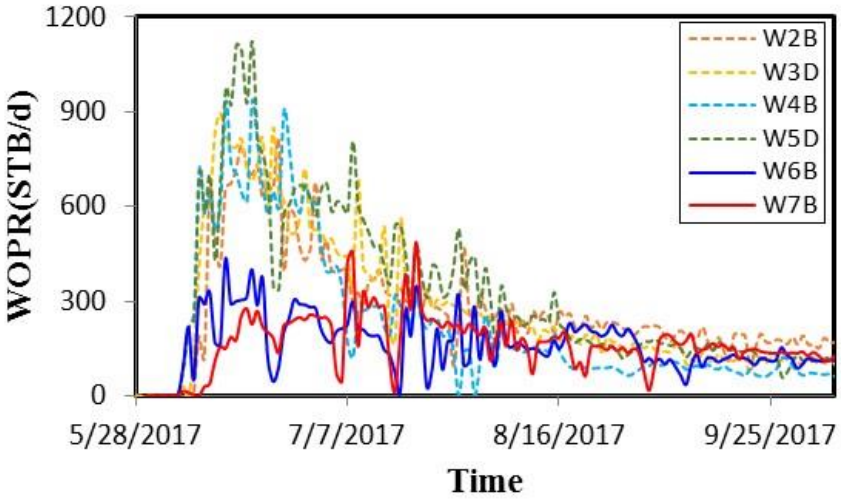

Figure 10 Oil production rate of infill wells

The above analysis shows that well interference occurred between the parent well and those two infill wells. The objective of this chapter is to find out and verify the mechanism that induced the well interference.

Our explanation is the parent well production altered the stress distribution. In the altered stress field, the infill well hydraulic fracture geometry is less efficient; it covers less area, which results in the low production rates in those two infill wells. At the same time, in this altered stress field, frac hits occurred between parent and infill wells fractures; this results in the water increase, oil and gas loss in the parent well. To justify this explanation, first of all, we need to analyze possible mechanisms that cause parent well production loss and low infill well production.

2.2 Analysis of the possible mechanisms that cause parent well production loss and low infill well production

The possible causes of the poor performance of both parent and child wells are listed as follows, we are going to check them one by one with available data.

1. Different landing depths of laterals of four infill wells in layer 4.
2. Well trajectories of four infill wells (toe up, toe down, undulating).
3. Operation conditions of four infill wells.
4. Designs of completion and fracturing treatments.
5. Stress change induced by parent well depletion negatively affects the effectiveness of infill well completion.

2.2.1 Comparison of infill well trajectories

From **Figs. 11** and **12**, no significant difference is found in terms of infill well trajectory. These 4 infill wells landed at a similar depth. As the thickness of layer 4 is 60ft on average, there is no large difference in landing depth. Then the laterals went up and ended up at almost the same depth. The slight difference in the trajectories does not cause so obvious difference in production rate. Well trajectories could be removed from the possible mechanism list.

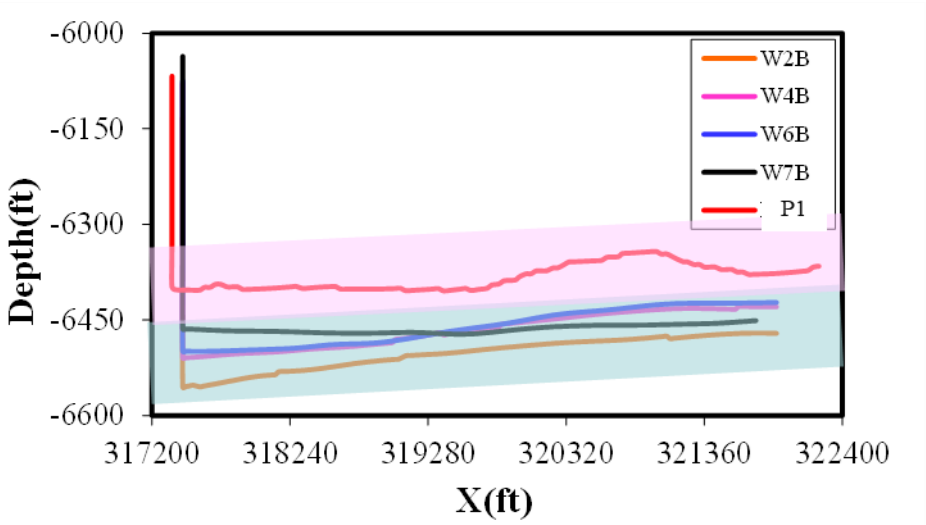

Figure 11 Infill well trajectories in layer 4

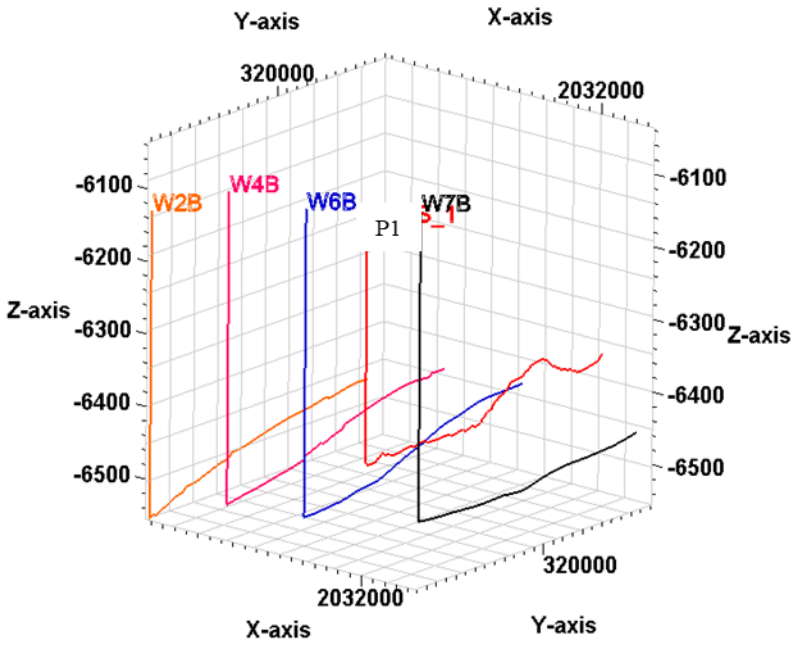

Figure 12 3D view of 4 Infill well trajectories in layer 4

2.2.2 Comparison of operation conditions

Fig. 13 compared the casing pressure of these 6 infill wells. Before July 7, 2017, their casing pressures are almost at the same level, but the production rates of wells W6B and W7B are much lower. So, operation conditions could be removed from the possible mechanism list.

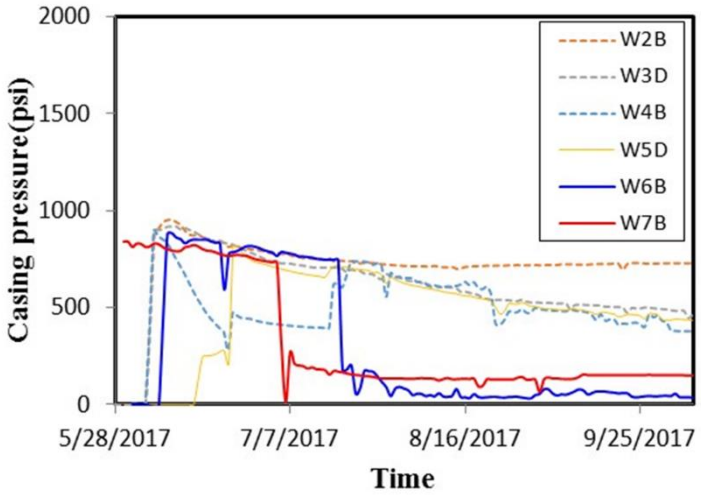

Figure 13 Casing pressure of 7 infill wells

2.2.3 Comparison of the fracturing operation

Table 1 compares the fracturing design of 6 infill wells in terms of length of lateral, depth, number of stages, cluster spacing, and number of fractures. **Table 2** compares the fracturing fluid and proppant. As can be found from these 2 tables, well W6B and W7B were completed with a similar design as other infill wells. So, the fracturing operation could be removed from the possible mechanism list.

Table 1 Comparison of infill well completion designs

Well Name	P1	W2B	W3D	W4B	W5D	W6B	W7B
Length of Lateral, ft	4863	4472	4472	4462	4471	4465	4468
Max Depth (fracture), ft	-6452	-6567	-6476	-6528	-6458	-6526	-6498
Max Depth (Wellbore), ft	-6402	-6550	-6454	-6509	-6417	-6495	-6461
Number of Stages	24	35	35	35	35	35	35
Number of Perf. Clusters (Per Stage)	5	4	4	4	4	4	4
Perf. Cluster Spacing, ft	42	25	25	25	25	25	25
Number of fractures	120	140	140	140	140	140	140

Table 2 Comparison of infill well completion treatments

Well	Slick Water per stage, bbls	Gel per stage, bbls	X-link, bbls
W2B	4421	1203	1174
W3D	4282	1192	1165
W4B	4198	866	1238
W5D	2463	689	2475
W6B	2629	710	2454
W7B	1783	1056	1576

2.3 Stress changes induced by parent well production

The analysis in the second section removes the first 4 possible mechanisms from the list. Now in the rest of this chapter, we are going to justify that it is the stress change

induced by parent well depletion that caused the poor production performance in parent and infill wells.

2.3.1 History matching

The stress calculation is based on the simulation results from reservoir simulation. Before we could use the reservoir simulation results, we need to calibrate the reservoir parameters by doing history matching. The oil production rate is set as the control mode to match BHP, gas/oil ratio, and well water cut.

The reservoir model is as follows. To improve computation efficiency, we did not use the full model. Instead, we cut 3 stages from it and built a model shown in **Fig. 15**. It contains all 6 layers in the vertical direction.

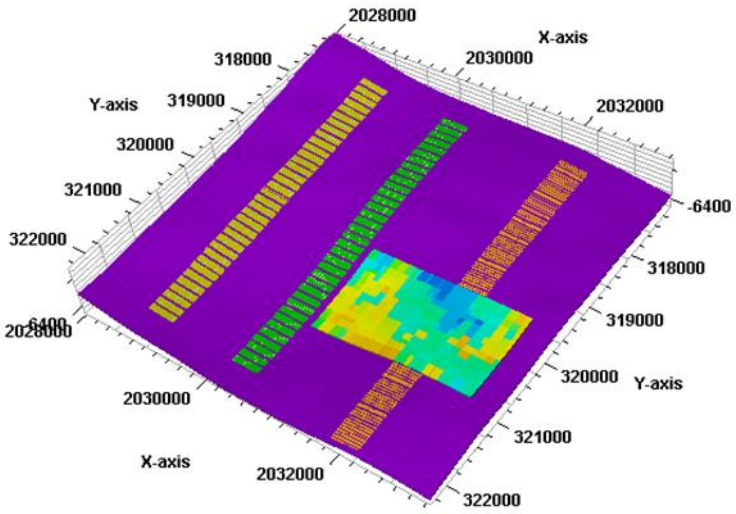

Figure 14 The full reservoir model

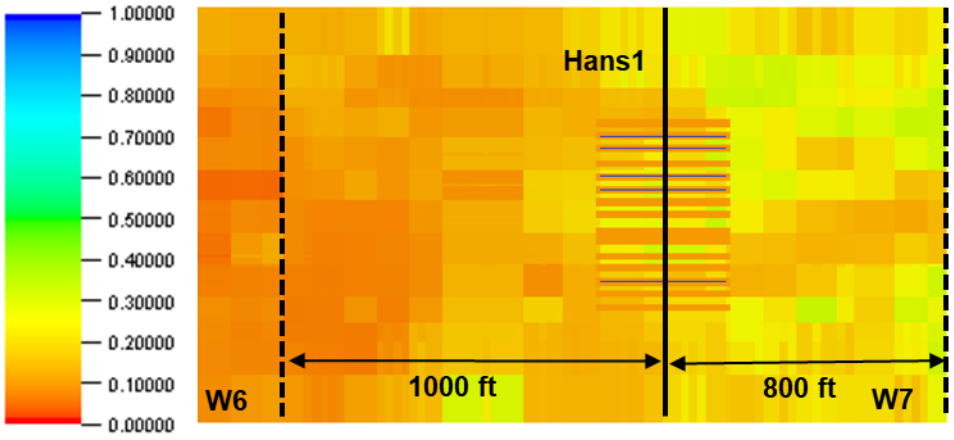

Figure 15 Reservoir model dimension and layout of parent and infill wells (parent well is the solid line, and infill well is the dashed line) with initial water saturation plotted

Table 3 Reservoir parameters calibrated by history matching

Parameter	Values
Long fracture half-length, ft	585
Medium fracture half-length, ft	146
Short fracture half-length, ft	81
Fracture height, layer	3
Matrix K_H multiplier	6.0
Matrix K_V multiplier	0.55
SRV K_H multiplier	3.9
SRV K_V multiplier	3.9
Fracture conductivity, mD-ft	50

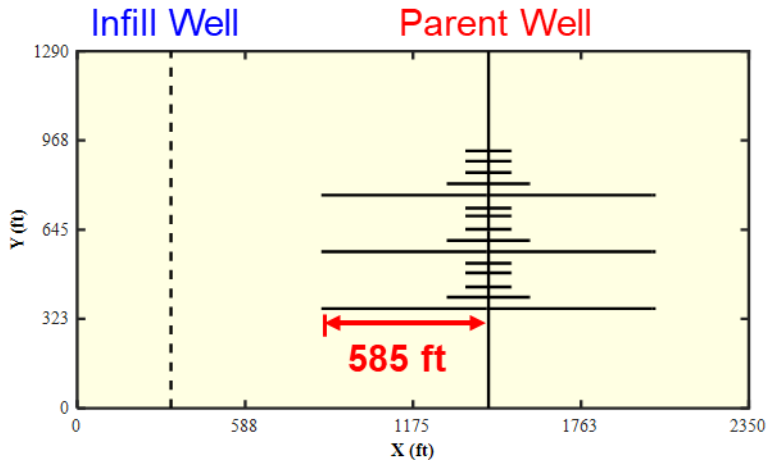

Figure 16 Parent well hydraulic fracture geometry and reservoir dimension

After history matching, the calibrated reservoir parameters are listed in table 3. And fracture geometry is plotted in **Fig. 16**. The simulated and history production curves are as follows.

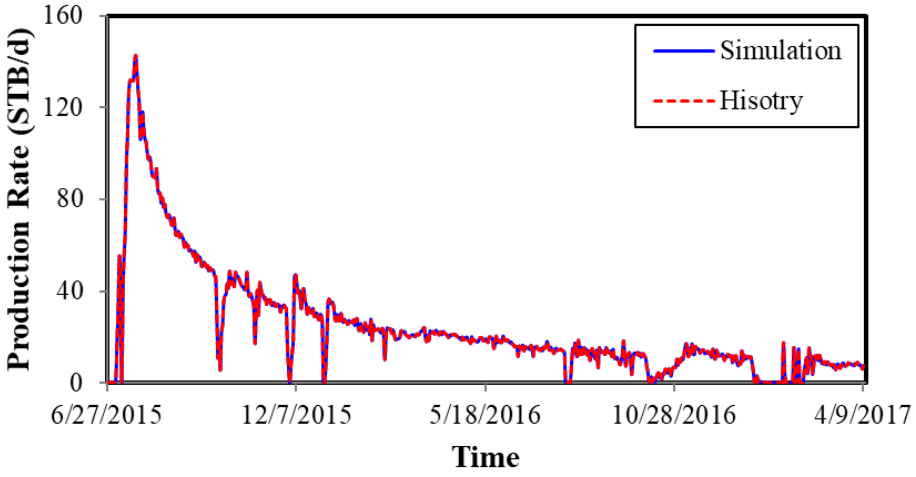

Figure 17 History matching results for oil production rate

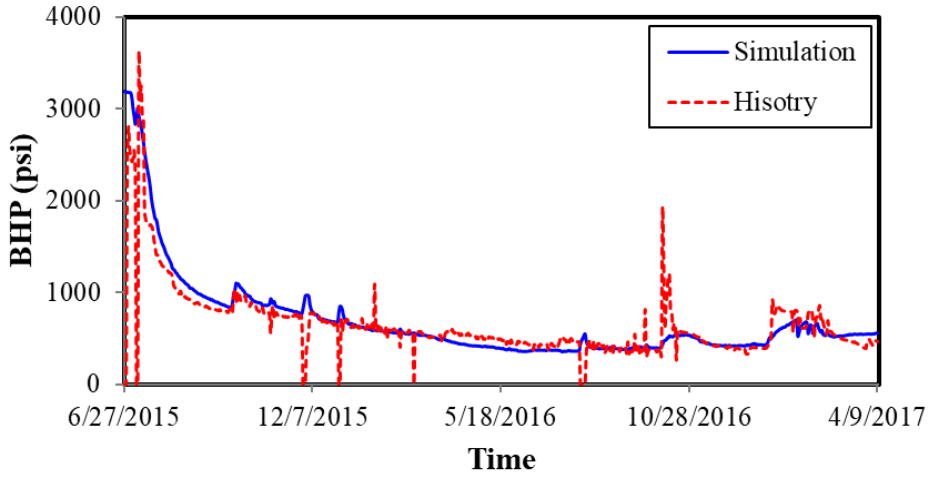

Figure 18 History matching results for bottom hole pressure, psi

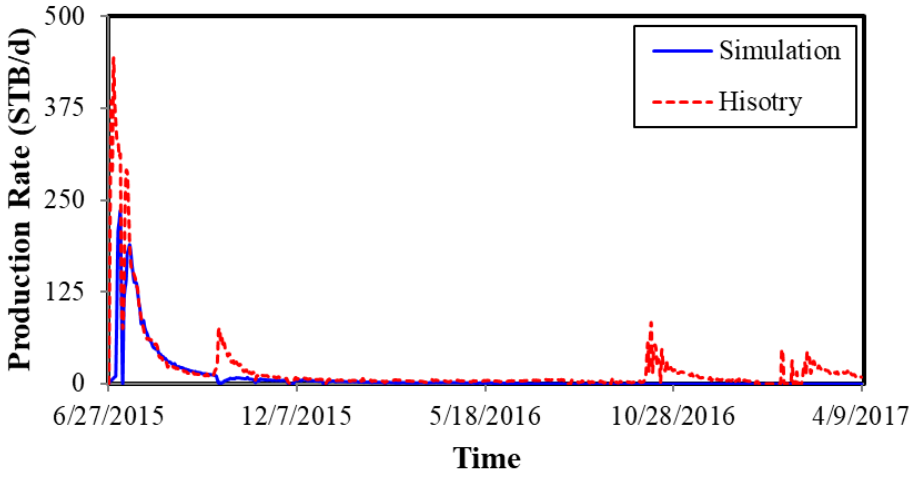

Figure 19 History matching results for water production rate, STB/day

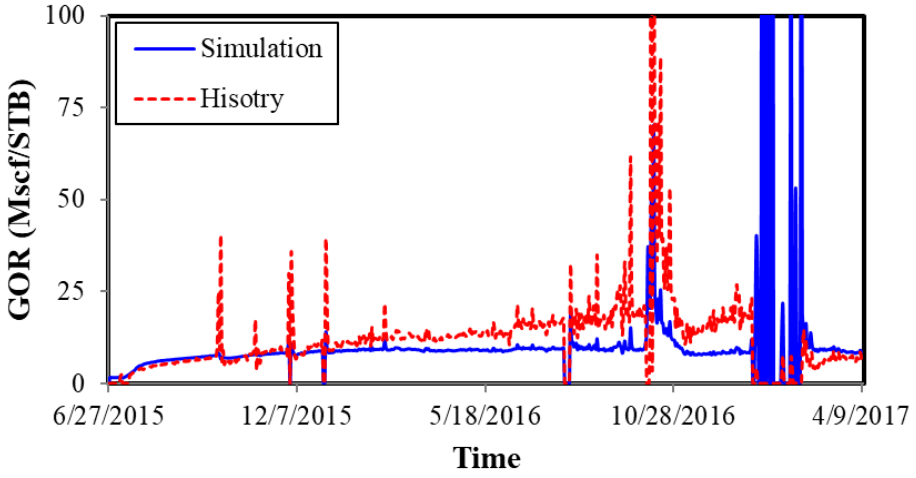

Figure 20 History matching results for Gas/Oil Ratio, Mscf/STB

2.3.2 The geomechanical model

The parameters listed in **Table 4** for geomechanics simulation are determined based on the given reservoir model and available geomechanical well logging reports. Non-displacement is used as the boundary condition.

Table 4 Parameters for geomechanics simulation

Parameter	Value	Unit
Young's modulus	3-8	Mpsi
Poisson's ratio	0.3	-
Permeability(k)	~0.304	μD
Porosity	~0.05	-
S_V	1.03	psi/ft

Table 4 Continued

Parameter	Value	Unit
S_{hmin}	0.583	psi/ft
S_{Hmax}	0.594	psi/ft
Pore Pressure	0.433	psi/ft
Depth of layer 3	~6360	ft

2.3.3 Stress changes caused by parent well production

Once we get the pressure distribution from reservoir simulation, the stress can be readily calculated with geomechanical simulation. The details of stress redistribution induced by parent well production are as follows.

Figs. 21-23 shows the stress and pressure distribution in layer 3. After two years' production of the parent well, a depletion region is generated, and the shape of this depletion region is determined by the geometry of hydraulic fractures (**Fig. 21**). In this depletion region, reservoir pressure drops from initial reservoir pressure of 3100 psi to bottom hole pressure of 700 psi. As the pressure drops, S_{hmin} decreases from 3660 psi to 2590 psi (**Fig. 22**). The S_{Hmax} also decreases from 4040 psi to 2810 psi. This drop mainly occurred near the wellbore (**Fig. 23**).

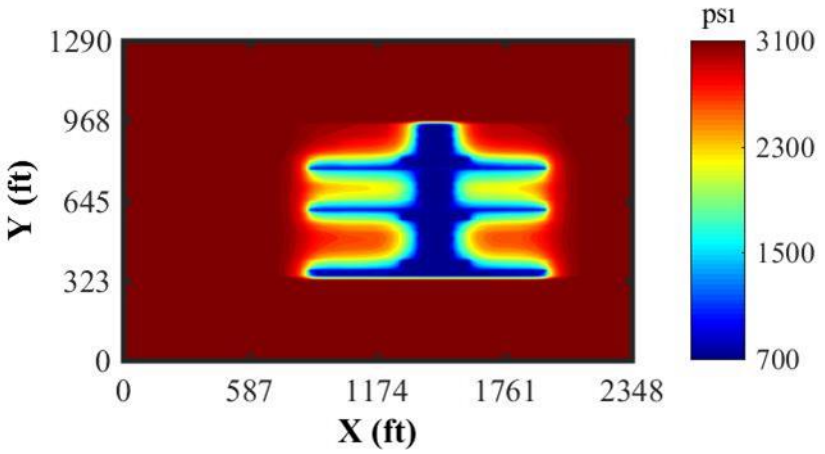

Figure 21 Pressure distribution in layer 3

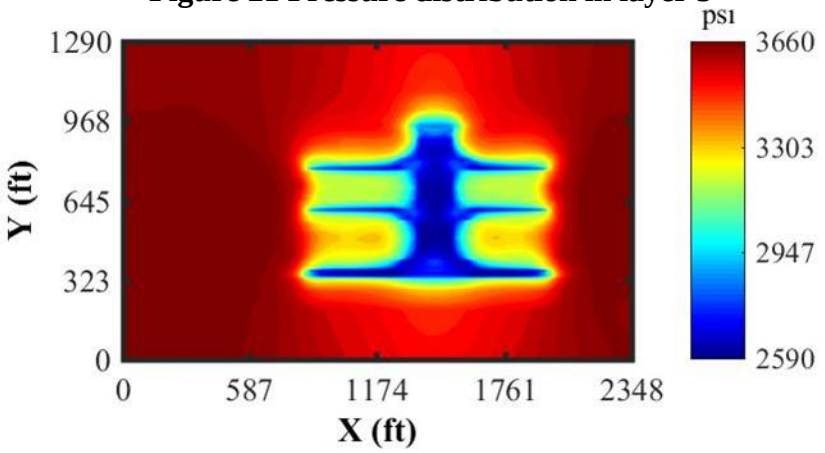

Figure 22 S_{hmin} distribution in layer 3

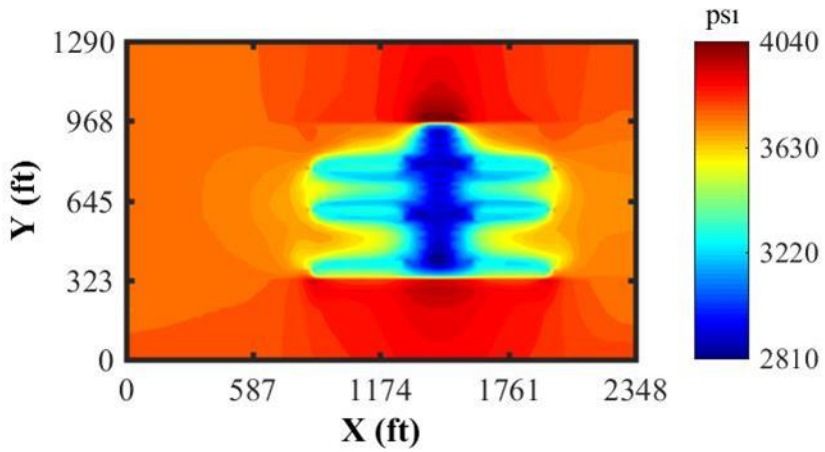

Figure 23 S_{Hmax} distribution in layer 3

Once layer 3 is depleted, a pressure gradient is built up between layer 4 and layer 3, and as a result, the oil and gas in layer 4 flows to layer 3. We expect to find similar stress and pressure distribution in layer 4, but we find different trends in the upper and lower parts of layer 4. **Figs. 24-26** are the pressure and stress in upper layer 4. In this part, both pressure and stress distributions are very similar to layer 3. A depletion region is generated, and within this region both pressure and stress decline, though the drops are relatively small compared to layer 3, which are 900 psi, 400 psi, and 500 psi respectively for pressure, S_{hmin}, and S_{Hmax}.

Figs. 27-29 are the pressure and stress in lower layer 4. In this part, the pressure drop is much smaller (only 140 psi), and the depletion region is also much smaller. In the depletion region, the distribution of S_{hmin} and S_{Hmax} are different from layer 3 and the upper part of layer 4; Instead of decreasing along with pressure, the S_{hmin} is 150 psi higher and S_{Hmax} is 200 psi higher than the surrounding area.

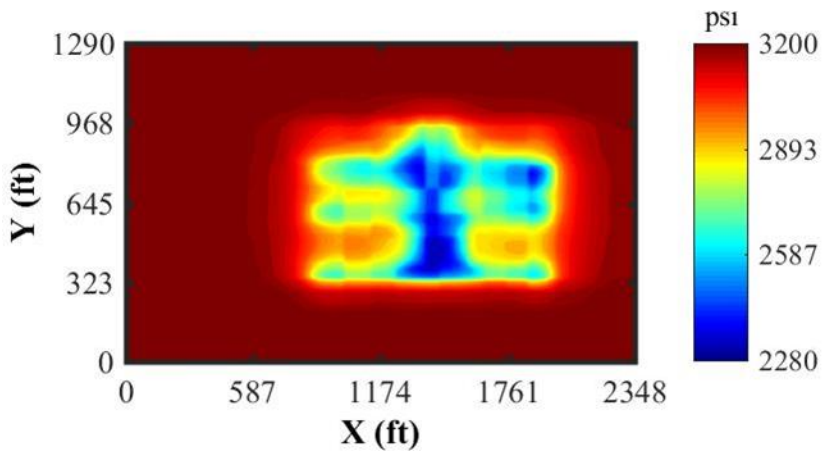

Figure 24 Pressure distribution in upper layer 4

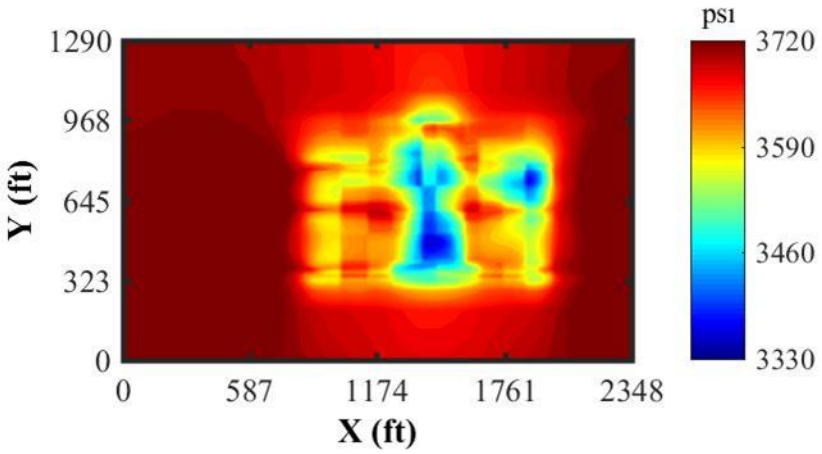

Figure 25 S_{hmin} distribution in upper layer 4

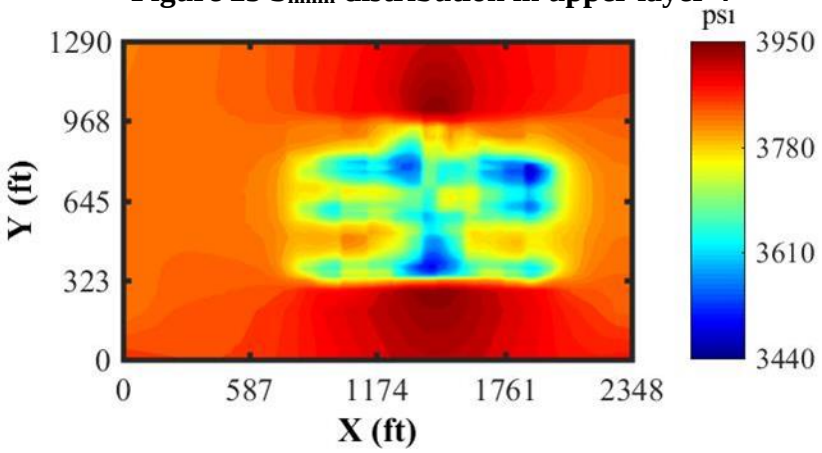

Figure 26 S_{Hmax} distribution in upper layer 4

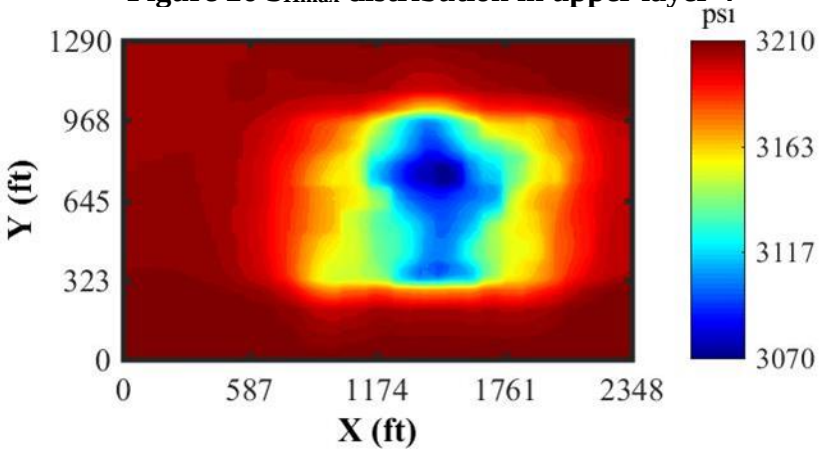

Figure 27 Pressure distribution in lower layer 4

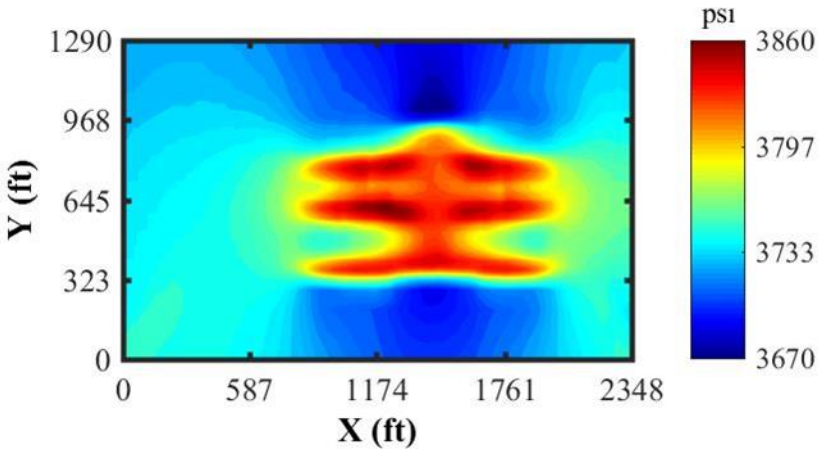

Figure 28 Shmin distribution in lower layer 4

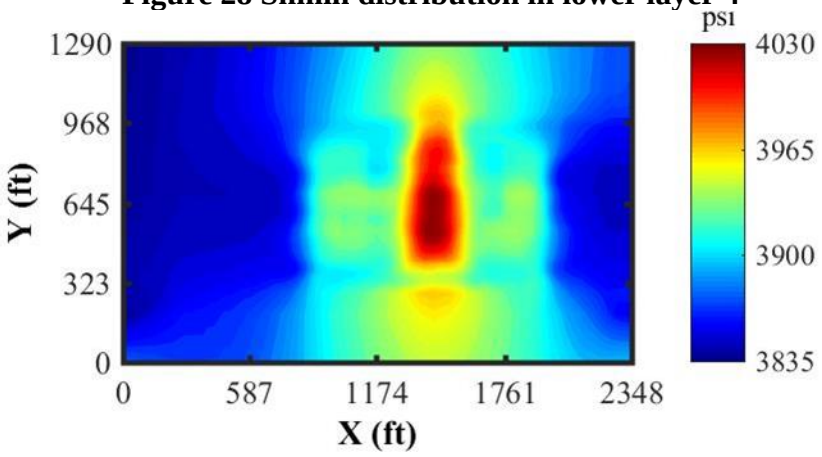

Figure 29 SHmax distribution in lower layer 4

To find out the pressure and stress change in the vertical direction, section views are made in **Figs. 31-33**. The depletion region mainly lies in layer 3, but also extends downward to the upper part of layer 4. The pressure change induces higher S_{hmin} and S_{Hmax} in the region just below the depletion region. How this stress distribution will affect the fracture geometry of infill wells is explained in the next section.

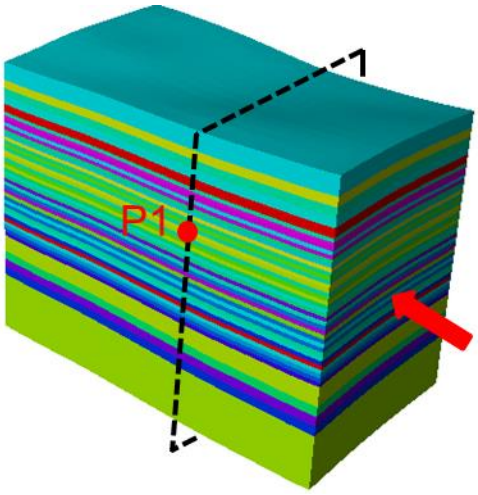

Figure 30 Sketch of the section view

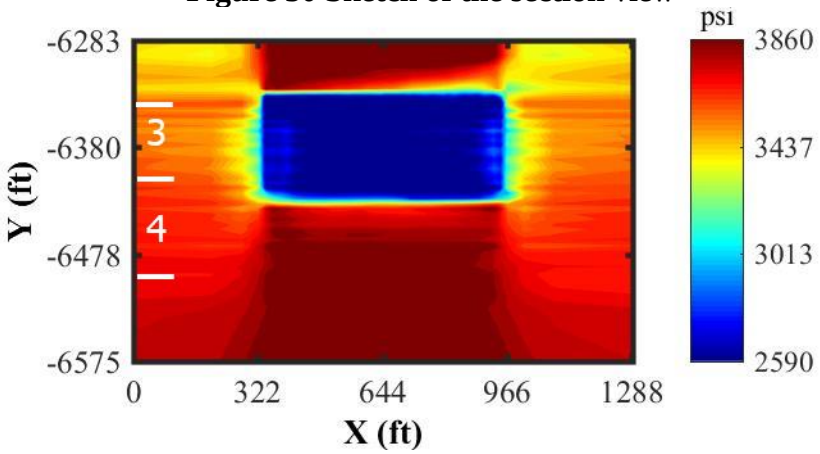

Figure 31 S_{hmin} distribution in the vertical direction

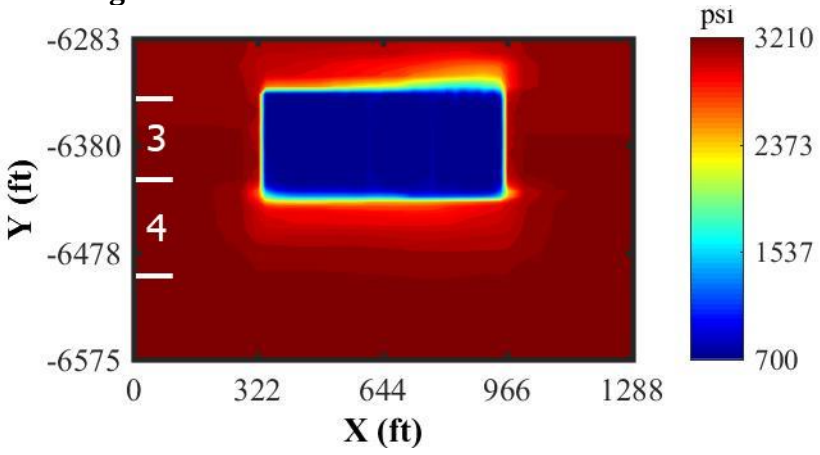

Figure 32 Pressure distribution in the vertical direction

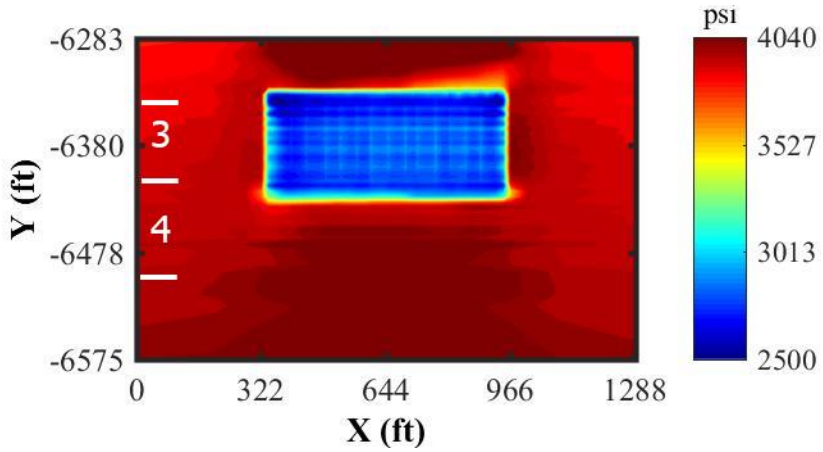

Figure 33 S_{Hmax} distribution in the vertical direction

2.3.4 Fracture swarm effect

To find out the actual fracture geometry underground, ConocoPhillips did a test in its Eagle Ford acreage in north-central DeWitt County, Texas (Raterman et al., 2018). Rock samples are collected from this section (**Fig. 34**). A production well P3 was first drilled. Then to characterize the stimulated reservoir volume of this well, 4 pilot wells were drilled (P1, P2, P4, and P5). Analyzing the rock samples from these 4 pilot wells shows that a hydraulic fracture swarm exists (**Figs. 35 and 36**). In rock samples for well S3, fracture density near the wellbore is much larger than the far-away region. Rock samples also show that hydraulic fractures could be as long as 1500 ft.

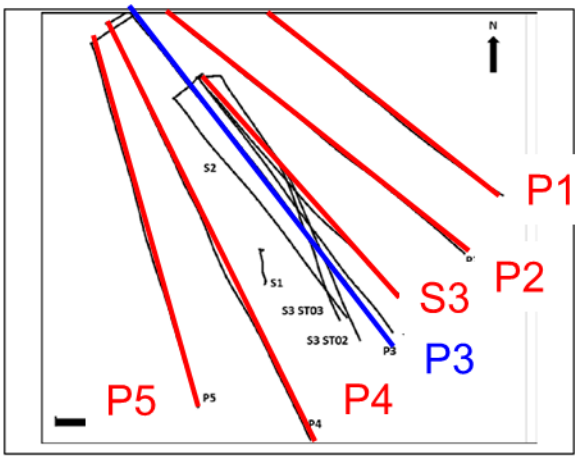

Figure 34 Sketch of pilot wells

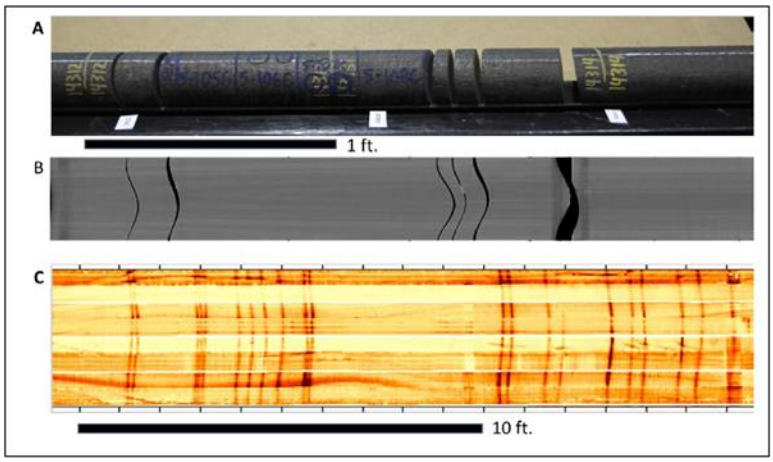

Figure 35 Hydraulic fracture in close association

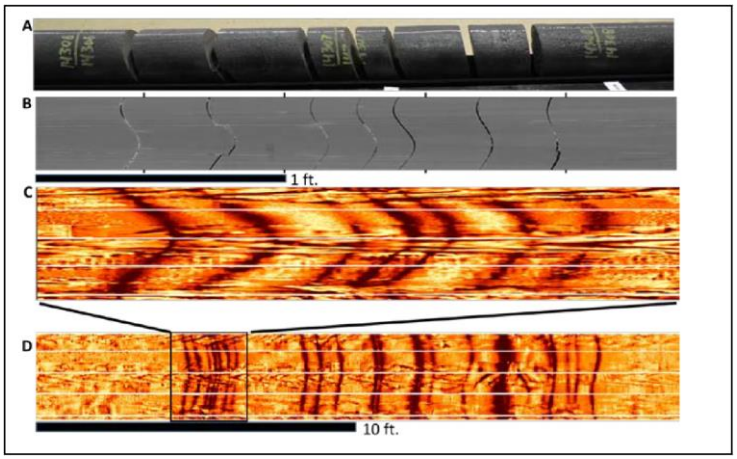

Figure 36 Hydraulic fracture swarm

Considering the hydraulic fracture swarm effect, we redo the history matching using high fracture density and extremely long fractures. The new history matching results are as follows. The longest fracture half-length is 1220 ft. And the number of fractures of the 3 stages could be as many as 200. The solution is not unique. We choose pattern 3 to calculate the stress distribution (**Fig. 37** and **Table 5**).

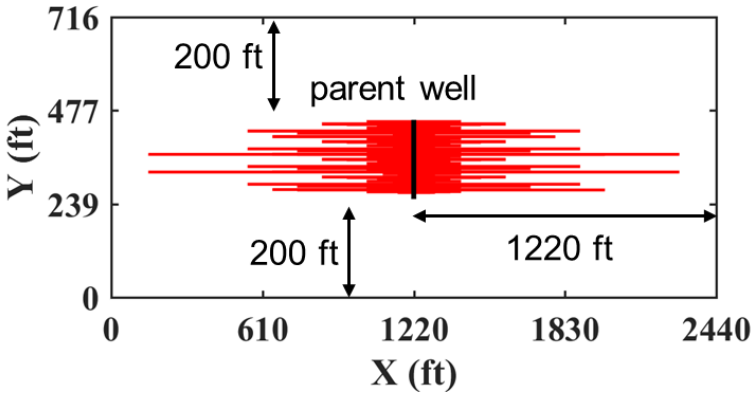

Figure 37 Fracture geometry considering fracture swarm effect

Table 5 Reservoir parameters calibrated by history matching considering fracture swarm

Parameter	Pattern 1	Pattern 2	Pattern 3
Long X_f, ft	1120	1120	1120
Short X_f, ft	75	75	75
Height, layer	3	3	3
Total frac. num.	200	120	120
Matrix K_H multiplier	0.02	0.1	0.5
Matrix K_V multiplier	1	0.5	0.1
HF conductivity, md-ft	1-0.6	0.8-0.08	0.25-0.07

Pressure and stress in layer 3 are plotted in **Figs. 38-40**. Compared to cases not considering the fracture swarm effect, the depletion region is significantly extended due to the increased number of fractures and extremely long hydraulic fractures. The length of the depletion region along the x-axis is about 1400 feet. In the depletion region, S_{Hmax} drops to as low as 2610 psi, and S_{hmin} drops to as low as 2460 psi. When an infill well is drilled near this parent well, it is easier for the infill well fractures to propagate into the depletion region due to the low stress there. When this happens, the infill well hydraulic fractures are not symmetric and more infill fractures will be found in the depletion region. This is detrimental to the production of infill wells as the depletion region has

been produced by the parent well and the infill well fractures are expected to propagate into and then produce the region left by the parent well production.

This altered stress field will also do damage to the parent well production. As more infill well fractures propagate into the depletion region, the possibility of occurrence of frac-hits increases. Once frac-hits occurs, fracturing water from the infill well will flow into the parent well fractures and then is produced from the parent well. This will increase the parent well water production, and at the same time, reduce both oil and gas production from the parent well.

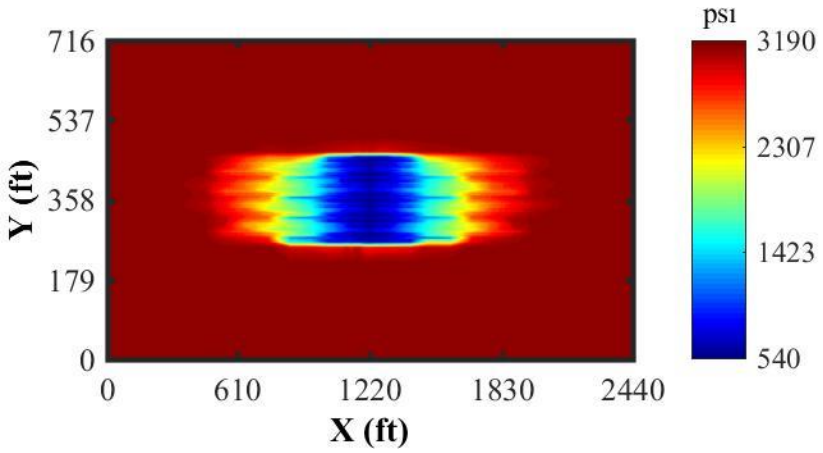

Figure 38 Pressure distribution in layer 3 (swarm effect)

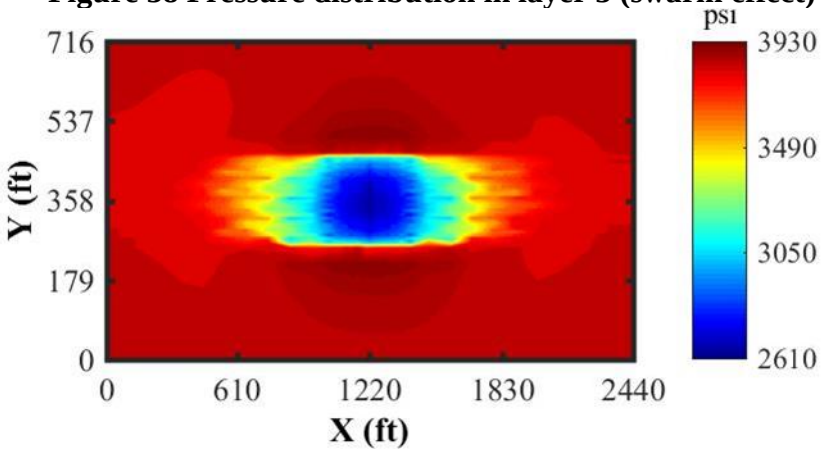

Figure 39 S_{Hmax} distribution in layer 3 (swarm effect)

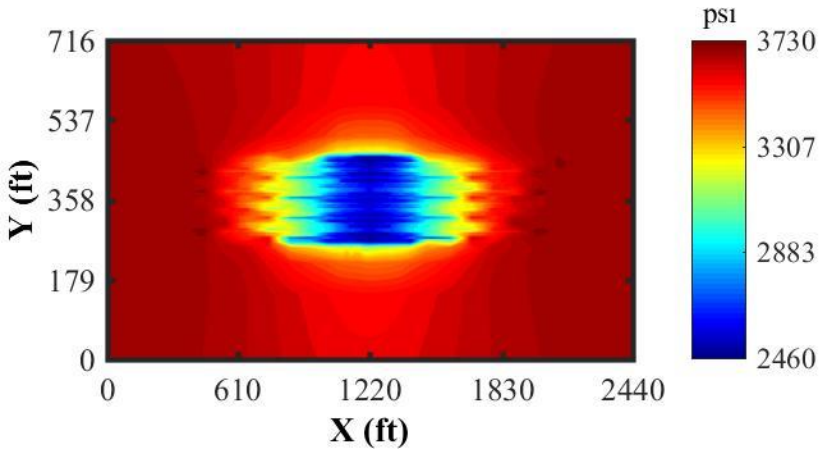

Figure 40 S_{hmin} distribution in layer 3 (swarm effect)

Pressure and stress in layer 4 are plotted in **Figs. 41-43**. In layer 4, the region below the parent well is slightly depleted, and this depletion causes higher stress there than in the surrounding regions. This region is expected to be produced by infill wells drilled in layer 4. But the higher stress there makes the infill well fractures hard to propagate into this region, which will reduce the drainage area available for this infill well and as a result, reduce the infill well production.

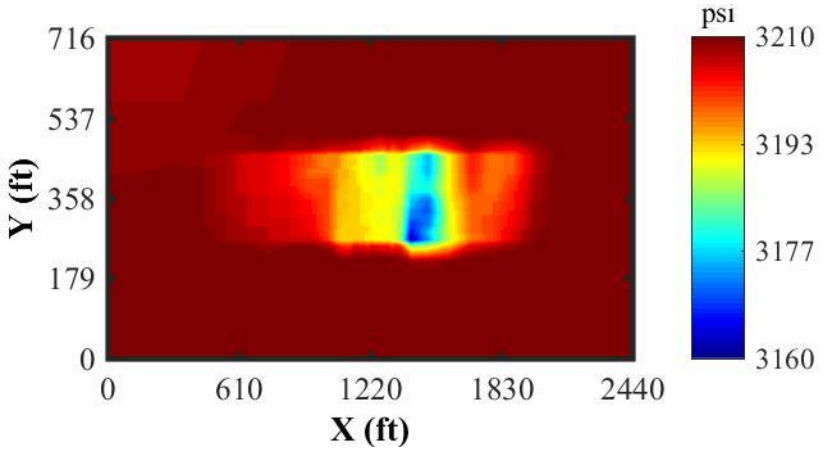

Figure 41 Pressure distribution in layer 4 (swarm effect)

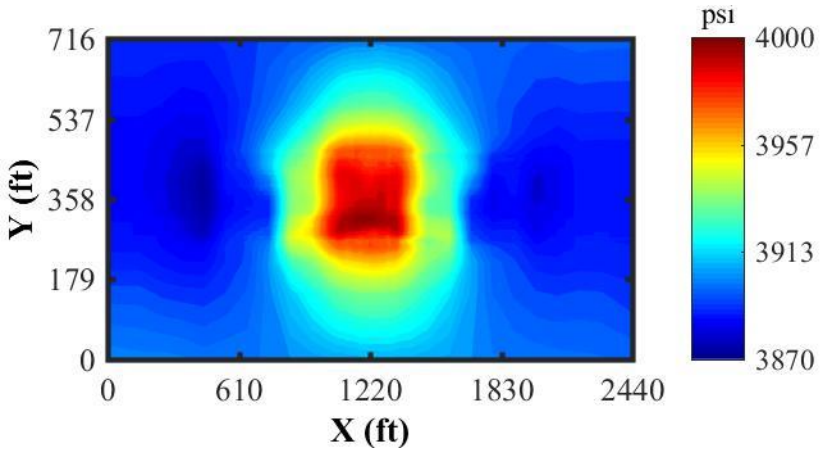

Figure 42 S_{Hmax} distribution in layer 4 (swarm effect)

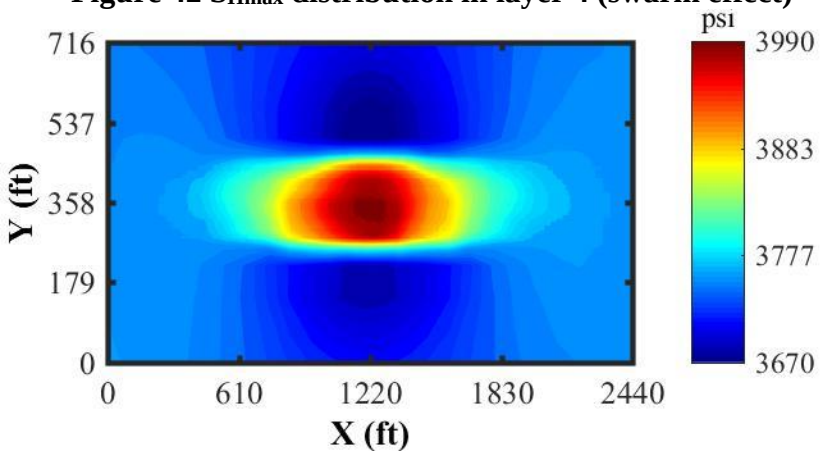

Figure 43 S_{hmin} distribution in layer 4 (swarm effect)

We also plotted the pressure and stress distribution in the vertical direction (**Figs. 44-47**). In the vertical direction, the stress in the region just below the depletion region is higher than the rest part at the same depth; while the stress in layer 3 is much lower than layer 4. This makes the hydraulic fractures of infill wells drilled in layer 4 easier to propagate upward to layer 3, the depleted region. This stress distribution not only will reduce the production of these infill wells as fractures propagate into the depleted region, but also cause production loss in the parent well as the infill well fractures hit the fractures of the parent well.

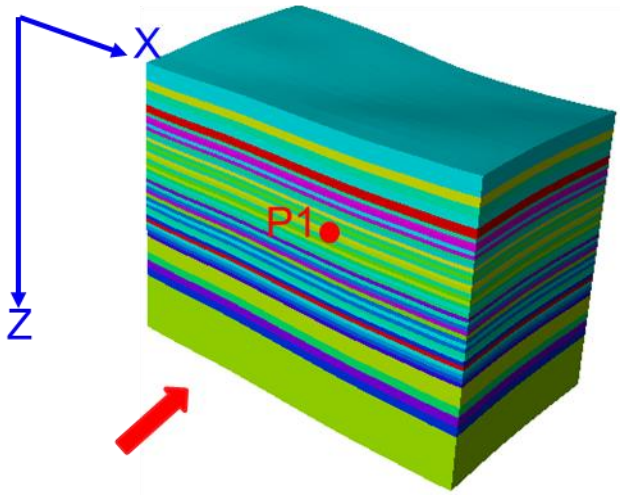

Figure 44 Sketch of the section view (swarm effect)

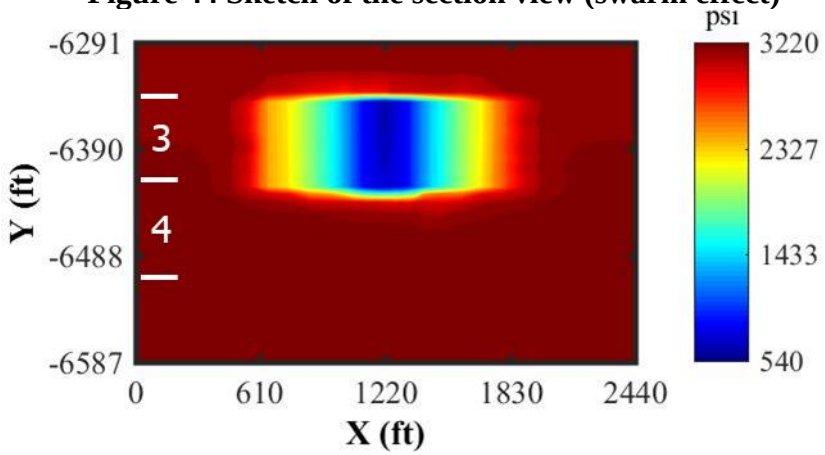

Figure 45 Pressure distribution in the vertical direction (swarm effect)

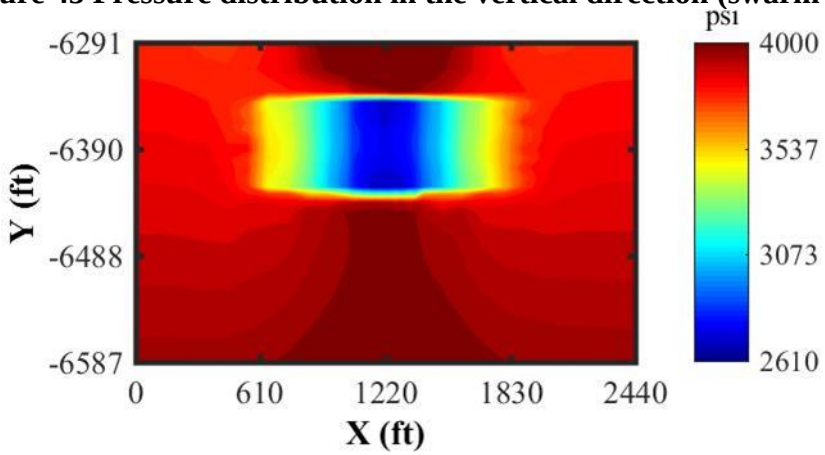

Figure 46 S_{Hmax} distribution in the vertical direction (swarm effect)

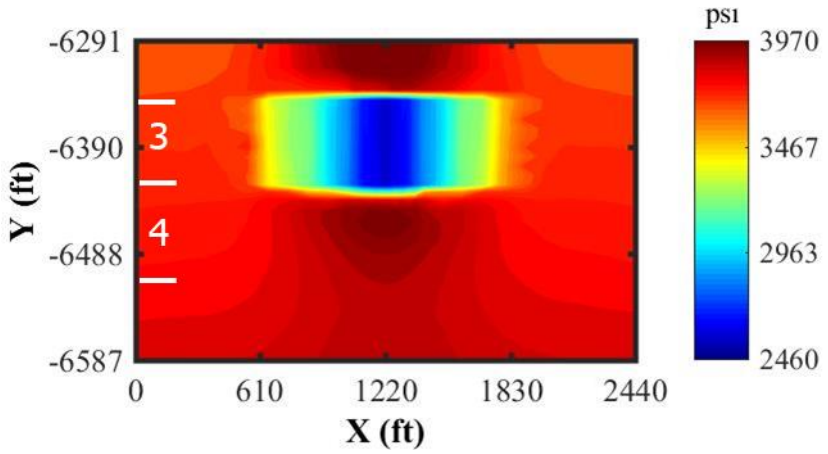

Figure 47 S_{hmin} distribution in the vertical direction (swarm effect)

2.4 Summary

From the above analysis, we conclude

1. Due to non-uniform fracture growth in the parent well, some extreme long fractures are created which induce the irregular depletion area and large stress change region in the reservoir.

2. Due to non-uniform fracture growth, even 1000 ft large well spacing, frac hits still can be induced from the irregular depletion area between the staggered parent and infill wells.

3. Parent well depletion not only changes reservoir stress in the layer of the parent wells, but also alters stress in the lower layer of the infill wells. Stress change favors fracture height in infill wells of layer 4 growing to layer 3 (the depleted region).

4. The altered stress field reduces the drainage area available for infill wells and makes the production from the affected infill wells lower than the rest infill wells.

5. The altered stress field also induces frac-hits between parent and infill well fractures which will increase the parent well water production and decrease the oil/gas production as found in the field observations section.

CHAPTER III

SUBSEQUENT PARENT WELL WATER INJECTION TO RESTORE STRESSES

3.1 Available Mitigation Strategies

In chapter II, the mechanism that caused the poor production performance of infill wells and production loss in parent wells are proposed and verified. In this chapter, the efficiency of subsequent parent well water injection is to be investigated.

Currently, the available mitigation strategies include, but not limited to,

1. Shut-in: to shut in the parent well ahead of infill well activity. This one is the simplest method. But it results in production loss in parent wells.
2. Refracturing: to refracture the parent well after infill frac activity, which is time-consuming and expensive to execute.
3. Subsequent parent well water injection.

My study focuses on the last one. By now, we could find reports on field trials of this strategy from papers. Gakhar et al. (2017) and Whitfield et al. (2018) reported using the subsequent injection in several fields (Karnes, Hawkville, Permian) to prevent parent well production loss and infill well low production rates. We could also find numerical analysis on this topic in papers (Gala et al. (2018), Guo et al. (2018), Kumar et al. (2018).

Based on existing research, this thesis tries to answer the following questions: what are the mechanisms and key factors that control the effectiveness of subsequent parent well water injection? In detail, we are going to investigate 1. what portions of the

depleted region can be restored? 2. How much can the stress magnitude and orientation be restored? 3. The effect of reservoir fluids on stress change?

3.2 Subsequent Water Injection Analysis

The subsequent parent well water injection design is listed in table 6. The Control mode for water injection is constant injection pressure. Here, we tried 3 injection designs with injection pressure ranged from 3200 psi (equal to the initial reservoir pressure) to 3700 psi (just below the Shmin), and injection times ranged from 5 days to 2 weeks.

Table 6 Injection designs (3-phase reservoir)

reservoir fluid type	Pinj, psi	injection time, days	cum liquid, stb per stage	water injected, stb per stage	injection rate, stb/d per stage
gas-oil-water	3200	7	8086	2204	314
	3200	14		3465	247
	3700	5		2244	449

Figs. 48 - 49 are the pressure and S_{hmin} distribution after injection of 1 week with an injection pressure of 3200 psi. The restored region is very small, the width is about 86 ft. The pressure there is increased to 2000 psi, and the S_{hmin} is restored to 3080 psi.

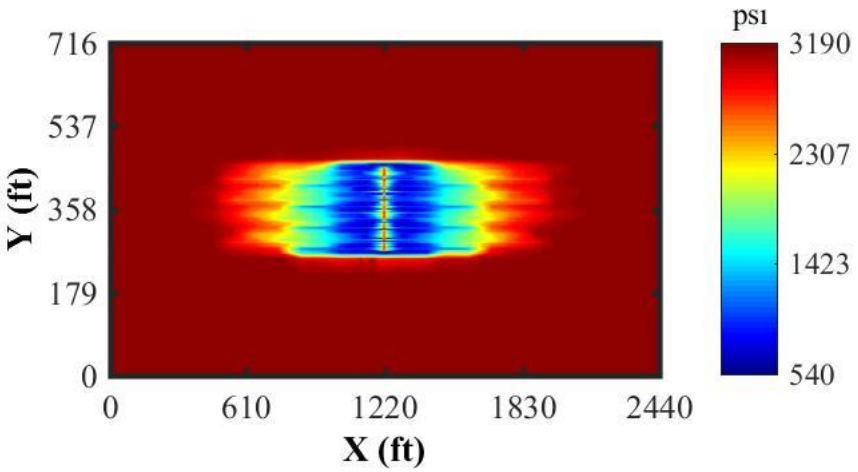

Figure 48 Pressure distribution after injection of 1 week (Pinj = 3200 psi)

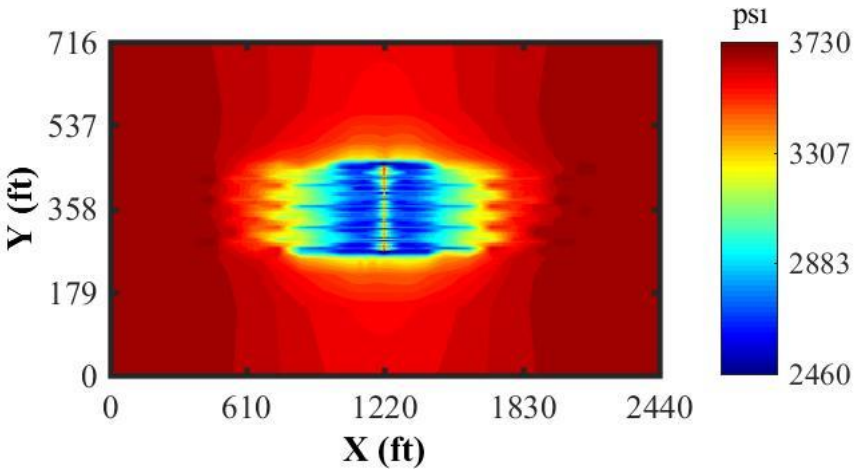

Figure 49 Shmin distribution after injection of 1 week (Pinj = 3200 psi)

As the infill well completion may take weeks to finish, it is important to know how the pressure and stress change during the infill well completion period. For this sake, a soaking period of 1 week is considered. **Figs. 50-51** plotted the pressure and stress after soaking of 1 week. As can be found from the plots, after 1 week's soaking, the restored pressure and stress vanished.

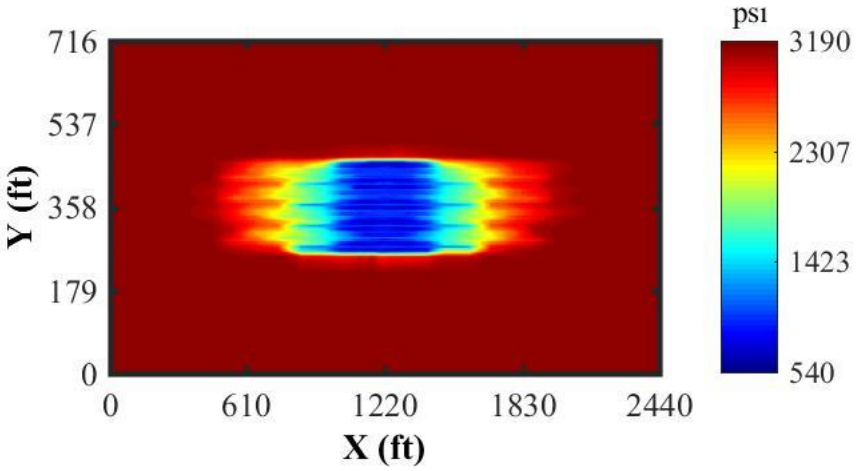

Figure 50 Pressure distribution after soaking of 1 week (Pinj = 3200 psi)

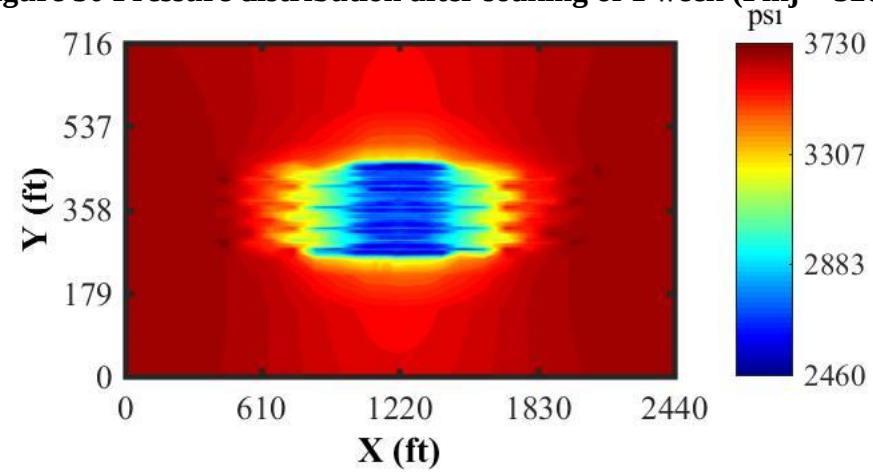

Figure 51 S_{hmin} distribution after soaking of 1 week (Pinj = 3200 psi)

Then we increased the injection time to 2 weeks. The pressure and stress distribution are in **Figs. 52-53**. As more water is injected, the restored region increases to 114ft in width. Pressure there increases to 2195 psi and S_{hmin} increases to 3150 psi. But after soaking for 1 week, the restored region disappears (**Figs. 54-55**).

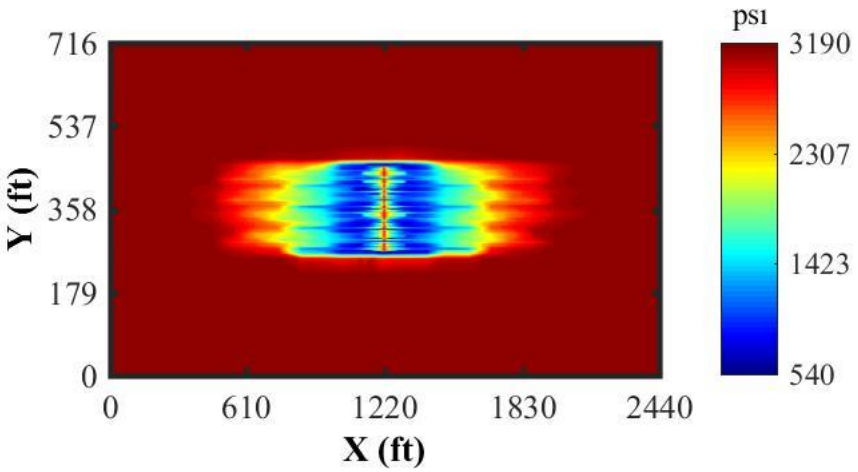

Figure 52 Pressure distribution after injection of 2 weeks (Pinj = 3200 psi)

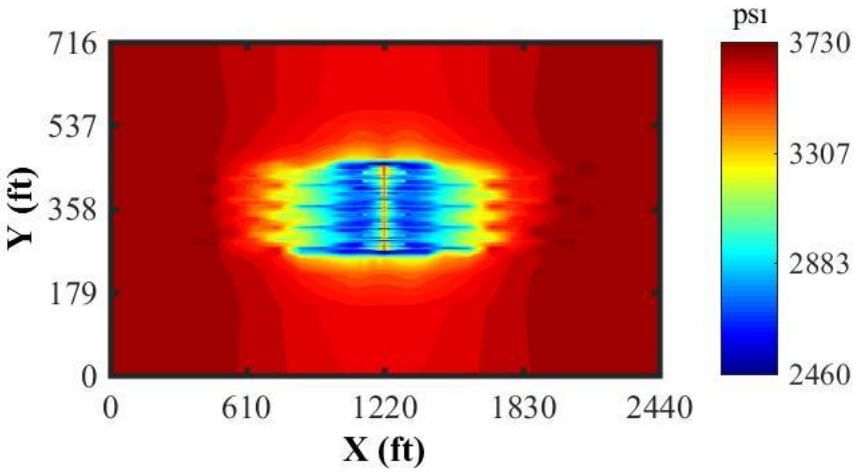

Figure 53 S_{hmin} distribution after injection of 2 weeks (Pinj = 3200 psi)

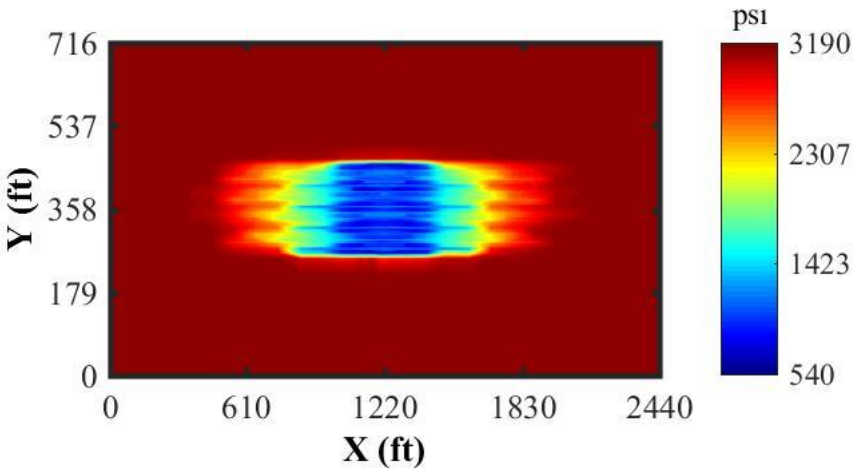

Figure 54 Pressure distribution after soaking of 1 week (Injection of 2 weeks)

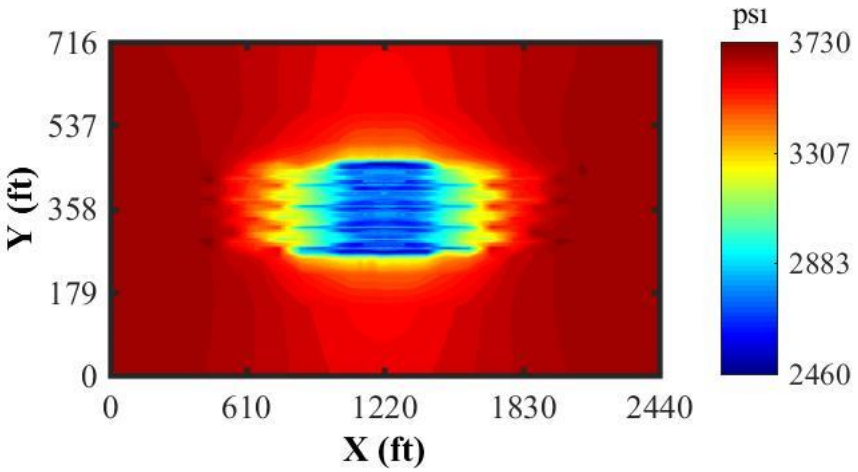

Figure 55 Shmin distribution after soaking of 1 week (Injection of 2 weeks)

The third design is to increase the injection pressure to 3700 psi. The results are plotted in **Figs. 56-59**. This time, though we increase the injection pressure, we could not enlarge the restored region significantly. And after the soaking of 1 week, the restored region vanished too.

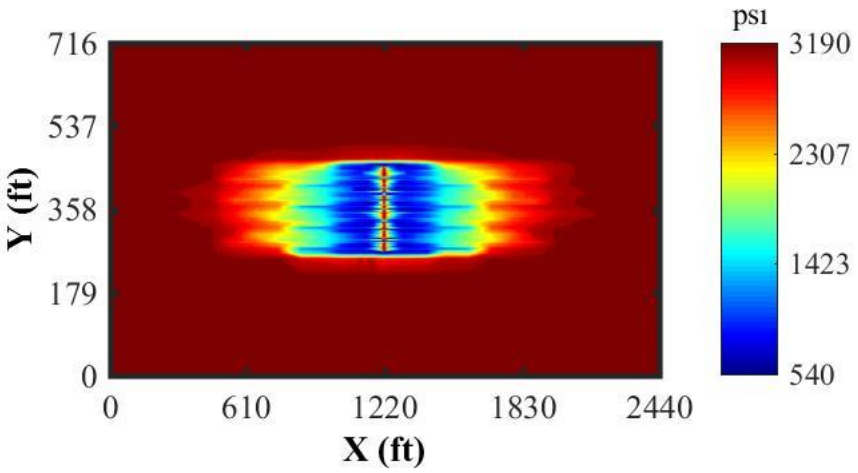

Figure 56 Pressure distribution after injection of 5 days

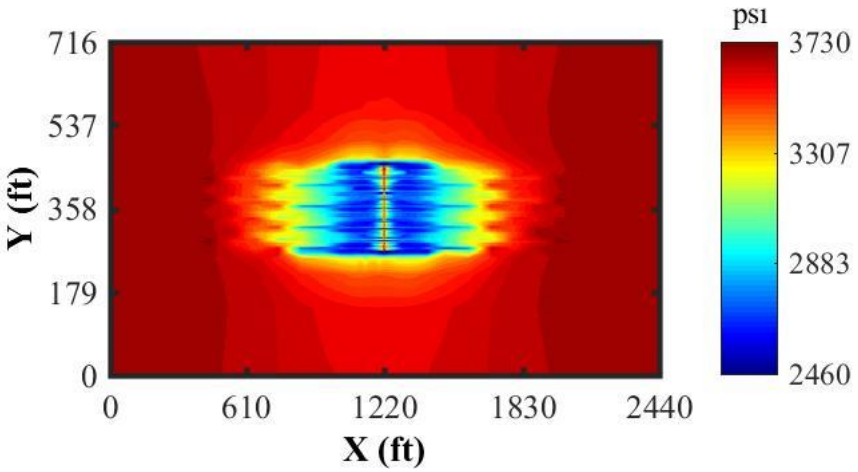

Figure 57 Shmin distribution after injection of 5 days

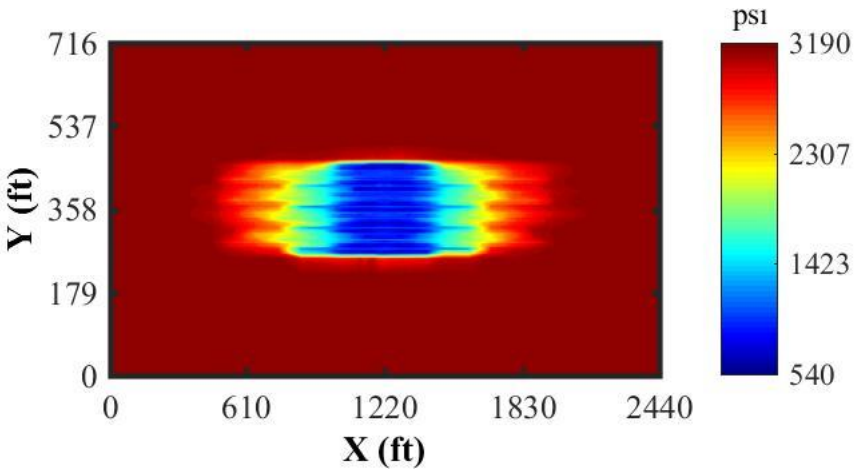

Figure 58 Pressure distribution after soaking of 1 week (Pinj = 3700 psi)

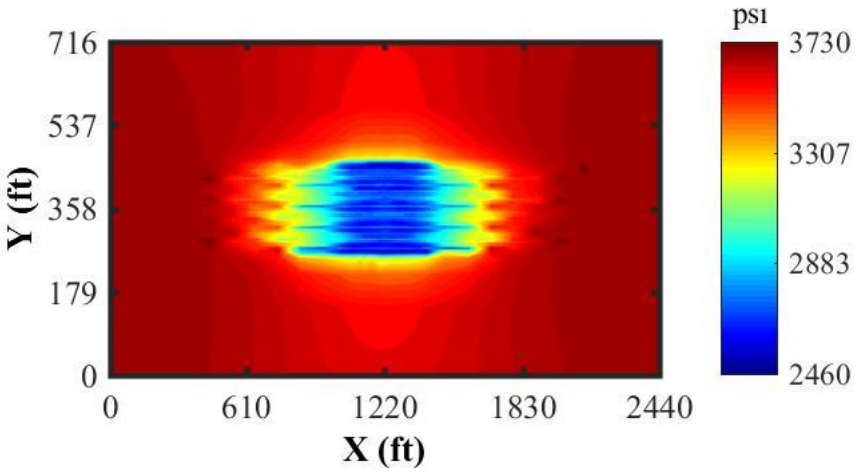

Figure 59 Shmin distribution after soaking of 1 week (Pinj = 3700 psi)

The last factor we consider in subsequent parent well injection is the reservoir fluid type. The original reservoir is a gas-oil-water 3-phase reservoir. Now we build a new oil-water 2-phase model. The only difference is the fluid type. The rest parameters remain the same as the original model.

The pressure and stress distribution of the 2-phase reservoir after production is plotted in **Figs. 60-61**. Compared to the 3-phase model, the depletion region is smaller due to the smaller compressibility of oil and water compared to the gas phase.

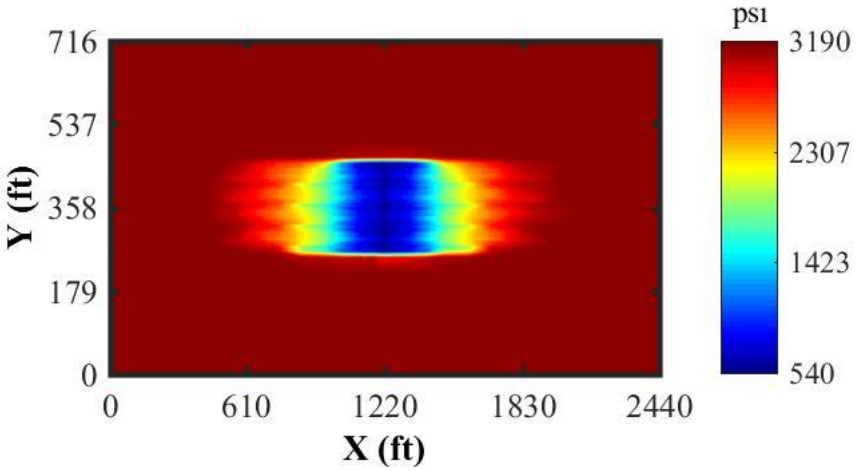

Figure 60 Pressure distribution after production (2-phase)

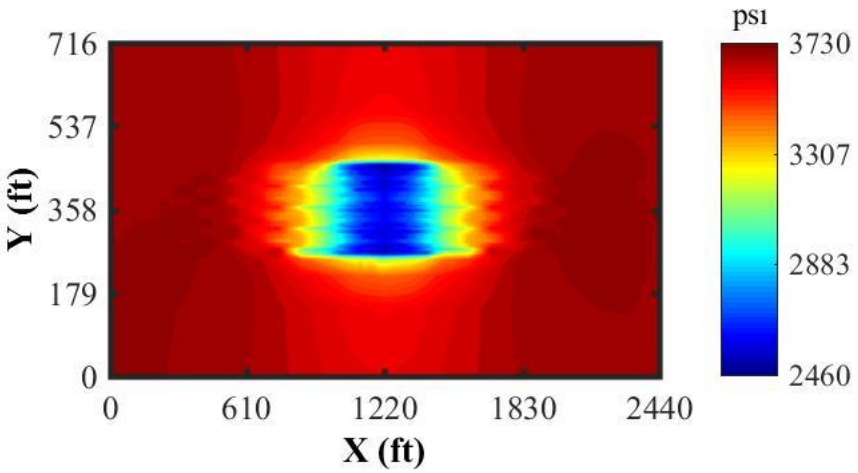

Figure 61 Shmin distribution after production (2-phase)

The injection design for this reservoir is listed in table 7.

Table 7 Injection designs (reservoir fluids)

reservoir fluid type	Pinj, psi	injection time, days	cum liquid, stb per stage	water injected, stb per stage	injection rate, stb/d per stage
gas-oil-water	3200	7	8086	2204	314
	3200	14		3465	247
	3700	5		2244	449
Oil-water	3200	7	13645	1498	214

For this 2-phase model, the effect of subsequent water injection is much better. The width of the restored region is 172 ft. The pressure there increases to 2480 psi (**Fig. 62**) and S_{hmin} is restored to 3300 psi (**Fig. 63**).

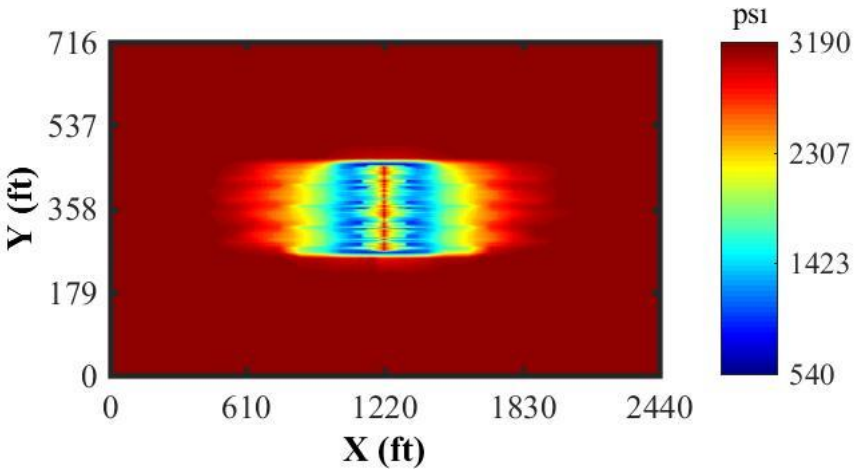

Figure 62 Pressure distribution after injection of 1 week (2-phase)

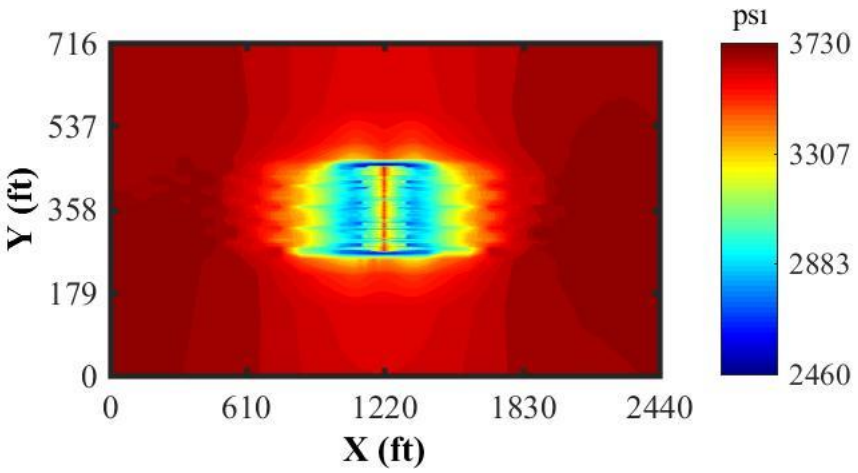

Figure 63 S_{hmin} distribution after injection of 1 week (2-phase)

After soaking for 1 week, though the restored pressure and stress still decrease, it is much better than the 3-phase case (**Figs. 64-65**).

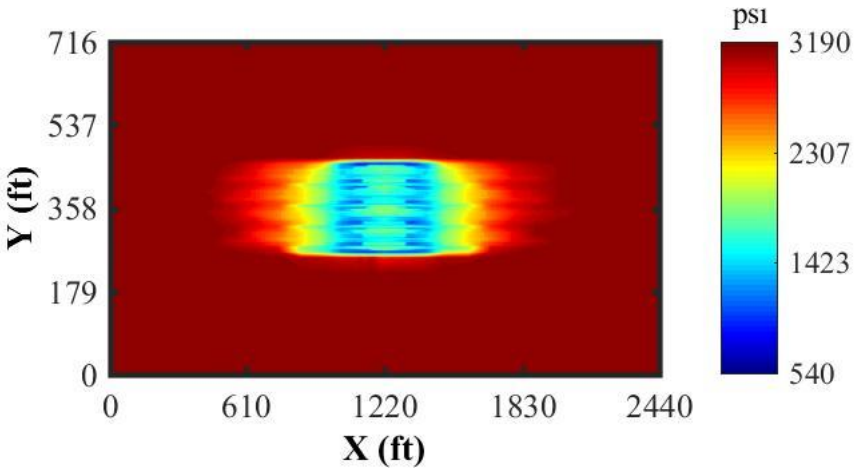

Figure 64 Pressure distribution after soaking of 1 week (2-phase)

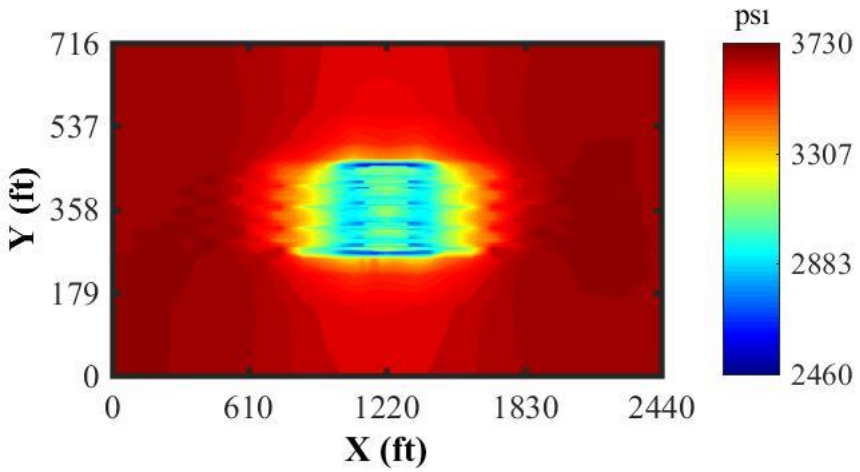

Figure 65 Shmin distribution after soaking of 1 week (2-phase)

The better effect in this oil-water 2-phase reservoir can be explained by the high compressibility of the gas phase. When water is injected into a reservoir with free gas, this free gas will be redissolved into the oil phase, which will generate a large free volume. The injected water then takes the volume left by free gas and does not increase the pressure in the reservoir.

3.3 Summary

Summarizing this subsequent parent well injection analysis, we find

1. After soaking of 1 week, in all cases, a decline of about 1200 psi in pressure and 400 psi in S_{hmin} are observed. This implies that to keep the restored stress during infill well completion, the parent well water injection should not stop.

2. For similar injection volumes, higher injection pressure with shorter injection time can create better pressure and stress recovery than low injection pressure with long injection time.

3. Double injection volume and injection time cannot dramatically improve pressure and stress recovery.

4. Subsequent water injection is more efficient in oil-water two-phase case: better restoration through water injection (i.e. about 400 psi higher in pressure and S_{hmin}) and less decline in soaking period.

CHAPTER IV

FRACTURE CLOSURE SIMULATION

The previous analysis was based on Eclipse and Visage (commercial software for reservoir and geomechanics simulations). The limits of these software's are obvious. For the reservoir simulator, local grid refinement is used to model hydraulic fractures; this increases the size of the problem and the cost of computing. In the reservoir simulation, both the stress-dependent porosity change and the fracture/matrix permeability change with pressure are considered with a rock compaction table. This method assumes the reservoir compressive stress does not change with time. which could not reflect the effect of altered stress on matrix and fracture.

To improve the efficiency and accuracy, a new coupled flow and geomechanics simulator was developed. This new simulator takes advantage of EDFM to model hydraulic fractures to reduce the problem size and save computation time; An algorithm was designed to update fracture conductivity more accurately with pressure and stress calculated.

4.1 Coupled fluid flow and geomechanics

The first job in fracture closure simulator development is to couple the geomechanics simulation to GURU, a compositional reservoir simulator. GURU was developed by Yan. Details could be found in his paper (Yan et al., 2012). My work focuses on the development of the 3D geomechanics simulator.

4.1.1 Equations of 3D geomechanics simulation

The governing equation for geomechanics is based on the quasi-static assumption, written as

$$\mathbf{Div}\,\boldsymbol{\sigma} + \rho_b \boldsymbol{g} = \mathbf{0} \tag{1}$$

Where $\boldsymbol{Div}$ is the divergence operator, $\boldsymbol{\sigma}$ is the total stress tensor, ρ_b is the bulk density, and $\boldsymbol{g}$ is the gravity vector.

Let σ_{ij} denote the stress tensor, let u_i denote the displacement vector, and let ι_i be the prescribed body force per unit volume. The (infinitesimal) strain tensor ε_{ij} is defined to be the symmetric part of the displacement gradients as follows

$$\varepsilon_{ij} = u_{(i,j)} \stackrel{\text{def}}{=} \frac{u_{i,j}+u_{j,i}}{2} \tag{2}$$

Where $i, j = 1,2$ for 2D problems and $i, j = 1,2,3$ for 3D problems.

From the generalized Hooke's law, we could get the relationship between the stress tensor and the strain tensor is defined by:

$$\sigma_{ij} = c_{ijkl}\varepsilon_{kl} \tag{3}$$

Where the c_{ijkl}'s are the elastic coefficients and are given functions of location $\boldsymbol{x} = (x, y, z)$. If we assume the body of interest is isotropic, then

$$c_{ijkl}(\boldsymbol{x}) = \mu(\boldsymbol{x})\left(\delta_{ik}\delta_{jl} + \delta_{il}\delta_{jk}\right) + \lambda(\boldsymbol{x})\delta_{ij}\delta_{kl} \tag{4}$$

Where μ is called the shear modulus and denoted by G in reservoir engineering. λ is the Lame parameter. They are given as functions of Young's Modulus *E*, and Poisson's ratio *s* as

$$\lambda = \frac{\nu \mathrm{E}}{(1+\nu)(1-2\nu)} \tag{5}$$

$$\mu = \frac{E}{2(1+\nu)} \tag{6}$$

By the definition of the divergence of rank-2 tensors, in a Cartesian coordinate system, the divergence of a second rank tensor can be written as

$$div(S) = \frac{\partial S_{ki}}{\partial x_k}\boldsymbol{e}_i = S_{ki,k}\boldsymbol{e}_i \tag{7}$$

In the above equation, i is the direction and k is the direction of the face and so it takes the "on-in" notation. Then, the governing equation (1) can be split into 3 directions. For direction i, we have

$$S_{ij,j}e_i + \rho_b g_i = 0 \tag{8}$$

Replace S with σ, we have

$$\sigma_{ij,j} + \iota_i = 0 \tag{9}$$

In Equation (9), the extended-expression of $\sigma_{ij,j}$ is

$$\sigma_{ij,j} = \frac{\partial \sigma_{i1}}{\partial x_1} + \frac{\partial \sigma_{i2}}{\partial x_2} + \frac{\partial \sigma_{i3}}{\partial x_3} \tag{10}$$

This follows the Einstein Summation Convention: repeated indices in any single term imply summation for that term over the full range of that index.

The geomechanics simulation is to calculate the displacements and stress with specified boundary conditions. From Equation (9), a formal statement of the strong form of the boundary-value problem goes as follows:

$$(S)\begin{cases} Given\ \iota_i: \Omega \to R, q_i: \Gamma_{qi} \to R, and\ h_i: \Gamma_{hi} \to R, find\ u_i: \overline{\Omega} \to R\ such\ that \\ \sigma_{ij,j} + \iota_i = 0\ in\ \Omega\ (equilibrium\ equation) \\ u_i = q_i\ on\ \Gamma_{qi} \\ \sigma_{ij}n_j = h_i\ on\ \Gamma_{hi} \\ where\ \sigma_{ij}\ is\ defined\ in\ terms\ of\ u_i \end{cases}$$

Where Ω is the domain of continuum (the reservoir in our reservoir simulation), Γ_{qi} is the boundary where displacement is specified, Γ_{hi} is the boundary where force acting on the surface is specified. The notations used in this chapter follow the "in-on" rule, which means i is direction, j is the direction of the face.

Recall the integration by parts formula for higher dimensions

$$\int_{\Omega} \frac{\partial u}{\partial x_i} v \, d\Omega = \int_{\Gamma} uv\vec{n}_i \, d\Gamma - \int_{\Omega} u \frac{\partial v}{\partial x_i} d\Omega \tag{11}$$

where $\vec{n}$ is the outward unit surface normal to Γ, $\vec{n}_i$ is its i-th component and i ranges from 1 to n_{sd} (the dimension of space). In coupled flow and geomechanics simulation, when displacement boundary conditions are used, it is usually no displacement there, i.e. $q_i = 0 \; on \; \Gamma_{qi}$. Applying Equation (11) to the strong form and assume $u_i = q_i = 0 \; on \; \Gamma_{qi}$, we have

$$\int_{\Omega} w_i \, \sigma_{ij,j} d\Omega + \int_{\Omega} w_i \, \iota_i d\Omega = 0 \tag{12}$$

$$\int_{\Gamma} \sigma_{ij} w_i \vec{n}_j \, d\Gamma \; - \int_{\Omega} \sigma_{ij} w_{i,j} \, d\Omega + \int_{\Omega} w_i \, \iota_i d\Omega = 0 \tag{13}$$

$$\int_{\Gamma_{hi}} w_i h_i \, d\Gamma - \int_{\Omega} \sigma_{ij} w_{i,j} \, d\Omega + \int_{\Omega} w_i \, \iota_i d\Omega = 0 \tag{14}$$

Where $\sigma_{ij} n_j = h_i \; on \; \Gamma_{hi}$. w_i is the test function and $w_i = u_i = q_i = 0 \; on \; \Gamma_{qi}$. It is important to note that both i and j are repeated in this equation.

Define $w_{(i,j)}$ to be the symmetric part of $w_{i,j}$ as

$$w_{(i,j)} \stackrel{\text{def}}{=} \frac{w_{i,j} + w_{j,i}}{2} \tag{15}$$

As σ_{ij} is symmetric, then $\sigma_{ij} w_{i,j} = \sigma_{ij} w_{(i,j)}$. Apply it to Equation (14), we get

$$\int_{\Gamma_{hi}} w_i h_i \, d\Gamma - \int_{\Omega} \sigma_{ij} w_{(i,j)} \, d\Omega + \int_{\Omega} w_i \, \iota_i d\Omega = 0 \tag{16}$$

Now the weak formulation can be stated as:

$$(W)\begin{cases} Given\ \iota_i: \Omega \to R, q_i: \Gamma_{qi} \to R, and\ h_i: \Gamma_{hi} \to R, find\ u_i \in U_i\ such\ that\ for\ all\ w_i \in V_i, \\ \int_\Omega w_{(i,j)}\, \sigma_{ij} d\Omega = \int_\Omega w_i\, \iota_i d\Omega + \sum_{i=1}^{n_{sd}} \left(\int_{\Gamma_{hi}} w_i h_i d\Gamma \right) \\ where\ \sigma_{ij}\ is\ defined\ in\ terms\ of\ u_i \end{cases}$$

To make the formula compact, the following abstract notations are used in the following derivation,

$$a(\boldsymbol{w}, \boldsymbol{u}) = \int_\Omega w_{(i,j)} c_{ijkl} u_{(k,l)} d\Omega \tag{17}$$

$$(\boldsymbol{w}, \boldsymbol{\iota}) = \int_\Omega w_i l_i d\Omega \tag{18}$$

$$(\boldsymbol{w}, \boldsymbol{h})_\Gamma = \sum_{i=1}^{n_{sd}} \left(\int_{\Gamma_{hi}} w_i h_i d\Gamma \right) \tag{19}$$

Then, the weak form could be concisely stated as

$$(W)\begin{cases} Given\ \boldsymbol{\iota}, \boldsymbol{q}\ and\ \boldsymbol{h}\big(in\ which\ the\ components\ are\ defined\ in\ (W)\big), \\ find\ \boldsymbol{u} \in U\ such\ that\ for\ all\ \boldsymbol{w} \in V, \\ a(\boldsymbol{w}, \boldsymbol{u}) = (\boldsymbol{w}, \boldsymbol{\iota}) + (\boldsymbol{w}, \boldsymbol{h})_\Gamma \end{cases}$$

To improve the computation efficiency, it is favorable to construct index-free counterparts of the above expressions. For example, for the 2D problems, i.e., $n_{sd} = 2$; $1 \le i, j, k, l \le 2$. Then, we have the following definitions.

$$\varepsilon(\boldsymbol{u}) = \{\varepsilon_I(\boldsymbol{u})\} = \begin{Bmatrix} u_{1,1} \\ u_{2,2} \\ u_{1,2} + u_{2,1} \end{Bmatrix}$$

$$\varepsilon(\boldsymbol{w}) = \{\varepsilon_I(\boldsymbol{w})\} = \begin{Bmatrix} w_{1,1} \\ w_{2,2} \\ w_{1,2} + w_{2,1} \end{Bmatrix}$$

$$\boldsymbol{D} = [D_{IJ}] = \begin{bmatrix} D_{11} & D_{12} & D_{13} \\ & D_{22} & D_{23} \\ sym & & D_{33} \end{bmatrix}$$

ε is the vector of displacements. Note that factors of one-half have been eliminated from the shearing components (i.e., last components in the strain vectors). Recall the definition of strain as a function of displacement.

$$\varepsilon_{ij} = u_{(i,j)} \stackrel{\text{def}}{=} \frac{u_{i,j}+u_{j,i}}{2} \tag{2}$$

These factors of one-half have been merged to matrix $\boldsymbol{D}$. This way ε only contains displacements which are the unknowns in geomechanics simulation. $\boldsymbol{D}$ is the matrix for elastic coefficients. Note that matrix $\boldsymbol{D}$ is symmetric, so only half of it is explicitly shown.

Now $a(\boldsymbol{w},\boldsymbol{u})$ can be rewritten in terms of $\varepsilon(\boldsymbol{u})$, $\varepsilon(\boldsymbol{w})$ and $\boldsymbol{D}$.

$$w_{(i,j)}c_{ijkl}u_{(k,l)} = \varepsilon(\boldsymbol{w})^T\boldsymbol{D}\varepsilon(\boldsymbol{u})$$

$$= \begin{Bmatrix} w_{1,1} \\ w_{2,2} \\ w_{1,2}+w_{2,1} \end{Bmatrix}^T \begin{bmatrix} D_{11} & D_{12} & D_{13} \\ & D_{22} & D_{23} \\ sym & & D_{33} \end{bmatrix} \begin{Bmatrix} u_{1,1} \\ u_{2,2} \\ u_{1,2}+u_{2,1} \end{Bmatrix} \tag{20}$$

$$= \{w_{1,1} \quad w_{2,2} \quad w_{1,2}+w_{2,1}\} \begin{Bmatrix} D_{11}u_{1,1}+D_{12}u_{2,2}+D_{13}(u_{1,2}+u_{2,1}) \\ D_{21}u_{1,1}+D_{22}u_{2,2}+D_{23}(u_{1,2}+u_{2,1}) \\ D_{31}u_{1,1}+D_{32}u_{2,2}+D_{33}(u_{1,2}+u_{2,1}) \end{Bmatrix}$$

And so

$$a(\boldsymbol{w},\boldsymbol{u}) = \int_\Omega \varepsilon(\boldsymbol{w})^T\boldsymbol{D}\varepsilon(\boldsymbol{u})d\Omega \tag{21}$$

For 3D problems ($n_{sd} = 3$), we could get the same equation with an updated definition of $\varepsilon(\boldsymbol{u})$ as follows.

$$\varepsilon(\boldsymbol{u}) = \begin{Bmatrix} u_{1,1} \\ u_{2,2} \\ u_{3,3} \\ u_{2,3}+u_{3,2} \\ u_{1,3}+u_{3,1} \\ u_{1,2}+u_{2,1} \end{Bmatrix} \tag{22}$$

And for 3D problems, the elastic coefficients matrix $\boldsymbol{D}$ now is a 6×6 matrix.

$$D = \begin{bmatrix} K+\frac{4}{3}\mu & K-\frac{2}{3}\mu & K-\frac{2}{3}\mu & 0 & 0 & 0 \\ K-\frac{2}{3}\mu & K+\frac{4}{3}\mu & K-\frac{2}{3}\mu & 0 & 0 & 0 \\ K-\frac{2}{3}\mu & K-\frac{2}{3}\mu & K+\frac{4}{3}\mu & 0 & 0 & 0 \\ 0 & 0 & 0 & \mu & 0 & 0 \\ 0 & 0 & 0 & 0 & \mu & 0 \\ 0 & 0 & 0 & 0 & 0 & \mu \end{bmatrix} \tag{23}$$

Where K is the Bulk modulus defined as

$$K = \frac{E}{3(1-2\nu)} \tag{24}$$

The body force term $(\boldsymbol{w}, \boldsymbol{\iota})$ accounts for the effect of gravity. For our reservoir engineering problems, gravity is far smaller than stress calculated, so this term is usually ignored. Then the weak form (W) could be reduced to

$$(W)\begin{cases} Given\ \boldsymbol{\iota}, \boldsymbol{q}\ and\ \boldsymbol{h}, \\ find\ \boldsymbol{u} \in U\ such\ that\ for\ all\ \boldsymbol{w} \in V, \\ a(\boldsymbol{w}, \boldsymbol{u}) = (\boldsymbol{w}, \boldsymbol{h})_{\Gamma} \end{cases}$$

4.1.2 Numerical implementation

The finite element method is commonly used for geomechanics simulation. The Galerkin formulation of the weak form is given as follows

$$(W)\begin{cases} Given\ \boldsymbol{h}, find\ \boldsymbol{u}^h = \boldsymbol{v}^h \in U^h\ such\ that\ for\ all\ \boldsymbol{w}^h \in V, \\ a(\boldsymbol{w}^h, \boldsymbol{u}^h) = (\boldsymbol{w}^h, \boldsymbol{h})_{\Gamma} \end{cases}$$

In the above weak form, the force term is ignored as it is much smaller than the stress handled in reservoir engineering. And the displacement on Γ_q is 0, i.e. $\boldsymbol{q} = 0\ on\ \Gamma_q$. So, the terms $a(\boldsymbol{w}^h, \boldsymbol{q}^h)$ and $(\boldsymbol{w}^h, \boldsymbol{\iota})$ are removed.

The explicit representations of v_i^h, in terms of the shape functions and nodal values are

$$v_i^h = \sum_{A\in\eta-\eta_{qi}} N_A d_{iA} \tag{25}$$

Where η denotes the set of global node numbers. η_{qi} is the set of nodes at which $u_i^h = q_i$ and $\eta - \eta_{qi}$ is the complement of η_{qi}. For each node in $\eta - \eta_{qi}$, the nodal value of u_i^h is to be determined. A is a point. $\boldsymbol{u}$ is a function of $\boldsymbol{x}$.

The vector version is

$$\boldsymbol{v}^h = v_i^h \boldsymbol{e}_i \tag{26}$$

In the same way, we get

$$\boldsymbol{w}^h = w_i^h \boldsymbol{e}_i \quad w_i^h = \sum_{A\in\eta-\eta_{qi}} N_A c_{iA} \tag{27}$$

Now the Galerkin form

$$a(\boldsymbol{w}^h, \boldsymbol{u}^h) = (\boldsymbol{w}^h, \boldsymbol{h})_\Gamma \tag{28}$$

can be written as:

$$a\left(\sum_{A\in\eta-\eta_{qi}} N_A c_{iA}\, \boldsymbol{e}_i, \sum_{B\in\eta-\eta_{qi}} N_B d_{jB}\, \boldsymbol{e}_j\right) = \left(\sum_{A\in\eta-\eta_{qi}} N_A c_{iA}\, \boldsymbol{e}_i, \boldsymbol{h}\right)_\Gamma \tag{29}$$

Take the sum over node A out of the integration, we get

$$\sum_{A\in\eta-\eta_{qi}} c_{iA}\, a\left(N_A \boldsymbol{e}_i, \sum_{B\in\eta-\eta_{qi}} N_B\, \boldsymbol{e}_j\right) d_{jB} = \sum_{A\in\eta-\eta_{qi}} c_{iA}\, (N_A \boldsymbol{e}_i, \boldsymbol{h})_\Gamma \tag{30}$$

Put the integrations together, we get

$$\sum_{A\in\eta-\eta_{qi}} c_{iA}\, a\left[\left(N_A \boldsymbol{e}_i, \sum_{B\in\eta-\eta_{qi}} N_B\, \boldsymbol{e}_j\right) d_{jB} - (N_A \boldsymbol{e}_i, \boldsymbol{h})_\Gamma\right] = 0 \tag{31}$$

As this equation is valid for all nodes B, we must have

$$a\left(N_A \boldsymbol{e}_i, \sum_{B\in\eta-\eta_{qi}} N_B\, \boldsymbol{e}_j\right) d_{jB} - (N_A \boldsymbol{e}_i, \boldsymbol{h})_\Gamma = 0 \tag{32}$$

Rearrange the above equation and move known items to the right side, we have

$$\sum_{j=1}^{n_{dof}} \left(\sum_{B \in \eta - \eta_{qi}} a\left(N_A \boldsymbol{e}_i, N_B \boldsymbol{e}_j \right) d_{jB} \right) = (N_A \boldsymbol{e}_i, \boldsymbol{h})_\Gamma \quad (32)$$

Where $A \in \eta - \eta_{qi}, 1 \le i \le n_{sd}$. $\boldsymbol{e}_i$ is the unit vector with 1 in slot i and zeros elsewhere.

The shape function in the above equations take the form

$$N_a(\boldsymbol{\xi}) = N_a(\xi, \eta, \zeta) = \frac{1}{8}(1 + \xi_a \xi)(1 + \eta_a \eta)(1 + \zeta_a \zeta) \quad (33)$$

4.1.3 The sequential coupling method

To couple the geomechanics to GURU, the compositional simulator, a modified fixed-stress coupling method is used (Kim et al., 2012). For the reservoir simulation, the geomechanics is coupled to it with Equation (34), which is used to calculate porosity. For the geomechanics simulation, fluid flow is coupled to it with Equation (44).

The equations used in this method to update reservoir porosity is

$$\Phi^{n+1} - \Phi^n = \left[\frac{b - \Phi}{K_s} + \frac{b^2}{K_{dr}} \right] \sum S_J \left(p_J^{n+1} - p_J^n \right) + 3\alpha_T b (T^{n+1} - T^n) - \Delta\Phi_C \quad (34)$$

where, S_J is the saturation of phase J.

To get this equation, recall that we have derived the coupling formula for porosity variation as

$$\phi - \phi^0 = \frac{b - \phi}{K_s}(p_f - p_f^0) + (b - \phi)\varepsilon_v \quad (A.15)$$

This Equation is derived in appendix A. And the porosity ϕ is the true porosity not the simulation porosity in reservoir simulations. For simulation porosity Φ, we have

$$\Phi - \Phi^0 = (1 + \varepsilon_v)\phi - \phi^0 = \phi - \phi^0 + \varepsilon_v \phi = \frac{b - \phi}{K_s}(p_f - p_f^0) + b\varepsilon_v \quad (35)$$

or

$$\delta\Phi = \frac{b-\phi}{K_s}\delta p + b\delta\varepsilon_v \tag{36}$$

Using the explicit method, we have

$$\delta\Phi^{n+1} = \frac{b-\Phi^n}{K_s}\delta p^{n+1} + b\delta\varepsilon_V^n + \frac{b^2}{K_{dr}}\delta p^{n+1} - \frac{b^2}{K_{dr}}\delta p^n \tag{37}$$

To calculate the right-hand side, for the first term, we use the implicit method, then we have

$$\frac{b-\Phi^n}{K_s}\delta p^{n+1} = \frac{b-\Phi^n}{K_s}(p^{n+1} - p^n) \tag{38}$$

for the second term, we use the explicit method, then we have

$$b\delta\varepsilon_V^n = b(\varepsilon_V^n - \varepsilon_V^{n-1}) \tag{39}$$

for the third term, using the implicit method, we have

$$\frac{b^2}{K_{dr}}\delta p = \frac{b^2}{K_{dr}}(p^{n+1} - p^n) \tag{40}$$

and for the last term, using the explicit method, we have

$$-\frac{b^2}{K_{dr}}\delta p = -\frac{b^2}{K_{dr}}(p^n - p^{n-1}) \tag{41}$$

Putting them together, we get

$$\Phi^{n+1} - \Phi^n = \left(\frac{b-\Phi}{K_s} + \frac{b^2}{K_{dr}}\right)(p^{n+1} - p^n) + \left[b(\varepsilon_V^n - \varepsilon_V^{n-1}) - \frac{b^2}{K_{dr}}(p^n - p^{n-1})\right] \tag{42}$$

and we define the group in the square brackets as $-\Delta\Phi_C$, that is

$$-\Delta\Phi_C = b(\varepsilon_V^n - \varepsilon_V^{n-1}) - \frac{b^2}{K_{dr}}(p^n - p^{n-1}) \tag{43}$$

For the geomechanics simulation, the fluid flow is coupled to it with the Biot (1941,1955) theory. The total stress could be written as

$$\sigma = \sigma_{eff} - bp \tag{44}$$

Where σ is the total stress, σ_{eff} is the effective stress, and p is the fluid pressure, b is the Biot coefficient. Now the total stress change could be written as

$$\boldsymbol{\sigma} - \boldsymbol{\sigma}_0 = \boldsymbol{C}_{dr} : \boldsymbol{\varepsilon} - b(p - p_0)\boldsymbol{I} \tag{45}$$

Where $\boldsymbol{\sigma}_0$ is the initial value, $\boldsymbol{C}_{dr} : \varepsilon$ is the stress change induced by displacement, p_0 is the initial fluid pressure. $\boldsymbol{I}$ is a vector that takes the following form for 3D problems.

$$\boldsymbol{I} = \begin{bmatrix} 1 \\ 1 \\ 1 \\ 0 \\ 0 \\ 0 \end{bmatrix} \tag{46}$$

Rewriting the above equation, we have

$$\boldsymbol{\sigma} = \boldsymbol{\sigma}_0 + \boldsymbol{C}_{dr} : \boldsymbol{\varepsilon} - b(p - p_0)\boldsymbol{I} \tag{47}$$

When building the matrix for geomechanics, just replace $\boldsymbol{\sigma}$ with $\boldsymbol{\sigma}_0 + \boldsymbol{C}_{dr} : \boldsymbol{\varepsilon} - b(p - p_0)\boldsymbol{I}$ in section 4.1.1.

With this coupling method, the algorithm is plotted in **Fig. 66**.

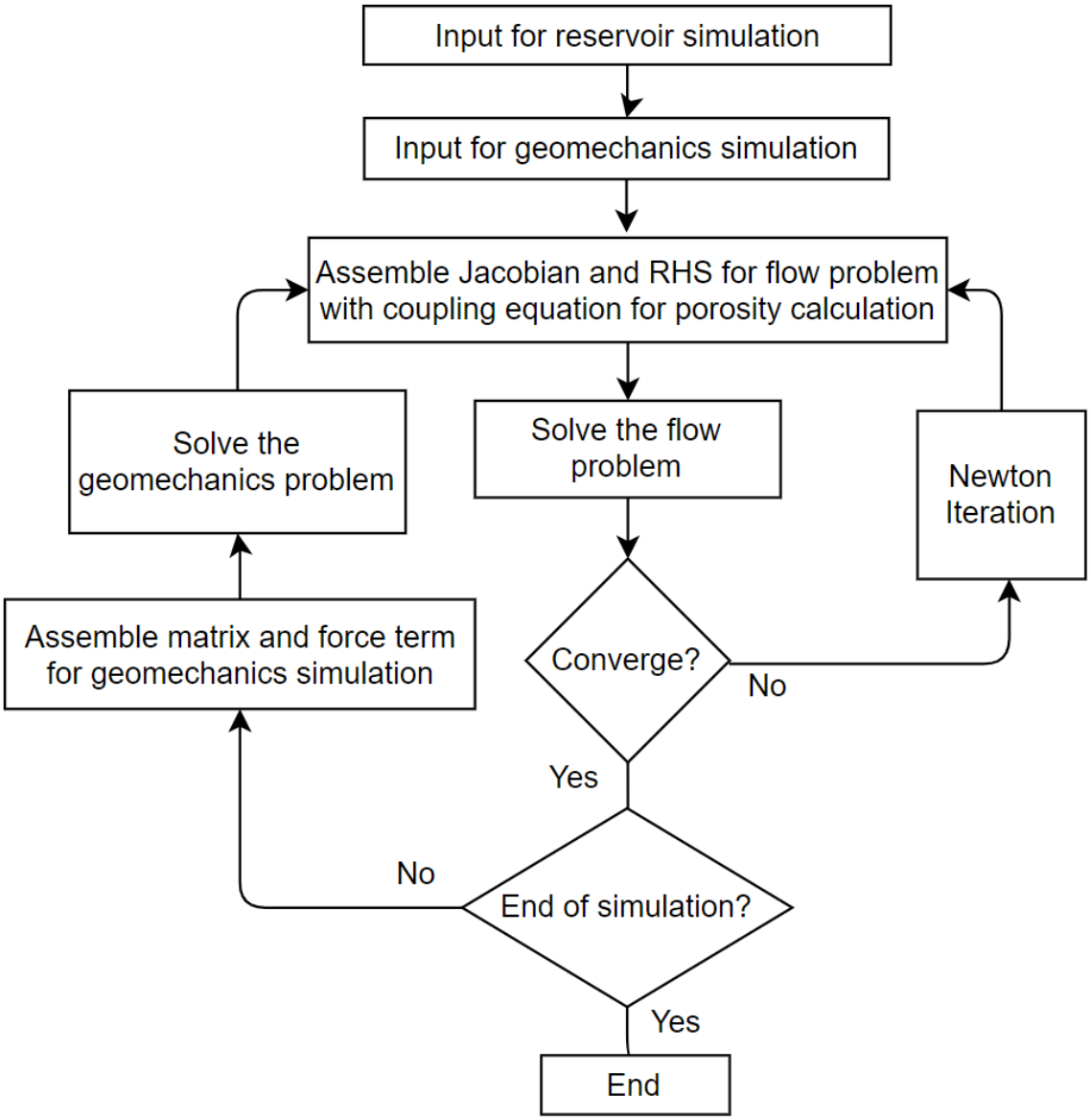

Figure 66 Algorithm for coupled flow and geomechanics simulation

4.1.4 Strain calculation from displacement

In Equation (34), we need the volumetric strain ε_v to update porosity. It is defined as

$$\varepsilon_v = \varepsilon_{xx} + \varepsilon_{yy} + \varepsilon_{zz} \tag{48}$$

It can be calculated once we get the displacements from the geomechanics simulation. By definition, for a 2D problem,

$$\varepsilon(\boldsymbol{u}) = \{\varepsilon_I(\boldsymbol{u})\} = \begin{Bmatrix} u_{1,1} \\ u_{2,2} \\ u_{1,2} + u_{2,1} \end{Bmatrix}$$

thus,

$$\varepsilon(\boldsymbol{u}) = \begin{Bmatrix} u_{1,1} \\ u_{2,2} \\ u_{1,2} + u_{2,1} \end{Bmatrix} = \begin{bmatrix} \frac{\partial u_x}{\partial x} \\ \frac{\partial u_z}{\partial z} \\ \frac{\partial u_x}{\partial z} + \frac{\partial u_z}{\partial x} \end{bmatrix} = \sum_{a=1}^{nnode} \underbrace{\begin{bmatrix} N_{,x}^a & 0 \\ 0 & N_{,z}^a \\ N_{,z}^a & N_{,x}^a \end{bmatrix}}_{B_e^a} \begin{bmatrix} u_x^a \\ u_z^a \end{bmatrix} \quad (48)$$

For 3D problem,

$$\varepsilon(\boldsymbol{u}) = \begin{Bmatrix} u_{1,1} \\ u_{2,2} \\ u_{3,3} \\ u_{2,3} + u_{3,2} \\ u_{1,3} + u_{3,1} \\ u_{1,2} + u_{2,1} \end{Bmatrix} = \sum_{a=1}^{nnode} \underbrace{\begin{bmatrix} N_{A,1} & 0 & 0 \\ 0 & N_{A,2} & 0 \\ 0 & 0 & N_{A,3} \\ 0 & N_{A,3} & N_{A,2} \\ N_{A,3} & 0 & N_{A,1} \\ N_{A,2} & N_{A,1} & 0 \end{bmatrix}}_{B_e^a} \begin{bmatrix} u_x^a \\ u_y^a \\ u_z^a \end{bmatrix} \quad (49)$$

4.1.5 Initial stress term

Usually the initial stress term $\boldsymbol{\sigma}_0$ in Equation (47) is ignored as people only care about how stress change and the porosity change induced by it. However, in the fracture closure simulation, it is important to get the total stress, so the initial stress must be included in the stress calculation.

After coupled with fluid flow, the governing equation without initial conditions is

$$\int_\Omega \varepsilon(\boldsymbol{w}) : \boldsymbol{\sigma} d\Omega = \int_\Omega \varepsilon(\boldsymbol{w}) : (\boldsymbol{C}\varepsilon(\boldsymbol{u}) - p\mathbf{1}) d\Omega \quad (50)$$

Including the initial conditions, it becomes

$$\int_\Omega \varepsilon(\boldsymbol{w}) : \boldsymbol{\sigma} d\Omega = \int_\Omega \varepsilon(\boldsymbol{w}) : (\boldsymbol{C}\varepsilon(\boldsymbol{u}) + \boldsymbol{\sigma_0} - bp\mathbf{1} + bp_0\mathbf{1}) d\Omega \quad (51)$$

For an element Ω^e (a cell in reservoir simulatin),

$$\int_{\Omega^e} \varepsilon(\boldsymbol{w}) : (\boldsymbol{C}\varepsilon(\boldsymbol{u}) + \boldsymbol{\sigma_0} - bp\mathbf{1} + bp_0\mathbf{1}) d\Omega^e$$

$$= \int_{\Omega^e} B_e^{A^T} D B_e \boldsymbol{u}^e - B_e^{A^T}\mathbf{1}p_e + B_e^{A^T}\mathbf{1}p_0 + B_e^{A^T}\boldsymbol{\sigma_0} d\Omega^e \quad (52)$$

$$= \int_{\Omega^e} B_e^{A^T} D B_e d\Omega^e \boldsymbol{u}^e - \int_{\Omega^e} B_e^{A^T}\mathbf{1} d\Omega^e \, p_e + \int_{\Omega^e} B_e^{A^T}\mathbf{1} d\Omega^e \, p_0 + \int_{\Omega^e} B_e^{A^T}\boldsymbol{\sigma_0} d\Omega^e$$

where the $\mathbf{1}$ is a vector, and for 3D problems, $\mathbf{1} = \begin{bmatrix} 1 \\ 1 \\ 1 \\ 0 \\ 0 \\ 0 \end{bmatrix}$. p_e is the fluid pressure in this element. $B_e^{A^T}$ is the coefficient matrix for the element. The initial stress vector is $\boldsymbol{\sigma_0} = \begin{bmatrix} \sigma_{xx}^0 \\ \sigma_{yy}^0 \\ \sigma_{zz}^0 \\ 0 \\ 0 \\ 0 \end{bmatrix}$. The order of stress component is consistent with definitions of $\boldsymbol{\varepsilon}(u)$ and $\boldsymbol{\sigma}$ as

$$\varepsilon(u) = \begin{Bmatrix} u_{1,1} \\ u_{2,2} \\ u_{3,3} \\ u_{2,3} + u_{3,2} \\ u_{1,3} + u_{3,1} \\ u_{1,2} + u_{2,1} \end{Bmatrix}$$

$$\sigma = \begin{Bmatrix} \sigma_{11} \\ \sigma_{22} \\ \sigma_{33} \\ \sigma_{23} \\ \sigma_{13} \\ \sigma_{12} \end{Bmatrix}$$

4.1.6 Model validation

The coupled flow and geomechanics simulator developed above is validated with the following two problems which have analytical solutions.

The Terzaghi Problem

This is a 1D problem. The parameters are listed in **Table 8**. At the top, a force of 20MPa is applied. The boundary condition at the bottom is no displacement for geomechanics and no flow for flow simulation (**Fig. 67**). To verify our simulator, I compared the pressure of the grid at the bottom with the available analytical solution. As **Fig. 68** shows, a good match is achieved.

Table 8 Parameters of the Terzaghi problem

Parameter	Value	Parameter	Value
E, GPa	1	Porosity	0.25
ν	0.0	Compressibility, Pa^{-1}	4×10^{-10}
b	1.0	Permeability, mD	50
P_i, MPa	10	Viscosity, $Pa \cdot s$	1×10^{-3}

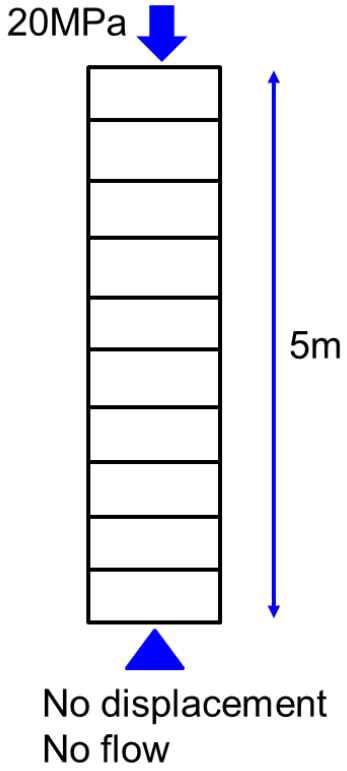

Figure 67 Sketch of the Terzaghi problem

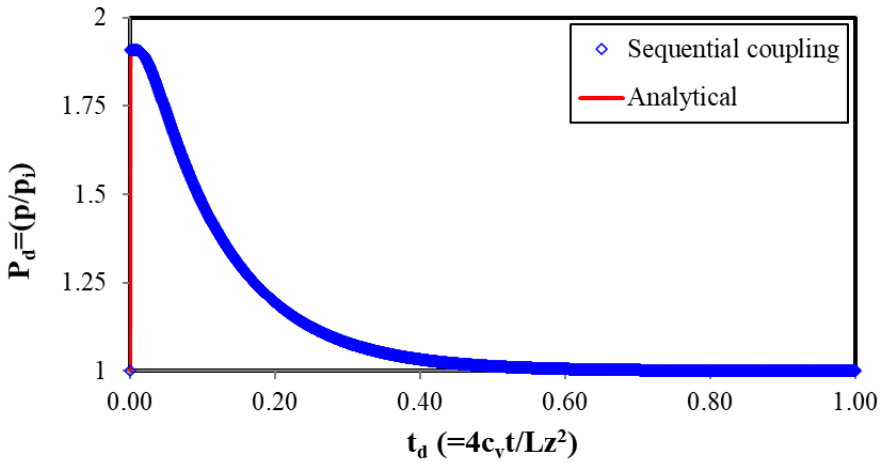

Figure 68 Comparison of sequential coupling results and analytical solution of dimensionless pressure at bottom grid

The Mandel Problem

The Mandel problem (Abousleiman et al. 1996) is a 2D problem. Nonuniform force is applied at the top. On other boundaries, no displacement boundary conditions are applied (**Fig. 69**). The parameters are listed in **Table 9**. We monitored the pressure in the target grid and compared it to the analytical solution (**Fig. 70**).

Table 9 Parameters of the Mandel problem

Parameter	Value	Parameter	Value
E, MPa	450	Porosity	0.25
ν	0.0	Compressibility, Pa^{-1}	4×10^{-10}
b	1.0	Permeability, mD	50
P_i, MPa	10	Viscosity, $Pa \cdot s$	1×10^{-3}

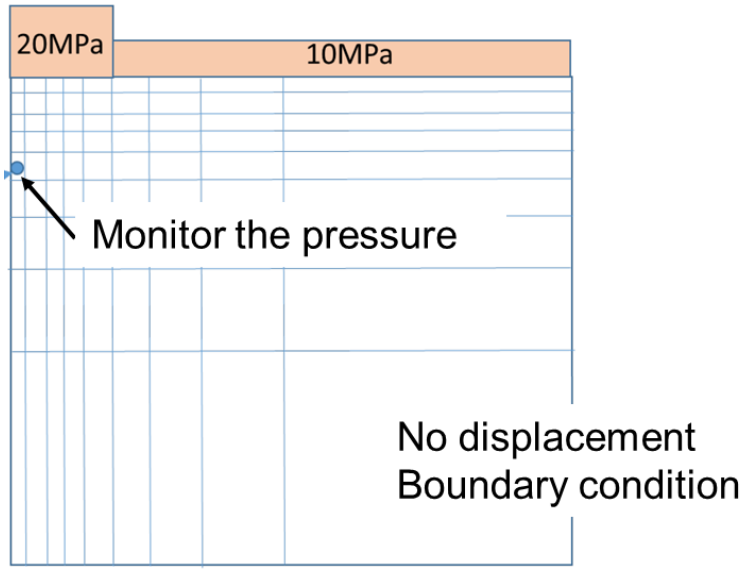

Figure 69 Sketch of the Mandel problem

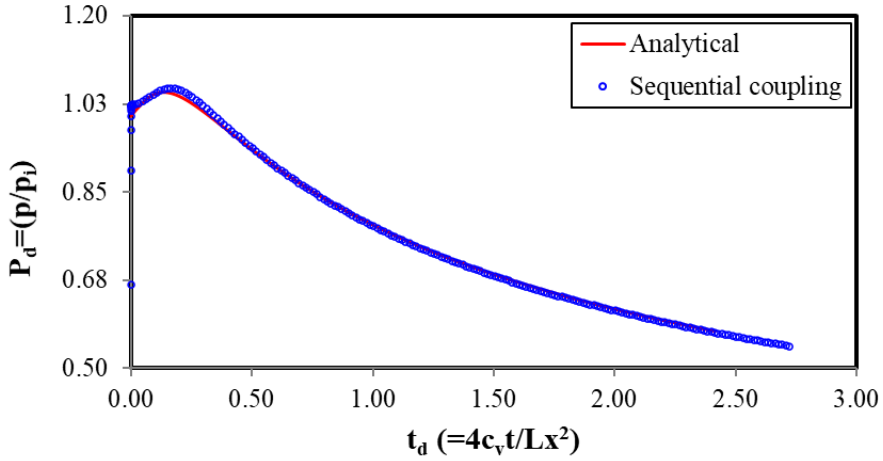

Figure 70 Comparison of sequential coupling results and analytical solution of dimensionless pressure at the target cell

4.2 Fracture closure simulation

In this part, a new method to calculate fracture closure and fracture permeability is proposed. Then this method is applied to a gas reservoir to check how the fracture close will affect production rate and cumulative production.

4.2.1 Calculation of fracture closure and fracture permeability

To update the fracture conductivity in response to fracture closure, the following empirical formula is used.

$$\frac{\Delta V_j}{\sigma_n} = a - b\Delta V_j \tag{53}$$

Where ΔV_j is the fracture volume change induced by the fracture closure, and σ_n is the normal contact stress acting on the fracture surface that tries to close the fracture. As $V = w \cdot area$, if we assume the area does not change, then Equation (53) could be expressed in terms of fracture width w and normal contact stress σ_n as

$$\frac{(w_{offset} - w)}{\sigma_n} = a - b(w_{offset} - w)$$

or

$$\sigma_n = \frac{(w_{offset} - w)}{a - b(w_{offset} - w)} \quad (54)$$

Where w_{offset} is the width at which the asperities inside the closing fracture come in contact and w is the current width of the closing fracture. The coefficients a and b are functions of the initial normal stiffness (K_{ni}) and w_{offset} as:

$$a = \frac{1}{K_{ni}}, b = \frac{1}{K_{ni} w_{offset}} \quad (55)$$

Where K_{ni} is related to rock properties such as the joint roughness coefficient, joint compressive strength, and joint aperture.

Rearrange Equation (55), the current fracture width could be calculated as

$$\mathrm{w} = \frac{w_{offset} + \sigma_n (b w_{offset} - a)}{1 + b\sigma_n} \quad (56)$$

Equation 55 describes the relationship between the normal contact stress acting on a closing fracture surface and the amount of closure. It was derived by Bandis et al., 1983 from experiment results. This relationship is non-linear. To show this non-linearity, a typical curve between the normal contact stress (σ_n) and the fracture width (w) calculated from Equation (55) is shown in **Fig. 71**.

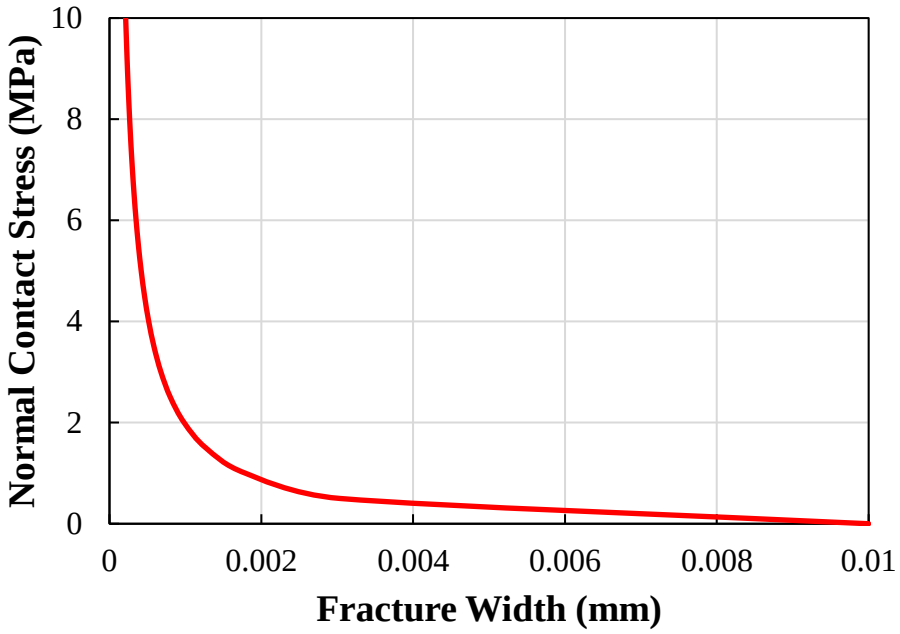

Figure 71 Non-linear relationship between normal contact stress (σ_n) and the fracture width (w) calculated from Bandis et al., 1983, with K_{ni}=21.8MPa/mm, w_{offset} =0.01mm

The normal contact stress that acts on the fracture surface is defined as the difference between the normal compressive stress in the local region acting on the fracture surface and the fluid pressure in the fracture.

$$\sigma_n = S_n - P_f \tag{57}$$

Where S_n is the normal compressive stress in the local region that tries to close the fracture and P_f is the fluid pressure in the closing fracture.

Once we get the new fracture width, we could update the fracture conductivity from the Cubic Law as

$$C_f(x) = k_f(x)w_f(x) = \lambda w_f^3(x) \tag{58}$$

Where C_f is the fracture conductivity and w_f the fracture width.

In this simulator, the hydraulic fractures are modeled with EDFM (Chai, et al. 2016, Yu et al. 2017), once the geomechanics simulation is finished. Stress in the reservoir is calculated and the fracture permeability could be updated with Equations (57), (56), and (58). In the geomechanics simulation, the fracture grid is not included. The geomechanics simulation is on the matrix. When calculating the fracture width, the stress in the matrix cell in which the fracture cell is embedded is used as the compressive stress.

4.2.2 Reservoir and Fracture Parameters

To investigate how the fracture closes during production and its effect on production rate and cumulative production, the following reservoir model is used. This a gas reservoir. Production is controlled by bottom hole pressure. Production time is 500 days. At the end of the simulation, the production rate and cumulative production are plotted as well as fracture closure parameters at different locations along hydraulic fractures. One production well along the x-axis is located at the center of the reservoir (**Fig. 72**). 3 hydraulic fractures are connected to this well. The parameters are listed in **Table 10**.

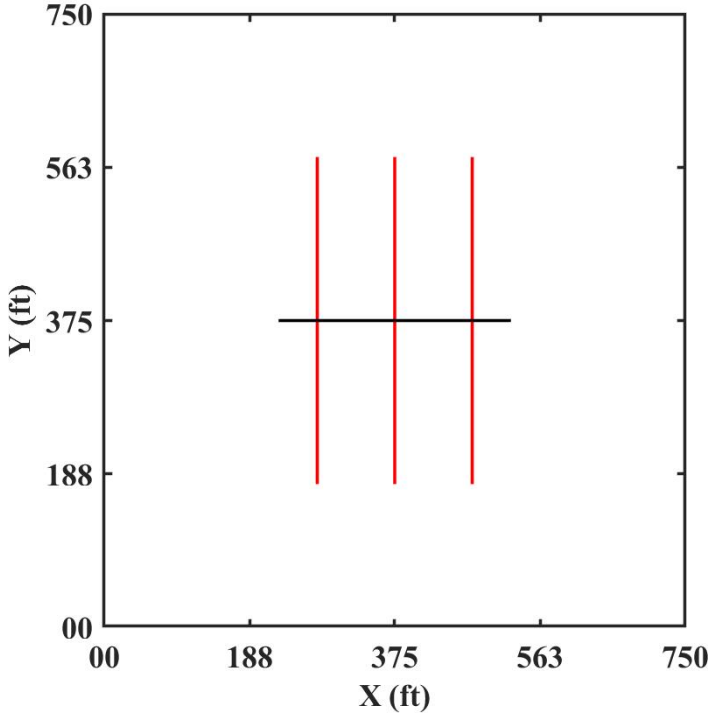

Figure 72 The reservoir dimensions (one well with 3 fractures)

Table 10 Reservoir and Fracture Parameters

Parameter	Value
Reservoir dimension, ft	750× 750 ×60
Number of Grids	15× 15 ×3
Fracture Permeability, mD	100
Biot coefficient	0.7
Poisson's ratio	0.2
Young's Modulus, psi	2.9×10^{6}
Matrix permeability, mD	1×10^{-4}
Porosity	0.03

Table 10 Continued

Parameter	Value
Kni, Mpa/mm	21.8
Woffset, mm	0.8
σ_{xx}, Mpa	52
σ_{yy}, Mpa	55
σ_{zz}, Mpa	60
Matrix permeability, mD	0.0001
Sw in fracture	0.8
Sw in matrix	0.1

4.2.3 Simulation Results

Stress and fracture width change during production

To quantitatively describe how the stress and fracture width change during production, we select 2 points along the fracture, one is at the fracture center, the other one is at the fracture tip. The compressive stress, contact stress as well as pressure in the hydraulic fractures there are plotted as follows (**Figs. 73** and **74**).

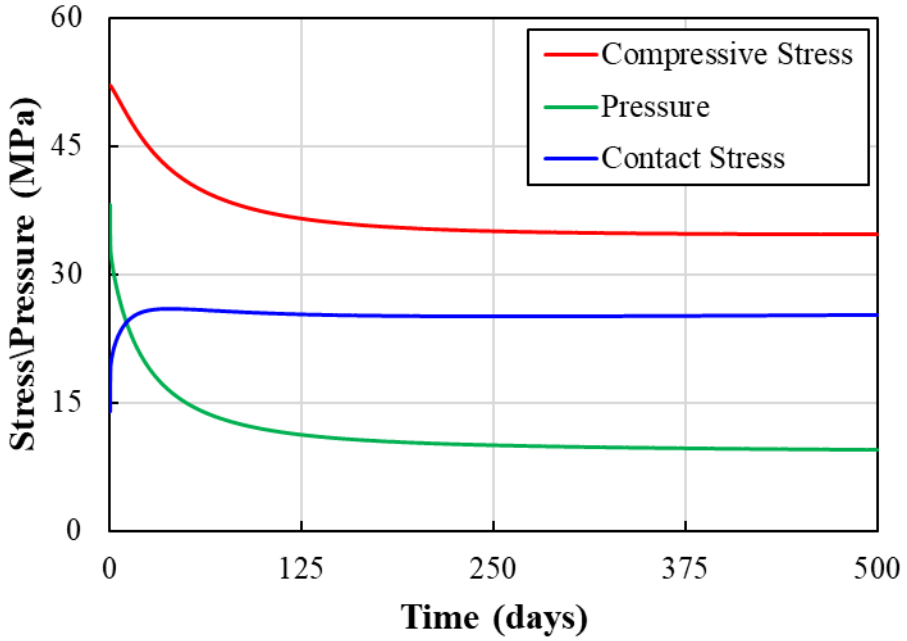

Figure 73 Stress and pressure change at fracture tips (case 1)

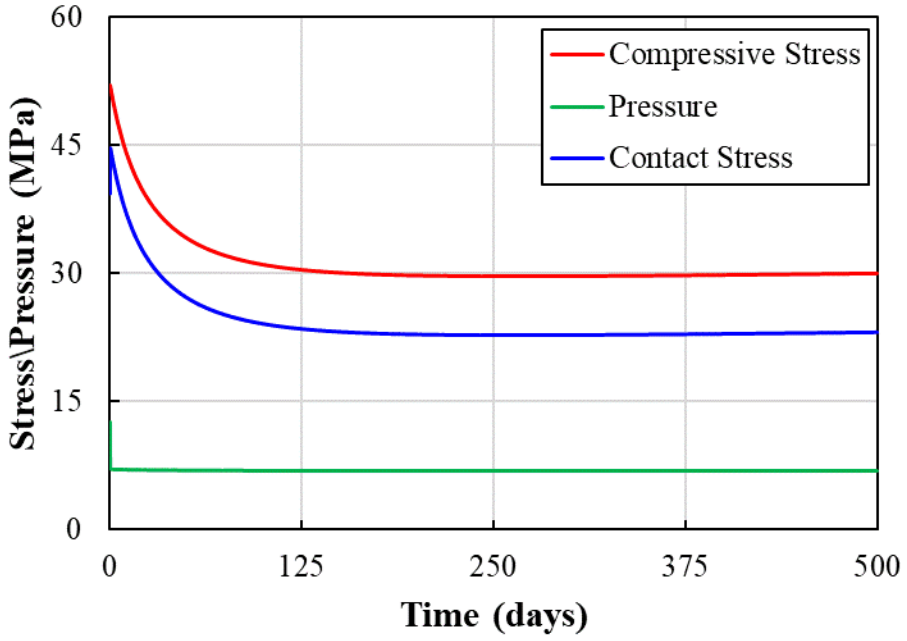

Figure 74 Stress and pressure change at fracture center (case 1)

As can be found from the plots, at the fracture center, the pressure in the hydraulic fracture cell drops to the bottomhole pressure immediately after production. The compressive stress acting on the fracture surface has not changed a lot, as a result, we observe a sharp increase in the value of contact stress. And the fracture width and fracture permeability there drop to 0.22mm and 13mD respectively. With gas being produced from the nearby region, compressive stress begins to drop. As pressure does not change with time, contact stress drops with compressive stress, and both fracture width and fracture permeability are partially restored. But the restored values are less than half of the initial values. After the production of 125 days, both stress and fracture width become stable and do not change much (**Fig. 76**).

At the fracture tips, we find different stress and fracture change trends. As this location is 200ft away from the wellbore, it takes time for the pressure drop to reach this point. The decline curves for compressive stress and pressure are smoother. After production of about 10 days, though both compressive stress and pressure still decline, the decline rate is small, and the contact stress becomes stable. As a response to stress and pressure change, fracture width and fracture permeability drop severely in the first 10 days, then fracture width and permeability are restored a little bit. After 10 days, there is little change observed in fracture width and permeability (**Fig. 75**).

If we compare the fracture permeability at fracture tips and the center, at the end of production the fracture permeability at the fracture center is higher than that at fracture tips, as compressive stress drop at fracture center is higher.

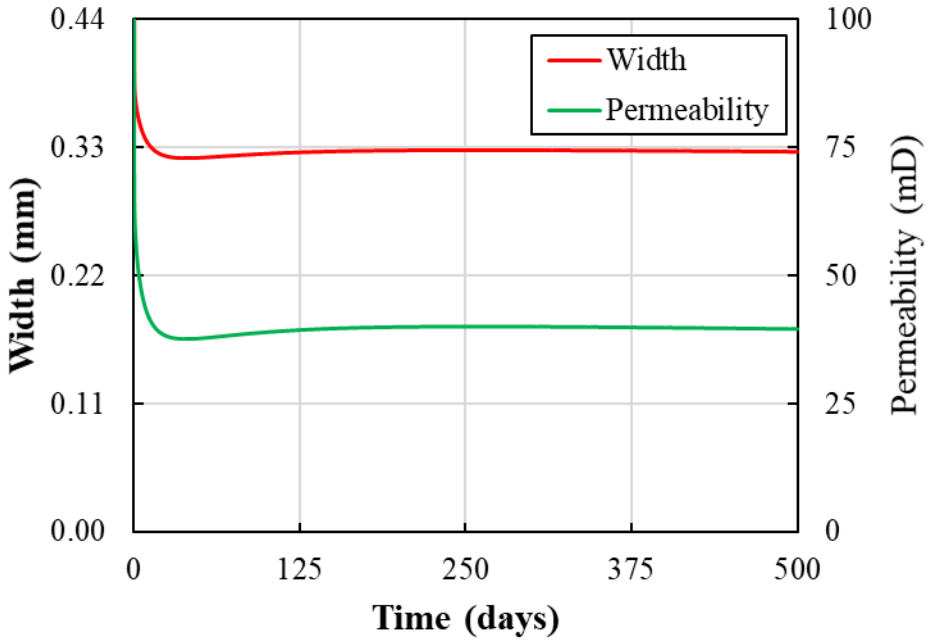

Figure 75 Fracture width and permeability change at fracture tips (case 1)

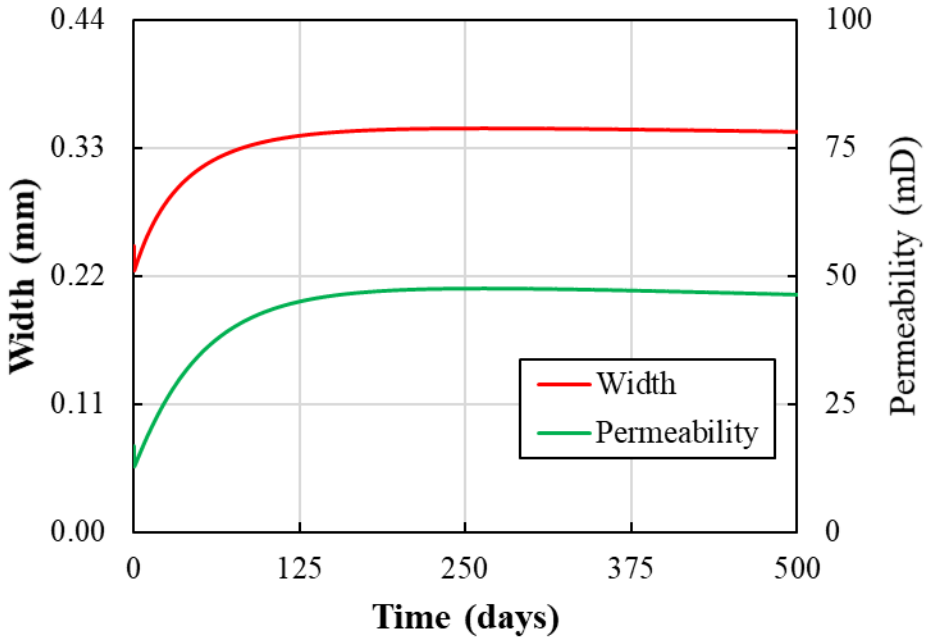

Figure 76 Fracture width and permeability change with time at the fracture center (case 1)

Effects of Fracture Closure on Production Performance

The gas production rate and total gas production are plotted in **Fig. 77**. To make it clear how the fracture closure affects production performance, these results are compared to a new case 2 that does not consider the fracture closure in **Figs. 78-79**. This comparison shows that fracture closure only affects production at the early production stage. When fracture closure is considered, the initial gas production rate is around 100 MSCF/day, which is about half the rate of case 2. This result is consistent with the stress and fracture width change. After the production of 10 days, the production rate affected by fracture closure catches up with that not considering the fracture closure. Then there is almost no difference between these two cases in production rate.

The difference in total gas production of these two cases is mainly caused by the early production period.

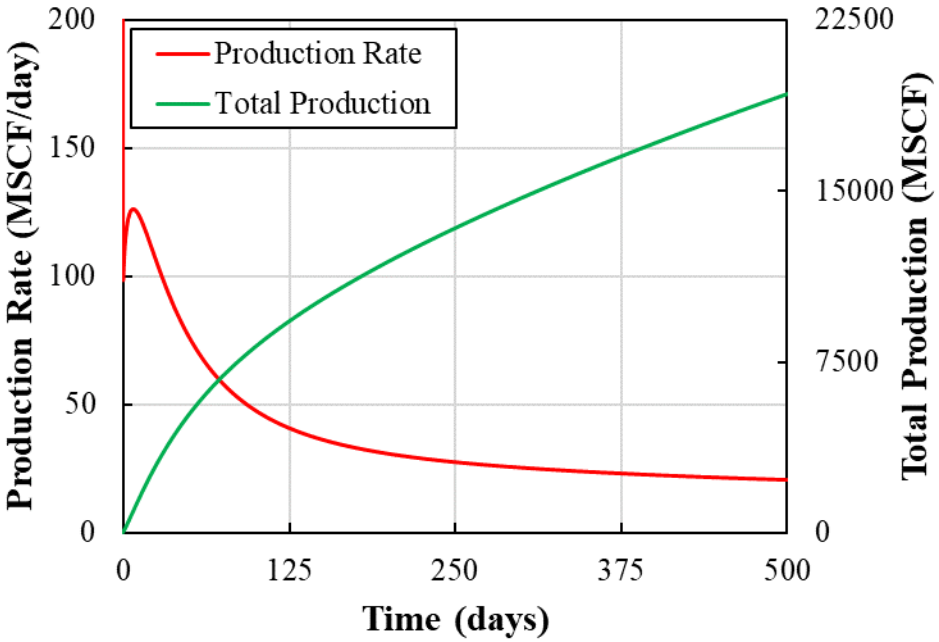

Figure 77 Gas production rate and total gas production considering fracture closure (case 1)

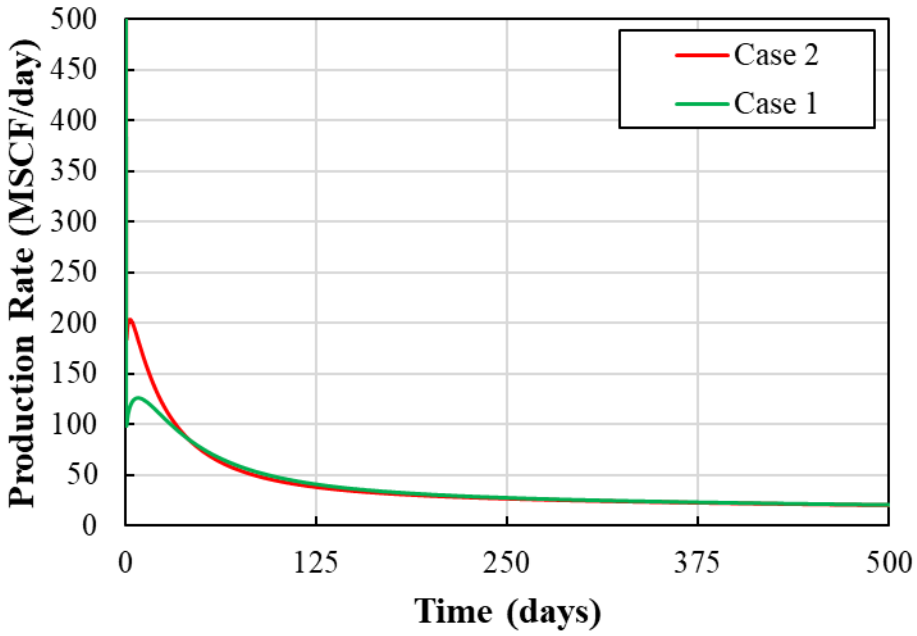

Figure 78 Comparison of gas production rate (case 1 vs case 2)

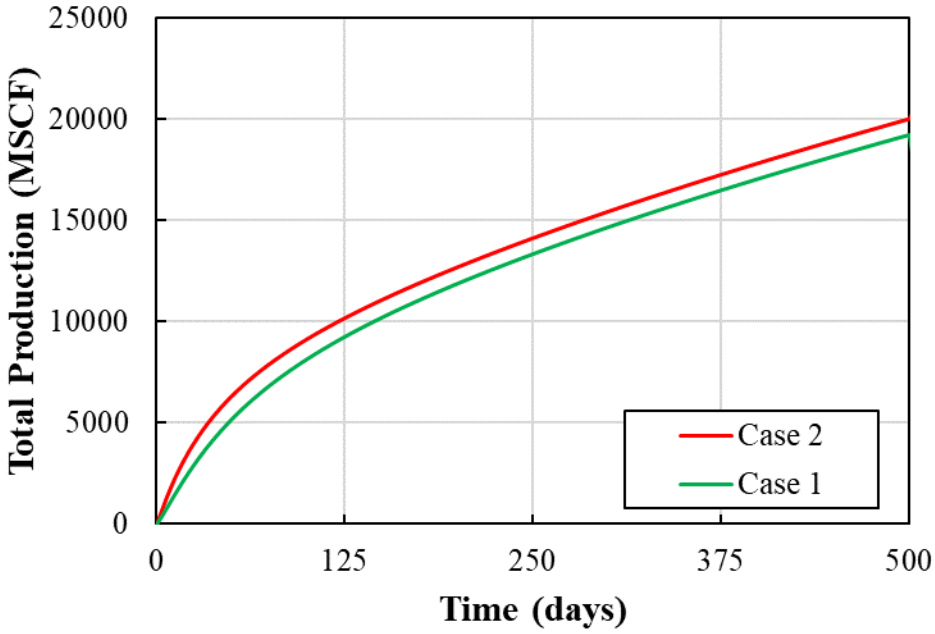

Figure 79 Comparison of total gas production (case 1 vs case 2)

Advantage over using rock compaction tables

In commercial software, the commonly used method to consider fracture closure is to use rock compaction tables or empirical formulas. These methods assume that the compressive stress acting on the fracture surface does not change with time. The minimum horizontal stress is usually used as this compressive stress. Then the normal contact stress could be simplified as $\sigma_n = \sigma_{min} - P_f$.

From the above analysis, this compressive stress acting on the fracture surface changes significantly during production, especially at the beginning of production. To show how this assumption of constant compressive stress will affect the reservoir simulation results, case 3 is run. For this case, when we calculate the normal stress, instead of using the changing compressive stress calculated from geomechanics

simulation, the minimum horizontal stress σ_{min} is used. The rest calculations are the same as case 1.

At the center of hydraulic fractures, once production starts, the pressure in hydraulic fracture cells drops to bottom hole pressure. As the compressive stress is constant, the calculated effective stress does not change with time (**Figs. 80** and **81**).

At the tips of hydraulic fractures, hydraulic fracture width and permeability are determined by fluid pressure in hydraulic fracture cells only. For case 3, the fracture permeability keeps declining during the production, while in case 1 fracture permeability becomes stable after production of 10 days (**Figs. 82** and **83**).

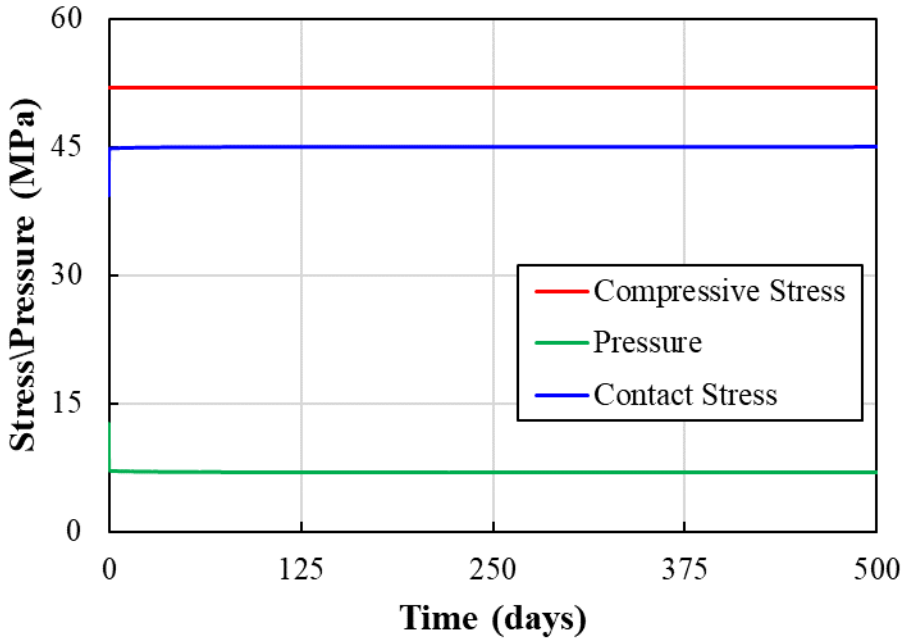

Figure 80 Stress and pressure change at the center of fracture (case 3)

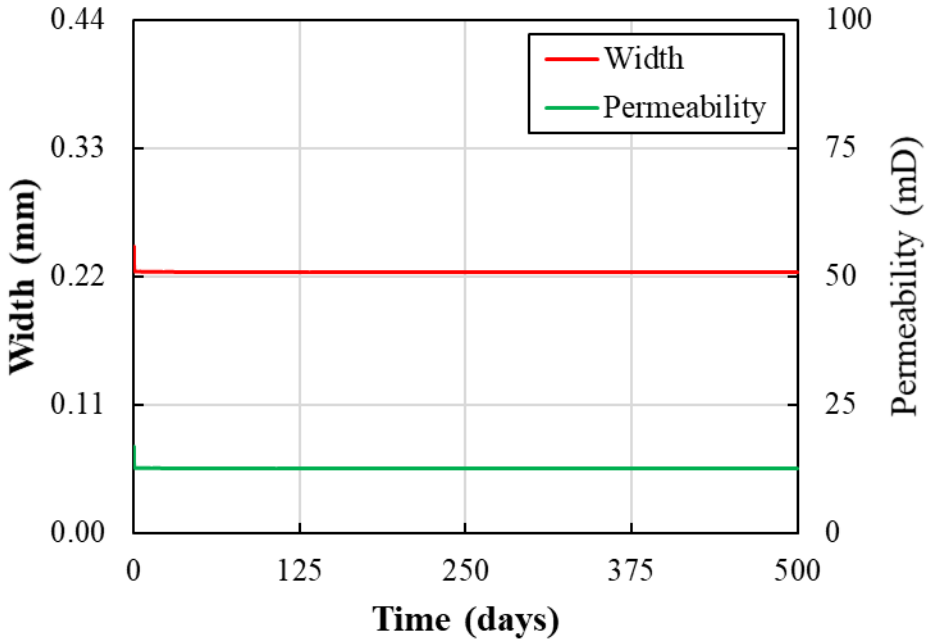

Figure 81 Fracture width and permeability change at the center of the fracture (case 3)

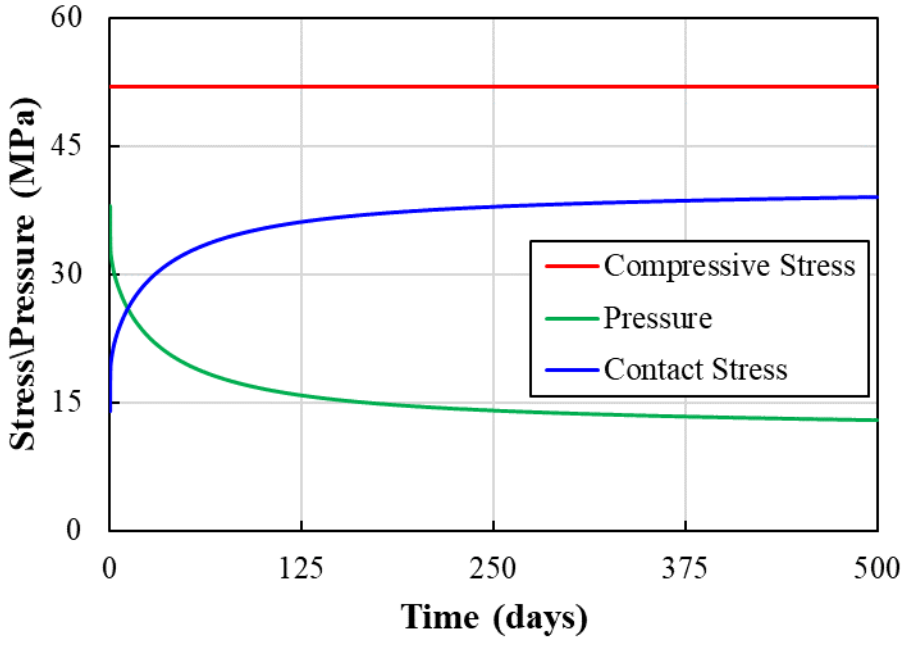

Figure 82 Stress and pressure change at fracture tips (case 3)

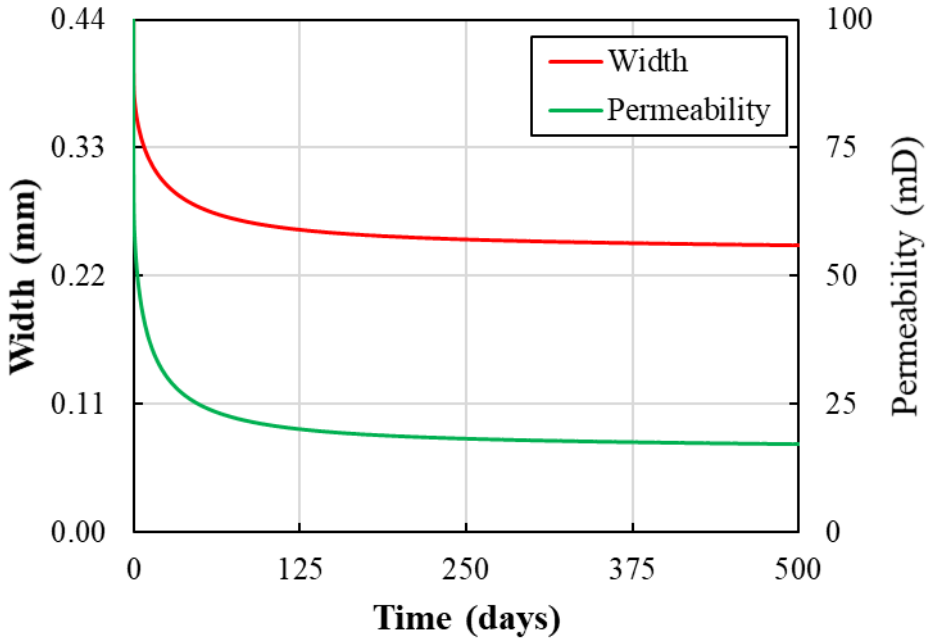

Figure 83 Fracture width and permeability change at fracture tips (case 3)

Fig. 84 and **85** compare the production performance of cases 1 and 3. In case 1, the compressive stress declines with time, and the effect of fracture closure mainly focuses on the early production stage. In case 3, the assumption of constant compressive stress makes the fractures more compressed and as a result, reduces the production at the early production stage.

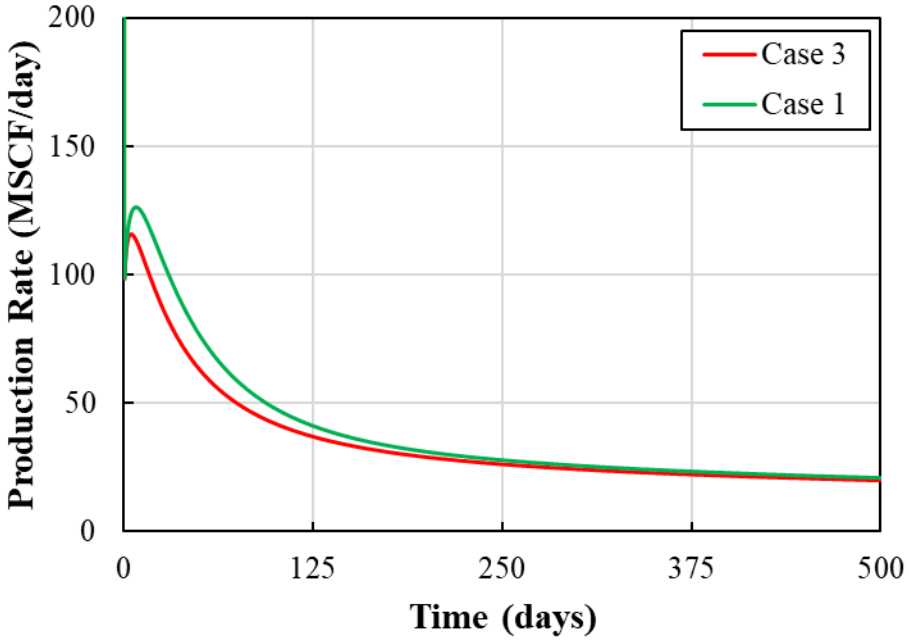

Figure 84 Comparison of gas production rate between case 1 and 3

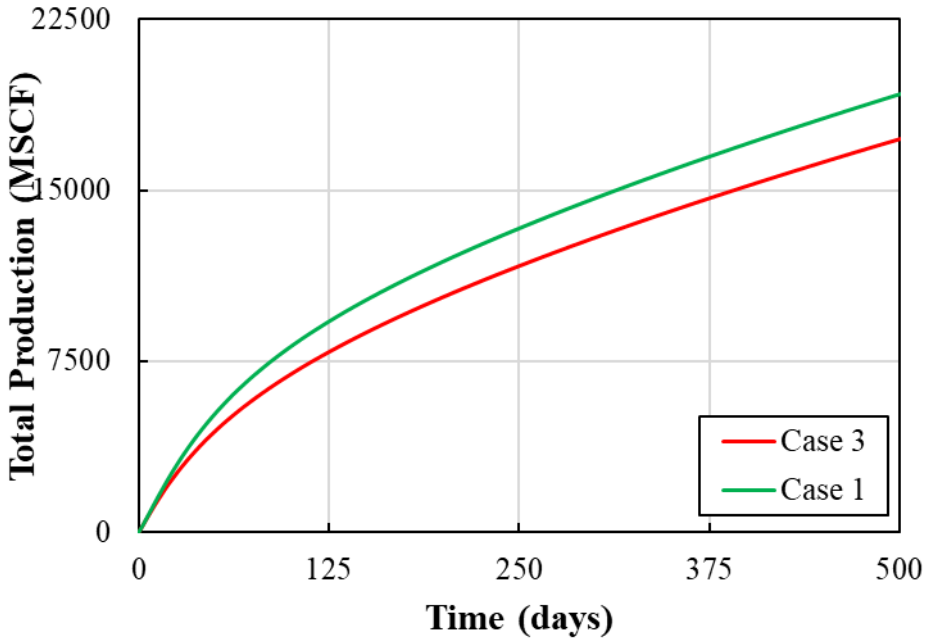

Figure 85 Comparison of total gas production between case 1 and 3

Fracture closure of tilted fractures

Due to the complex stress distribution underground and the interaction between fractures in a fracturing operation, the geometry of hydraulic fractures is complicated. In case 1, the angle between fracture and wellbore is 90°, which is called the strike angle. To investigate the effect of strike angle on fracture closure, case 4 is designed. In this case, the strike angle is 45° (**Fig. 86**).

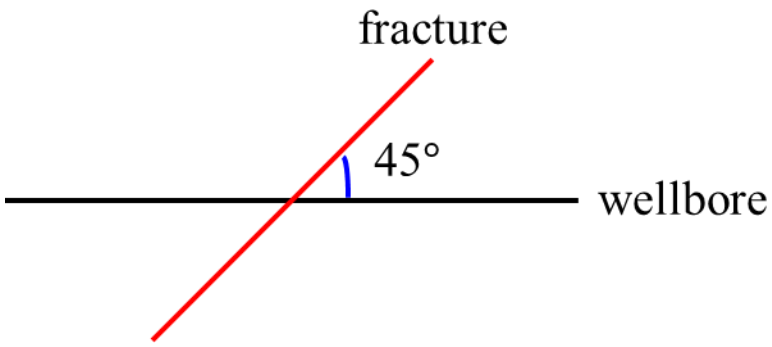

Figure 86 tilted fracture with strike angle = 45°

From geomechanics simulation, we get the stress in the matrix cell in which the fracture cell is embedded. Then the compressive stress on the tilted fracture surface could be easily calculated with the following formula.

$$\sigma_n = \frac{1}{2}(\sigma_x + \sigma_y) + \frac{1}{2}(\sigma_x - \sigma_y)cos2\theta + \tau_{xy}sin2\theta \quad (59)$$

$$\tau_n = -\frac{1}{2}(\sigma_x - \sigma_y)sin2\theta + \tau_{xy}cos2\theta \quad (60)$$

Where σ_n is the compressive stress and the rest stress components are illustrated in **Fig. 87**.

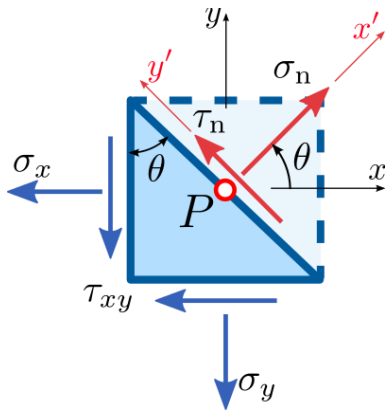

Figure 87 Stress components at a plane passing through a point in a continuum under plane stress conditions

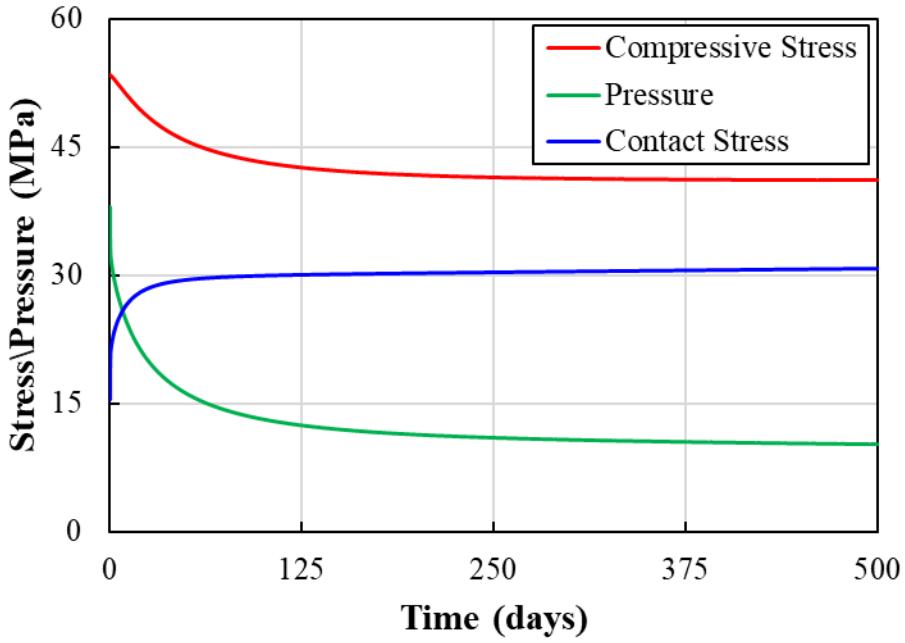

Figure 88 Pressure and stress at fracture tips in case 4

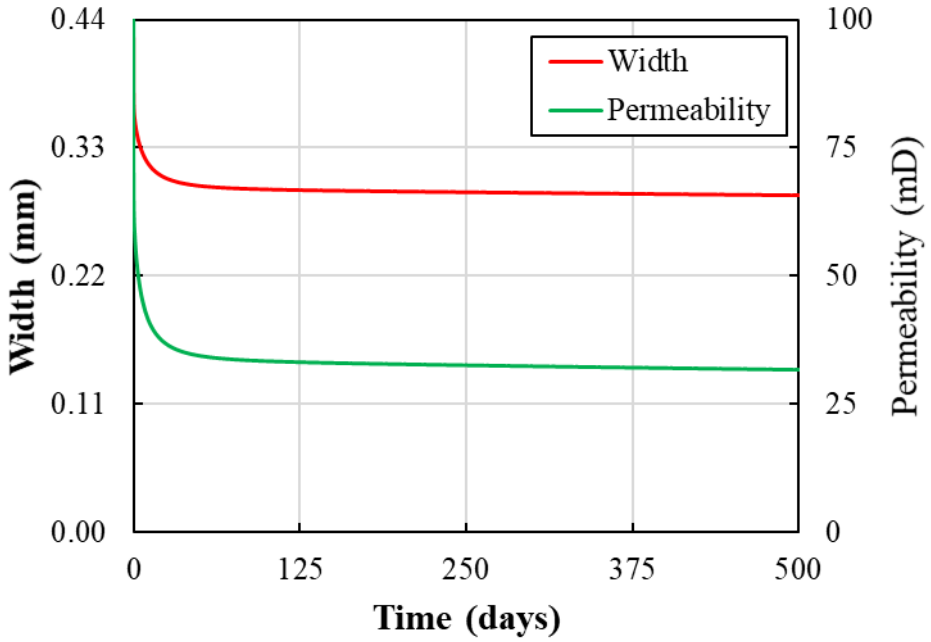

Figure 89 Fracture width and permeability change with time at fracture tips (case 4)

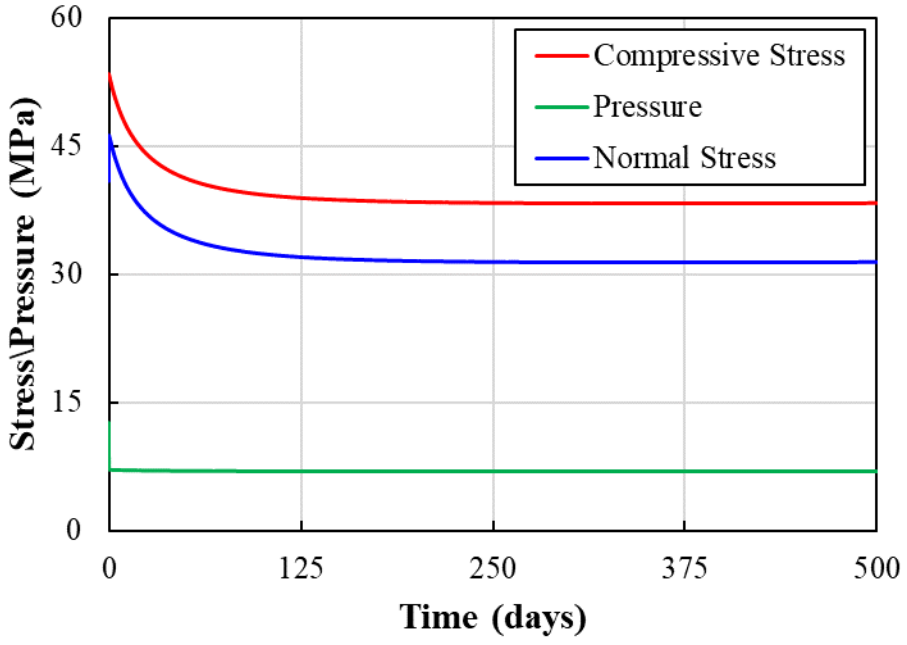

Figure 90 Stress and pressure at fracture center (case 4)

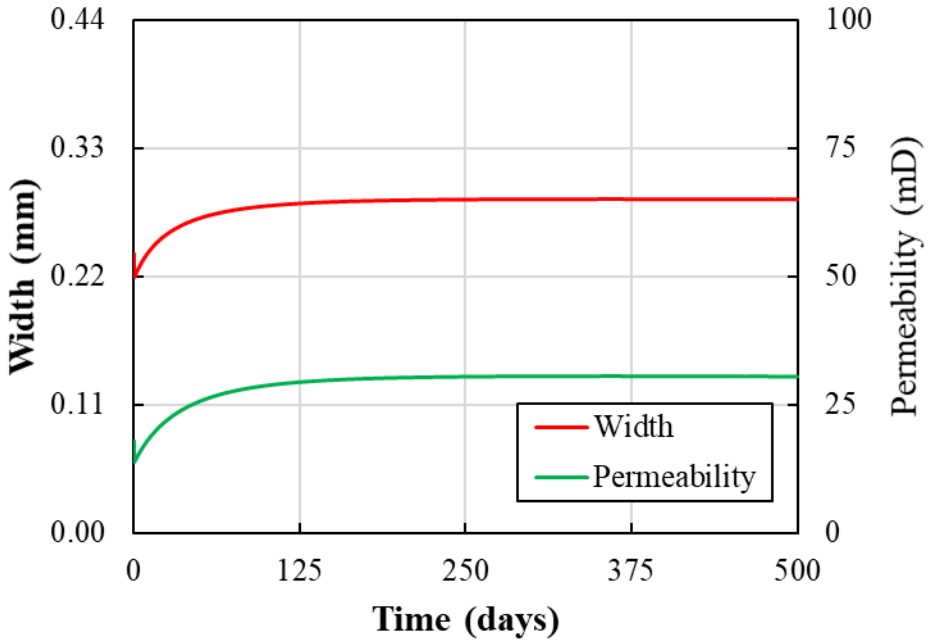

Figure 91 fracture width and permeability change at fracture center (case 4)

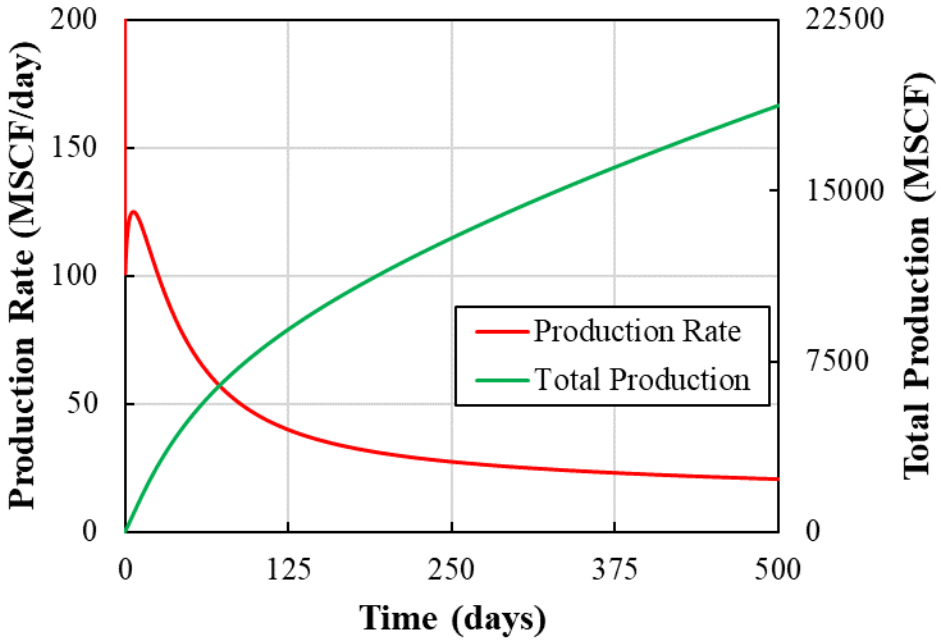

Figure 92 Production curves of case 4

From the plots **Figs. 88-92**, it can be found that strike angle mainly affects the specific values of compressive stress and normal contact stress, the trend is the same as case 1. The effect of fracture closure focuses on the early production stage and fracture permeability changes at fracture tips and center follows the same trend as case 1.

4.3 Summary

The simulation results show that

1. Fracture closure mainly occurs at the early production stage. Both fracture width and permeability experience a sharp decline due to the pressure drop in hydraulic fractures at the start of production. With production going on, reduced fracture width and permeability are partially restored due to the decreased compressive stress.

2. Fracture closure mainly reduces the production rate at the early production stage. After about 100 days, there is almost no difference in production performance compared to cases not considering fracture closure.

3. At different locations along the fracture, fracture closure shows different trends. At the end of production, at the center of fractures, the restored fracture permeability is higher than that at fracture tips.

4. Using rock compaction tables generates a low production rate and cumulative production as it ignores the compressive stress change during production and as a result, the fracture is over-compressed.

CHAPTER V

CONCLUSIONS

5.1 Conclusions

This study focuses on understanding how the stress change in unconventional reservoirs during production and injection. In chapter 1, stress calculation is done based on a real field case. It is verified that parent well production induced stress change; the altered stress field affects negatively the fracture geometry of infill wells and results in the poor production performance of parent and infill wells. From this chapter, we also learned:

1. Due to non-uniform fracture growth in the parent well, some extreme long fractures are created which induce the irregular depletion area and large stress change region in the reservoir.

2. Due to non-uniform fracture growth, even 1000 ft large well spacing, frac hits still can be induced from the irregular depletion area between the staggered parent and infill wells.

3. Parent well depletion not only changes reservoir stress in the layer of the parent well but also alters stress in the lower layer of the infill wells. Stress change favors fracture height in infill wells of layer 4 growing to layer 3 (the depleted region).

In chapter 2, the efficiency of subsequent parent well water injection is investigated. Different injection designs are simulated to analyze the effects of variable injection factors. From this analysis, we learned:

4. After soaking for 1 week, in all cases, a decline of about 1200 psi in pressure and 400 psi in S_{hmin} are observed.

5. For similar injection volumes, higher injection pressure with shorter injection time can create better pressure and stress recovery than low injection pressure with long injection time.

6. Double injection volume and injection time cannot dramatically improve pressure and stress recovery.

7. Subsequent water injection is more efficient in oil-water two-phase case: better restoration through water injection (i.e. about 400 psi higher in pressure and S_{hmin}) and less decline in soaking period

In chapter 4, a coupled geomechanics and fluid flow simulator is developed. A new method to calculate fracture closure is proposed and implemented. Cases simulations show that

8. Fracture closure mainly occurs at the early production stage. Both fracture width and permeability experience a sharp decline due to the pressure drop in hydraulic fractures at the start of production. With production going on, reduced fracture width and permeability are partially restored due to the decreased compressive stress.

9. Fracture closure mainly reduces the production rate at the early production stage. After about 100 days, there is almost no difference in production performance compared to cases not considering fracture closure.

10. At different locations along the fracture, fracture closure shows different trends. At the end of production, at the center of fractures, the restored fracture permeability is higher than that at fracture tips.

11. Using rock compaction tables generates a low production rate and cumulative production as it ignores the compressive stress change during production and as a result, the fracture is over-compressed.

REFERENCES

Awada, A., Santo, M., Lougheed, D., Xu, D., & Virues, C. (2016, October 1). Is That Interference? A Work Flow for Identifying and Analyzing Communication Through Hydraulic Fractures in a Multiwell Pad. Society of Petroleum Engineers. doi:10.2118/178509-PA

Bhardwaj, P., Hwang, J., Manchanda, R., & Sharma, M. M. (2016, September 26). Injection Induced Fracture Propagation and Stress Reorientation in Waterflooded Reservoirs. Society of Petroleum Engineers. doi:10.2118/181883-MS

Cao, R., Li, R., Girardi, A., Chowdhury, N., & Chen, C. (2017, July 24). Well Interference and Optimum Well Spacing for Wolfcamp Development at Permian Basin. Unconventional Resources Technology Conference. doi:10.15530/URTEC-2017-2691962

Dean R.H., Gai S., Stone C.M., and Minkoff S.E. 2006. A comparison of techniques for coupling porous flow and geomechanics. SPE J 11(1): 132–140.

Garipov, T. T., Karimi-Fard, M., & Tchelepi, H. A. (2014, August 18). Fully Coupled flow and Geomechanics Model for Fractured Porous Media. American Rock Mechanics Association.

Guo, X., Wu, K., & Killough, J. (2017, July 24). Investigation of Production-Induced Stress Changes for Infill Well Stimulation in Eagle Ford Shale. Unconventional Resources Technology Conference. doi:10.15530/URTEC-2017-2670745

Guo, X., Wu, K., Killough, J., & Tang, J. (2018, August 9). Understanding the Mechanism of Interwell Fracturing Interference Based on Reservoir-Geomechanics-Fracturing Modeling in Eagle Ford Shale. Unconventional Resources Technology Conference.

Gupta, J., Zielonka, M., Albert, R. A., El-Rabaa, A. M., Burnham, H. A., & Choi, N. H. (2012, January 1). Integrated Methodology for Optimizing Development of Unconventional Gas Resources. Society of Petroleum Engineers. doi:10.2118/152224-MS

Kamkom, R., Zhu, D., & Bond, A. J. (2007, January 1). Predict Undulating Well Performance. Society of Petroleum Engineers. doi:10.2118/109761-MS

Kim, J., Tchelepi, H. A., & Juanes, R. (2011, June 1). Stability, Accuracy, and Efficiency of Sequential Methods for Coupled Flow and Geomechanics. Society of Petroleum Engineers. doi:10.2118/119084-PA

King, G. E., Rainbolt, M. F., & Swanson, C. (2017, October 9). Frac Hit Induced Production Losses: Evaluating Root Causes, Damage Location, Possible Prevention Methods and Success of Remedial Treatments. Society of Petroleum Engineers. doi:10.2118/187192-MS

King, G. E., & Valencia, R. L. (2016, February 1). Well Integrity for Fracturing and Re-Fracturing: What Is Needed and Why? Society of Petroleum Engineers. doi:10.2118/179120-MS

Lindsay, G., Miller, G., Xu, T., Shan, D., & Baihly, J. (2018, January 23). Production Performance of Infill Horizontal Wells vs. Pre-Existing Wells in the Major US Unconventional Basins. Society of Petroleum Engineers. doi:10.2118/189875-MS

Olson, J. E., & Wu, K. (2012, January 1). Sequential vs. Simultaneous Multizone Fracturing in Horizontal Wells: Insights From a Non-Planar, Multifrac Numerical Model. Society of Petroleum Engineers. doi:10.2118/152602-MS

Pankaj, P., Shukla, P., Kavousi, P., & Carr, T. (2018, September 17). Integrated Well Interference Modeling Reveals Optimized Well Completion and Spacing in the Marcellus Shale. Society of Petroleum Engineers. doi:10.2118/191393-MS

Rainbolt, M. F., & Esco, J. (2018, January 23). Paper Title: Frac Hit Induced Production Losses: Evaluating Root Causes, Damage Location, Possible Prevention Methods and Success of Remediation Treatments, Part II. Society of Petroleum Engineers. doi:10.2118/189853-MS

Raterman, Kevin T., Farrell, Helen E., Mora, Oscar S., Janssen, Aaron L., Gomez, Gustavo A., Busetti, Seth , McEwen, Jamie , Friehauf, Kyle , Rutherford, James , Reid, Ray , Jin, Ge , Roy, Baishali , and Mark Warren. "Sampling a Stimulated Rock Volume: An Eagle Ford Example." SPE Res Eval & Eng 21 (2018): 927–941. doi: https://doi.org/10.2118/191375-PA

Safari, R., Lewis, R., Ma, X., Mutlu, U., & Ghassemi, A. (2017, April 1). Infill-Well Fracturing Optimization in Tightly Spaced Horizontal Wells. Society of Petroleum Engineers. doi:10.2118/178513-PA

Sangnimnuan, A., Li, J., & Wu, K. (2018, June 1). Development of Efficiently Coupled Fluid-Flow/Geomechanics Model To Predict Stress Evolution in Unconventional Reservoirs With Complex-Fracture Geometry. Society of Petroleum Engineers. doi:10.2118/189452-PA

Settari A. and Walters D.A. 2001. Advances in coupled geomechanical and reservoir modeling with applications to reservoir compaction. SPE J 6(3): 334–342.

Sun, H., Zhou, D., Chawathe, A., & Liang, B. (2017, July 24). Understanding the 'Frac-Hits' Impact on a Midland Basin Tight-Oil Well Production. Unconventional Resources Technology Conference. doi:10.15530/URTEC-2017-2662893

Van Dam, D.B., C.J. de Pater, and R. Romijn. 2000. Analysis of hydraulic fracture closure in laboratory experiments. SPE Prod. Facil. 15 (3): 151-158.

Warpinski, N.R., P.T. Branagan, B.P. Engler, R. Wilmer, and S.L. Wolhart. 2002. Evaluation of a downhole tiltmeter array for monitoring hydraulic fractures. Int. J. Rock Mech. & Min. Sci. 34.

Wu, K., & Olson, J. E. (2015, April 1). Simultaneous Multifracture Treatments: Fully Coupled Fluid Flow and Fracture Mechanics for Horizontal Wells. Society of Petroleum Engineers. doi:10.2118/167626-PA

Wu, K., Olson, J. E., & Balhoff, M. T. (2015, November 13). Study of Multiple Fracture Interaction Based on An Efficient Three-Dimensional Displacement Discontinuity Method. American Rock Mechanics Association.

Wu, R., Kresse, O., Weng, X., Cohen, C.-E., & Gu, H. (2012, January 1). Modeling of Interaction of Hydraulic Fractures in Complex Fracture Networks. Society of Petroleum Engineers. doi:10.2118/152052-MS

Xu, T., Lindsay, G., Baihly, J., Ejofodomi, E., Malpani, R., & Shan, D. (2017, October 9). Proposed Refracturing Methodology in the Haynesville Shale. Society of Petroleum Engineers. doi:10.2118/187236-MS

Yang, D., Moridis, G. J., & Blasingame, T. A. (2013, August 12). Numerical Upscaling of Coupled Flow and Geomechanics in Highly Heterogeneous Porous Media. Unconventional Resources Technology Conference.

Yu, W., Xu, Y., Weijermars, R., Wu, K., & Sepehrnoori, K. (2017, January 24). Impact of Well Interference on Shale Oil Production Performance: A Numerical Model for Analyzing Pressure Response of Fracture Hits with Complex Geometries. Society of Petroleum Engineers. doi:10.2118/184825-MS

Yu, W., Wu, K., Liu, M., Sepehrnoori, K., & Miao, J. (2018, September 17). Production Forecasting for Shale Gas Reservoirs with Nanopores and Complex Fracture Geometries Using An Innovative Non-Intrusive EDFM Method. Society of Petroleum Engineers. doi:10.2118/191666-MS

Zhu, J., Forrest, J., Xiong, H., & Kianinejad, A. (2017, September 13). Cluster Spacing and Well Spacing Optimization Using Multi-Well Simulation for the Lower Spraberry Shale in Midland Basin. Society of Petroleum Engineers. doi:10.2118/187485-MS.

APPENDIX A

DERIVATION OF THE COUPLING EQUATIONS

Any arbitrary change in pore volume is given by

$$\delta V_p = \frac{\partial V_p}{\partial P_f}\Big|_{\sigma_v} \delta p_f + \frac{\partial V_p}{\partial \sigma_v}\Big|_{p_f} \delta \sigma_v \tag{A.1}$$

Where V_p is the pore volume, p_f is the fluid pressure, σ_v is volumatirc stress.

And the change in bulk volume is given by

$$\delta V_b = \frac{\partial V_b}{\partial P_f}\Big|_{\sigma_v} \delta p_f + \frac{\partial V_b}{\partial \sigma_v}\Big|_{p_f} \delta \sigma_v \tag{A.2}$$

Dividing Equation (A.1) by V_p and Equation (A.2) byV_b, we get

$$\frac{\delta V_p}{V_p} = \left(\frac{1}{V_p}\frac{\partial V_p}{\partial P_f}\Big|_{\sigma_v} - \frac{1}{V_p}\frac{\partial V_p}{\partial \sigma_v}\Big|_{p_f}\right)\delta p_f + \frac{1}{V_p}\frac{\partial V_p}{\partial \sigma_v}\Big|_{p_f} (\delta \sigma_v + \delta p_f) \tag{A.3}$$

$$\frac{\delta V_b}{V_b} = \left(\frac{1}{V_b}\frac{\partial V_b}{\partial P_f}\Big|_{\sigma_v} - \frac{1}{V_b}\frac{\partial V_b}{\partial \sigma_v}\Big|_{p_f}\right)\delta p_f + \frac{1}{V_b}\frac{\partial V_b}{\partial \sigma_v}\Big|_{p_f} \left(\delta \sigma_v + \delta p_f\right) \tag{A.4}$$

Assume that the matrix is homogeneous, its only result is a uniform dilation throughout the whole matrix. And define intrinsic solid grain modulus as

$$\frac{\delta V_p}{V_p} = \frac{\delta V_b}{V_b} = -\frac{1}{K_s}\delta p_f = \frac{1}{K_s}\sigma_v \tag{A.5}$$

define solid skeleton modulus as

$$\frac{1}{V_b}\frac{\partial V_b}{\partial \sigma_v}\Big|_{p_f} = \frac{1}{K_{dr}} \tag{A.6}$$

Applying the above two definitions to Equation (A.4), we get

$$\frac{\delta V_b}{V_b} = \delta \varepsilon_v = -\frac{1}{K_s}\delta p_f + \frac{1}{K_{dr}}(\delta \sigma_v + \delta p_f) \tag{A.7}$$

Comparing Equations (A.4) and (A.7), we get

$$\frac{1}{V_b}\frac{\partial V_b}{\partial P_f}\bigg|_{\sigma_v} - \frac{1}{V_b}\frac{\partial V_b}{\partial \sigma_v}\bigg|_{p_f} = -\frac{1}{K_s} \tag{A.8a}$$

$$\frac{1}{V_b}\frac{\partial V_b}{\partial P_f}\bigg|_{\sigma_v} - \frac{1}{K_{dr}} = -\frac{1}{K_s} \tag{A.8a}$$

$$\frac{1}{V_b}\frac{\partial V_b}{\partial P_f}\bigg|_{\sigma_v} = \frac{1}{K_{dr}} - \frac{1}{K_s} \tag{A.8a}$$

By Betti reciprocal theorem, we have

$$\delta\sigma_v \frac{\partial V_b}{\partial P_f}\bigg|_{\sigma_v} \delta p_f = \delta p_f \frac{\partial V_p}{\partial \sigma_v}\bigg|_{p_f} \delta\sigma_v \tag{A.8b}$$

Or

$$\frac{\partial V_b}{\partial P_f}\bigg|_{\sigma_v} = \frac{\partial V_p}{\partial \sigma_v}\bigg|_{p_f} \tag{A.8b}$$

From Equation (A.8a), we get

$$\frac{1}{V_b}\frac{\partial V_b}{\partial P_f}\bigg|_{\sigma_v} = \frac{1}{K_{dr}} - \frac{1}{K_s} = \frac{\phi}{V_p}\frac{\partial V_b}{\partial P_f}\bigg|_{\sigma_v} \tag{A.8c}$$

Combining Equation (A.8b) with (A.8c), we get

$$\frac{1}{V_p}\frac{\partial V_p}{\partial \sigma_v}\bigg|_{p_f} = \frac{1}{\phi}\left(\frac{1}{K_{dr}} - \frac{1}{K_s}\right) \tag{A.9}$$

Using Equations (A.5) and (A.9), Equation (A.3) can be written as

$$\frac{\delta V_p}{V_p} = -\frac{1}{K_s}\delta p_f + \frac{1}{\phi}\left(\frac{1}{K_{dr}} - \frac{1}{K_s}\right)(\delta\sigma_v + \delta p_f) \tag{A.10}$$

Where the porosity ϕ is true porosity, defined as the ratio of the current pore volume to the bulk volume in the deformed configuration, i.e. $\phi = \frac{V_p}{V_b}$.

By the Chain Rule, the porosity variation can be written as

$$\delta\phi = \delta\left(\frac{V_p}{V_b}\right) = \frac{1}{V_b}\delta V_p + V_p\delta\left(\frac{1}{V_b}\right)$$

$$= \frac{1}{V_b}\delta V_p - V_p\frac{1}{V_b^2}\delta V_b$$

$$= \frac{V_p}{V_b}\left(\frac{\delta V_p}{V_p} - \frac{\delta V_b}{V_b}\right) = \phi\left(\frac{\delta V_p}{V_p} - \frac{\delta V_b}{V_b}\right)$$

Using Equation (A.10) to replace $\frac{\delta V_p}{V_p}$, the above equation becomes

$$\delta\phi = \delta\left(\frac{V_p}{V_b}\right) = \phi\left(\frac{\delta V_p}{V_p} - \frac{\delta V_b}{V_b}\right)$$

$$= \phi\left[-\frac{1}{K_s}\delta p_f + \frac{1}{\phi}\left(\frac{1}{K_{dr}} - \frac{1}{K_s}\right)\left(\delta\sigma_v + \delta p_f\right) - \delta\varepsilon_v\right] \quad \text{(A.11)}$$

Recall that Equation (A.7) is

$$\frac{\delta V_b}{V_b} = \delta\varepsilon_v = -\frac{1}{K_s}\delta p_f + \frac{1}{K_{dr}}(\delta\sigma_v + \delta p_f) \quad \text{(A.7)}$$

Rewrite it for $\delta\sigma_v + \delta p_f$, we have

$$\delta\sigma_v + \delta p_f = K_{dr}(\delta\varepsilon_v + \frac{1}{K_s}\delta p_f) \quad \text{(A.12)}$$

Substitute the above expression to Equation (A.11), we have

$$\delta\phi = \phi\left[-\frac{1}{K_s}\delta p_f + \frac{1}{\phi}\left(\frac{1}{K_{dr}} - \frac{1}{K_s}\right)K_{dr}(\delta\varepsilon_v + \frac{1}{K_s}\delta p_f) - \delta\varepsilon_v\right]$$

$$= \phi\left[\frac{1}{\phi}\left(1 - \frac{K_{dr}}{K_s}\right)\frac{1}{K_s}\delta p_f - \frac{1}{K_s}\delta p_f + \frac{1}{\phi}\left(1 - \frac{K_{dr}}{K_s}\right)\delta\varepsilon_v - \delta\varepsilon_v\right] \quad \text{(A.13)}$$

Define $b = 1 - \frac{K_{dr}}{K_s}$, and substitute into the above equation, we have

$$\delta\phi = \phi\left[\frac{1}{\phi}b\frac{1}{K_s}\delta p_f - \frac{1}{K_s}\delta p_f + \frac{1}{\phi}b\delta\varepsilon_v - \delta\varepsilon_v\right]$$

$$= \phi\left[\frac{1}{\phi}\frac{b-\phi}{K_s}\delta p_f + \frac{1}{\phi}(b-\phi)\delta\varepsilon_v\right] \quad \text{(A.14)}$$

$$= \frac{b-\phi}{K_s}\delta p_f + (b-\phi)\delta\varepsilon_v$$

The current true porosity can be expressed as

$$\phi - \phi^0 = \frac{b-\phi}{K_s}(p_f - p_f^0) + (b-\phi)\varepsilon_v \quad \text{(A.15)}$$

The simulation porosity or reservoir porosity (porosity in reservoir simulation) is the ratio of the current pore volume to the bulk volume in the reference (initial) configuration as

$$\Phi = \frac{V_p}{V_b^0} = \frac{V_b}{V_b^0}\frac{V_p}{V_b} = (1+\varepsilon_v)\phi \quad \text{(A.16)}$$

Thus,

$$\Phi - \Phi^0 = (1+\varepsilon_v)\phi - \phi^0 = \phi - \phi^0 + \varepsilon_v\phi = \frac{b-\phi}{K_s}(p_f - p_f^0) + b\varepsilon_v \quad \text{(A.17)}$$

APPENDIX B

ANALYTICAL SOLUTIONS TO THE TERZAGHI (1925) AND MANDEL (1953) PROBLEMS

For the Terzaghi (1925) problem, the analytical solutions for pressure (p) and displacement (u_z) as functions of locations and time are as follows

$$p(z,t) = -W\frac{a_f - a_i}{\alpha a_i}\sum_{j=0}^{\infty}\frac{4(-1)^j}{\pi(2j+1)}\cos\left[\frac{(2j+1)\pi z}{2H}\right]exp\left\{-\left[\frac{(2j+1)\pi}{2}\right]^2\frac{c_f t}{4H^2}\right\} \quad \text{(B.1)}$$

$$u_z(z,t) = -W\left(a_f - a_i\right)H\sum_{j=0}^{\infty}\frac{8(-1)^j}{\pi^2(2j+1)^2}\sin\left[\frac{(2j+1)\pi z}{2H}\right]exp\left\{-\left[\frac{(2j+1)\pi}{2}\right]^2\frac{c_f t}{4H^2}\right\} + Wa_f z \quad \text{(B.2)}$$

where

$$a_f = \frac{(1+\nu)(1-2\nu)}{E(1-\nu)} \quad \text{(B.3)}$$

$$a_i = a_f\left(\frac{b^2 a_f}{\phi c_f}\right)^{-1} \quad \text{(B.4)}$$

W is the external load on top of the column, H is the column height, and z is location of the observation point along the z-direction.

For the Mandal (1953) problem, the analytical solutions for pressure (p) and displacement (u_x and u_y) as functions of positions and time are as follows

$$u_x(x,t) = \left[\frac{W\nu}{2GL} - \frac{W\nu_u}{GL}\sum_{i=1}^{\infty}\frac{\sin\alpha_i cos\alpha_i}{\alpha_i - \sin\alpha_i cos\alpha_i}\exp\left(-\frac{\alpha_i^2 ct}{L^2}\right)\right]x + \quad \text{(B.5)}$$

$$\frac{W}{G}\sum_{i=1}^{\alpha}\frac{cos\alpha_i}{\alpha_i - \sin\alpha_i cos\alpha_i}\sin\frac{\alpha_i x}{L}\exp\left(-\frac{\alpha_i^2 ct}{L^2}\right) \quad \text{(B.5)}$$

$$u_y(y,t) = \left[-\frac{W(1-\nu)}{2GL} + \frac{w(1-\nu_u)}{GL}\sum_{i=1}^{\infty}\frac{\sin\alpha_i cos\alpha_i}{\alpha_i - \sin\alpha_i cos\alpha_i}\exp\left(-\frac{\alpha_i^2 ct}{L^2}\right)\right]y \quad \text{(B.6)}$$

Where ν_u is the undrained Poisson's ratio, B is the Skempton pore-pressure coefficient, x is the location in the x-direction, y is the location in the y-direction, L is domain length, G is the shear modulus, and c is the general consolidation coefficient,

$$c = \frac{2kB^2G(1-\nu)(1+\nu_u)^2}{9(1-\nu_u)(\nu_u-\nu)} \tag{B.7}$$

t is the time and $\alpha_i, i = 1, \infty$, are the roots of

$$\tan\alpha_i = \frac{1-\nu}{\nu_u-\nu}\alpha_i \tag{B.8}$$

For the case in the validation section, $\nu_u = 0.5$, and $\nu = \frac{1}{1+c_f\phi K_{dr}}$. Pressure, total stress σ_{xx}, σ_{yy}, σ_{zz}, and shear stress σ_{xy} can be calculated as functions of position and time as

$$p(x,t) = \frac{2WB(1+\nu_u)}{3L}\sum_{i=1}^{\infty}\frac{\sin\alpha_i}{\alpha_i-\sin\alpha_i\cos\alpha_i}(\cos\frac{\alpha_i x}{L} - \cos\alpha_i)\exp\left(-\frac{\alpha_i^2 ct}{L^2}\right) \tag{B.9}$$

$$\sigma_{xx} = 0 \tag{B.10}$$

as on the right boundary there is no traction.

$$\sigma_{yy} = -\frac{W}{L} - \frac{2W(\nu_u-\nu)}{L(1-\nu)}\sum_{i=1}^{\infty}\frac{\sin\alpha_i}{\alpha_i-\sin\alpha_i\cos\alpha_i}\cos\frac{\alpha_i x}{L}\exp\left(-\frac{\alpha_i^2 ct}{L^2}\right) + \tag{B.11}$$

$$\frac{2W}{L}\sum_{i=1}^{\infty}\frac{\sin\alpha_i\cos\alpha_i}{\alpha_i-\sin\alpha_i\cos\alpha_i}\exp\left(-\frac{\alpha_i^2 ct}{L^2}\right) \tag{B.11}$$

$$\sigma_{xy} = 0 \tag{B.12}$$

In this 2D case, u_y is ignored and assumed to be uniform along the x-direction, so is σ_{yy} along the x-direction. σ_{xy} is always 0. The external load is applied in the normal direction to the surface. In the direction parallel to the surface there is no external load.